REDESIGNING A BICYCLE CRANK ARM FOR METAL ADDITIVE MANUFACTURING BY APPLYING DFMAM GUIDELINES TO THE TOPOLOGY OPTIMIZATION PROCESS

A thesis presented to the faculty of the Graduate School of Western Carolina University in partial fulfillment of the requirements for the degree of Master of Science in Technology

By

Jeremy Smith

Advisor: Dr. Martin Tanaka
School of Engineering and Technology

Committee Members:
Dr. Patrick Gardner, Rapid Center, College of Engineering and Technology
Dr. Sudhir Kaul, School of Engineering and Technology

March 2019

ACKNOWLEDGEMENTS

I would like to sincerely thank my advisor, Dr. Martin Tanaka, and my committee members, Dr. Sudhir Kaul and Dr. Patrick Gardner. Each member has exhibited patience, encouragement, and assistance to help me overcome the numerous obstacles that I have encountered throughout my research. I would also like to express gratitude to Monty Graham and Mike Clare for their contributions pertaining to the creation of the initial three-dimensional model of the crank arm. Without the help and guidance of each member, this research could not have been successfully completed. I would also like to thank my fellow graduate students for their feedback, assistance, and friendship.

Finally, I must express my gratitude to my wife for providing me with unfailing support and continuous encouragement throughout the process of researching and writing this thesis. I also want to thank my family for their constant backing throughout the duration of my education. This accomplishment would not have been possible without them. Thank you.

TABLE OF CONTENTS

List of Tables

List of Figures

ABSTRACT

REDESIGING A BICYCLE CRANK ARM FOR METAL ADDITIVE MANUFACTURING BY

APPLYING DFMAM GUIDELINES TO THE TOPOLOGY OPTIMIZATION PROCESS

Jeremy Smith, M.S.T.

Western Carolina University (March 2019)

Advisor: Dr. Martin Tanaka

Metal additive manufacturing has transformed the conventional design process. With the assistance of

additive manufacturing, complex and novel geometries that were previously unfeasible to construct using

convention methods, can now be fabricated. Traditionally manufactured parts can be improved upon by

employing topology optimization and Design for Metal Additive Manufacturing (DFMAM) guidelines.

This research optimizes a commercially manufactured bicycle crank arm for the metal additive

manufacturing process. The initial three-dimensional CAD model was obtained by using a white light

scanner. Loading conditions obtained from cycling loads found in published literature, were applied to an

ANSYS Finite Element Analysis (FEA) model. The FEA model was used to determine the von-mises

stress, strain, and deflection that occurred throughout the part. These results were transferred to ANSYS's

Topology Optimization module, which uses an iterative process to remove areas of material that

experience low amounts of stress. After each iteration, the solver recalculates the maximum stress and

removes additional material until the solution converges on a target maximum stress value. DFMAM

principles were applied to the resulting optimized geometry to increase the part's printability. The

optimized design was calculated to weigh 41.5% less than the original crank arm. The FEA results

showed that the maximum stress increased from 41.2% of the material's yield strength to 61.5% of the

material's yield strength, which is greater than the target optimization stress value of 50% of the

material's yield strength. The simulation results were confirmed by a physical experiment. Both the

original crank arm and the DFMAM optimized crank arm were printed using a metal additive manufacturing machine. A testing apparatus was designed and fabricated to enable the testing of each crank arm by a universal tensile testing machine. Testing was conducted throughout the range of motion at 15-degree intervals. Strain gauges and dial indicators were used to measure strain and deflection for each test. The resulting experimental data closely resembled the results from the FEA model, thus validating the theoretical simulations. The topology optimization software was proven to be a suitable and useful design tool for optimizing parts for metal additive manufacturing. However, DFMAM principles must still be applied to the resulting optimized geometry to achieve a highly manufacturable design. In conclusion, this research has shown, by using a bicycle crank arm as an example, that topology optimization in conjunction with DFMAM principles can reduce the weight of an existing product without exceeding a targeted maximum stress level.

CHAPTER 1:   INTRODUCTION

Computer Aided Design programs play an important role in the design phase of a product.

Modern CAD systems help engineers explore design ideas, visualize concepts, and simulate product

performance in the real world [1]. With the use of CAD, design engineers can reduce the time it takes to

design and test a new product. These newly designed parts can be verified through a series of theoretical

tests and simulations. Traditional CAD software packages have been developed to incorporate Design for

Manufacturing (DFM) principles for conventional manufacturing methods such as subtractive

manufacturing (milling, turning, grinding, etc.), injection molding, casting, and forming. However, the

conventional design approaches associated with these manufacturing methods are not well-suited for

additive manufacturing. New programs and new design guidelines need to be incorporated into the design

process for parts that are produced using additive manufactured. The additive manufacturing process has

generated significant interest because it can now be used to manufacture fully-functional production parts,

not just rapid prototypes for visual or educational purposes [2].

Topology optimization is a new design methodology that can be used in conjunction with metal

additive manufacturing to create a product that leverages the capabilities of metal additive manufacturing

technology. Topology optimization can be used to find the optimum distribution of material within a part

to minimize mass and to maximize stiffness [3]. However, Design for Metal Additive Manufacturing

(DFMAM) principles must also be applied to the optimized geometry to enable the part to be

manufactured.

This research seeks to determine if a traditionally manufactured part can be improved by applying

topology optimization in conjunction with design for metal additive manufacturing guidelines with the

intent to be manufactured by using a metal additive manufacturing machine. A commercially

manufactured Sugino RD2 bicycle crank arm is used to demonstrate how this redesign process can

improve the performance of an existing part. A computer simulation is first conducted to determine the

structural characteristics of the original crank arm. Next, a topology optimization study is performed at the angle where the greatest force is applied, however, the optimized crank arm is evaluated over the entire range of motion. DFMAM guidelines are incorporated into the design process to increase the manufacturability of the optimized structure. A second computer simulation is conducted to evaluate the characteristics of the newly designed optimized crank arm. A fixture is built, and an experiment is conducted to validate the simulation results. Finally, the results are evaluated to determine the differences in the strain, stress, deflection, and weight between the two parts. The goals for the optimized crank arm are to exhibit the following characteristics:

1. Reduce the weight of the original part by 50%

2. Keep the maximum stress value less than or equal to 50% of the of the material's yield strength (Stress Factor of Safety = 2)

3. Keep the maximum stress at the optimization angle within 10% of the original stress value

4. Keep the maximum deflection at the optimization angle within 5% of the original deflection value

    This thesis seeks to answer the following research questions:

1. Can topology optimization in conjunction with DFMAM guidelines and metal additive manufacturing be used to improve a traditionally manufactured part?

2. If any, what are the structural differences between a conventionally manufactured part and an optimized part fabricated by a metal additive manufacturing machine?

3. Can the weight of the original part be reduced by 50% through the topology optimization process without compromising the part's structural integrity?

1.1 Overview of Thesis

Chapter 2 consists of a review of the current literature including the application of additive manufacturing machines, design for additive manufacturing, finite element analysis, and topology optimization. Also discussed was the motion of a bicycle pedal stroke and the terminology associated

with a bicycle crank arm. Next, the methods that were used to conduct the research are presented in Chapter 3 including the theoretical simulations and the validation experiment. Chapter 4 presents the findings from the operations described in Chapter 3. The results from Chapter 4 are analyzed in Chapter 5 and are compared against the original research goals. Finally, Chapter 6 presents a final summary of the findings from the research and discusses necessary future work.

CHAPTER 2:   LITERATURE REVIEW

2.1 Computer Aided Design

Design engineers have been using Computer Aided Design (CAD) to assist in product

development since 1963 when Ivan Sutherland submitted his thesis describing his work in creating what

is now recognized as one of the first interactive CAD systems [4]. His creation, Sketchpad, was the first

design program to use a graphical user interface, which allows humans to interact with computers [4].

However, Sketchpad was limited to creating sketches in only two dimensions. With the creation of

NURBS, Ken Versprille formed the basis of modern 3D curve and surface modeling [5]. In 1983,

Autodesk released the first significant CAD program for the IBM PC, which marked a huge milestone in

the evolution of CAD [5]. However, these systems were still primarily in only two dimensions. In 1987,

Parametric Technologies Corporation (PTC) released Pro/ENGINEER, a CAD program that used solid

geometry and feature-based parametric techniques to define parts and assemblies [5]. With the

advancement of personal computing technology, CAD software packages have become more readily

accessible. In 1995, SolidWorks was released, which was the first CAD program available for desktop

computers [5].

Modern CAD systems enable engineers to create high-quality products in a timely fashion. Also,

modern CAD systems help engineers to explore design ideas, visualize concepts, and simulate product

performance in the real world [1]. Through the use of CAD programs, engineers can design products

based on real-world requirements and constraints. Also, multiple design iterations can be explored and

analyzed before beginning the prototyping or manufacturing process. After the initial 3D CAD model has

been created, a prototype can be fabricated to determine if the part functions according to the pre-

determined requirements and constraints. Initial prototypes are frequently fabricated using additive

manufacturing technologies.

2.2   Additive Manufacturing

Additive manufacturing (AM) has been prevalent since the 1980s to fabricate three dimensional (3D) models and prototypes [6]. Unlike conventional subtractive manufacturing approaches, the AM process enables the fabrication of 3D macro/microstructures by adding material in a layer-by-layer manner [7]. Because AM machines fabricate parts in layers, complex and novel geometries can be produced. However, these layers can influence the mechanical properties within a printed object. For example, a part is more likely to experience failure along the XY-plane rather than along the XZ or YZ planes. Therefore, the build orientation should be considered prior to the manufacturing process. Additive manufacturing has been traditionally used to create short-term prototypes instead of fully-functional manufactured parts [6]. The AM process begins by taking a 3D CAD model and converting it into a stereolithography (STL) file, which approximates the geometry with triangles [8]. The STL file is then treated by machine-specific software, which slices the part into layers based on the machine's resolution [6]. Support material must also be generated if the component has overhanging features relative to the build plane. Each layer is then printed, and the summation of the layers comprises the final object. After the part has been formed, the support material must be removed.

2.2.1   Rapid Prototyping Methods

Many different additive manufacturing methods are used to fabricate parts. However, most methods can only produce non-functional prototypes. Fused deposition modeling (FDM) is an additive manufacturing process in which a thin filament of plastic is fed into a machine where a print head melts and extrudes the material [8]. This process is relatively inexpensive, but it is limited by the resolution of the z-axis (slice height). Standard materials used in this process include polycarbonate (PC), acrylonitrile butadiene styrene (ABS), polyphenylsulfone (PPSF), and PC-ABS blends [8]. Another AM method uses a UV polyjet machine, which exploits inkjet technologies to manufacture smooth and accurate prototypes [8]. The inkjet head deposits a photopolymer, which is cured in a layer-by-layer fashion by ultraviolet lamps. This process creates objects that have a high resolution and are dimensionally accurate. However,

these parts are usually weaker than those produced by FDM. Because UV polyjet parts are created from photopolymers, they experience degradation when exposed to UV rays for extended periods of time.

2.3 Metal Additive Manufacturing

Metal additive manufacturing also produces parts in layers, but it does not use an extruder to deposit the material. Metal AM uses a laser beam to fuse or sinter metal particles together to make solid parts. Similar to traditional additive manufacturing, metal additive manufacturing must also have support structures to uphold overhanging features. However, the support structures used in metal additive manufacturing are also used as a heat sink to prevent distortion and curling resulting from thermal stresses [9]. Metal AM also enables design engineers to minimize the number of parts within an assembly. Instead of having to manufacture separate individual components, Metal AM can be used to fabricate an assembly as one whole part, which reduces the time needed for assembly. This manufacturing process has generated a significant level of interest because it can be used to manufacture both fully-functional prototypes and production parts, not just rapid prototypes for visual or educational purposes [2].

2.3.1 Metal Additive Manufacturing Processes

Selective Laser Sintering (SLS) is a three-dimensional printing process in which a powder is sintered by the application of a carbon dioxide laser beam [8]. The laser beam fuses the powder at a specific location for each layer specified by the geometry of the object. After each layer is complete, another layer of powder is spread over the build plate. The SLS process can use a wide variety of materials but is limited by the size of the particles. Because of the high temperatures needed to melt the material, warpage and shrinkage are commonly seen in the resulting parts. Selective Laser Melting (SLM) is a metal printing process in which a high-powered laser fully melts each layer of metal powder to the previous layer [10]. SLM creates printed objects that are extremely dense and strong. According to [10], SLM can only be used with certain metals such as stainless steel, tool steel, titanium, cobalt chrome, and aluminum. Because high-temperature gradients occur during the SLM manufacturing process, SLM can lead to stresses and dislocations inside the final product, which compromises the part's physical

properties [10]. The SLM process can produce residual stresses within the part, which reduces the ultimate strength of the member [11]. Another method of 3D metal printing is Direct Metal Laser Sintering (DMLS), which can manufacture objects out of almost any metal alloy. DMLS involves spreading a very thin layer of metal powder across the surface that is to be printed [10]. Unlike SLM where the metal is completely melted, DMLS uses a laser to sinter the powder together. Additional layers of powder are then applied, thus building the object one cross-sectional layer at a time [10]. The primary advantage of DMLS is that it can produce objects free from residual stresses and internal defects that can plague traditionally manufactured metal components [10]. This is extremely important for parts that will operate under high levels of stress, such as a bicycle crank arm.

2.3.2 EOS M 290

The EOS M 290 direct metal laser sintering (DMLS) additive manufacturing machine was used to fabricate the parts for this study. According to the Electro-Optical Systems (EOS) website, the EOS M 290 enables fast, flexible, and cost-effective production of metal parts [12]. This machine has a build volume of 250 x 250 x 325 mm (9.48 x 9.84 x 12.79 inches) and uses a 400-watt fiber laser to join the metal particles together [12]. The EOS M 290 can fabricate parts in a variety of metals, such as aluminum, cobalt chrome, steel, nickel alloy, stainless steel, and titanium [12]. Currently, the M 290 located in the Rapid Center is loaded with 316L stainless steel powder, which has excellent corrosion resistance and high ductility. The M 290 also has a maximum scan speed of 7.0 m/s (23 ft./sec) and a focus diameter of 100 μm (0.004 in), which enables the ability to manufacture highly complex components [12]. Materialise Magics RP, EOSPRINT 2, EOSTATE, and EOS RP Tools are the accepted software packages for the EOS M 290.

There are multiple safety concerns when working with the EOS M 290. The metal powder is flammable, and the metal condensate is highly flammable [13]. In order to prevent the metal material from combusting, there must not be any source of ignition within the vicinity of the material, electrostatic charging must be avoided, and the metal particles must not be swirled up. The metal particles can also

7

cause health risks if it comes into contact with an operator's skin or eyes [13]. If the material comes into contact with a person's skin, it is important to wash the infected area with soap and water. Machine operators should always wear protective nitrile gloves when handling the material or operating the machine. The metal particles are also hazardous to inhale. Therefore, machine operators should always wear face masks with a P3 category filter when interacting with the metal powder. The argon used to purge the build chamber of oxygen is also very hazardous [13]. Argon gas is heavier than air and should not be inhaled. Because the gas is heavier than air, if inhaled, it can settle in one's lungs. EOS recommends the installation of a stationary oxygen measurement with alarm functions in all rooms where argon could escape if there is a leak [13]. Prior to operating the machine, it is imperative that an operator is educated on the proper safety procedures. Operators must comply with all safety warnings and must wear proper personal protective equipment (PPE).

2.4 Design for Manufacturing

Design for Manufacturing (DFM) is a methodology that involves designing with the intent to minimize the cost of production and the time-to-market without compromising the quality of the product [14]. Each unique manufacturing process is associated with different DFM guidelines. For example, parts designed for CNC machining must be checked for deep pockets and slots, inaccessible features, sharp internal corners, fillets on outside edges, etc. [15]. Assemblies with multiple parts can also be redesigned to reduce the number of parts to be manufactured and to reduce the time to construct the assembly.

2.4.1 Design for Metal Additive Manufacturing (DFMAM)

Metal Additive manufacturing enables greater design innovation, the production of lightweight structures, part consolidation, and superior component functionality [16]. Additive manufacturing, however, has some limitations as a result of the layer-by-layer manufacturing process. Objects with downward faces, overhanging features, steep angles, and thin walls may need support structures to enable accurate fabrication of the part [17]. Support structures must be removed from the part after the fabrication process is complete, which is known as post-processing.

Features with angles greater than 45° relative to the build platform usually do not require support structures but features with angles less than 45° do need support structures [16]. This concept is further explained in Figure 2.1.
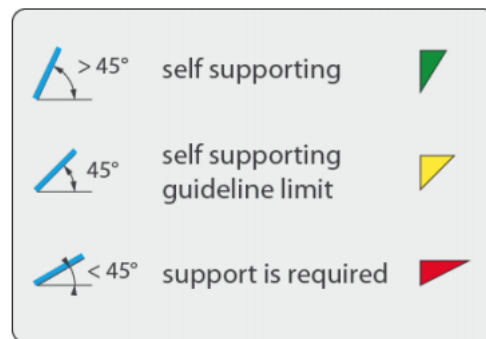
Figure 2.1: Overhanging Angles [16]

Overhanging features tend to acquire stresses easily during the printing process, which can cause warping and damage to the features [18]. Wall thickness is usually constrained by the resolution of the additive manufacturing machine. Features must have a sufficient thickness so that they are strong enough to withstand the stresses caused during post-processing [19]. Also, features with thin walls are susceptible to experience warpage or distortion due to the poor thermal conductivity of the feature. According to [19], machine manufacturers recommend that the minimum feature size in any section (i.e. XY) plane should be greater than or equal to four times the resolution, whereas the minimum feature size in Z direction should be greater than or equal to the resolution [19]. Round holes with small diameters, teardrop-shaped holes, and diamond-shaped holes can usually be manufactured without the use of support structures.

However, these features may have dross on the downward facing surfaces [16]. Dross is merely the

formation of material in overhanging regions [20]. Figure 2.2 shows several allowable shapes for self-

supporting internal features, and Figure 2.3 displays an example of dross formation.
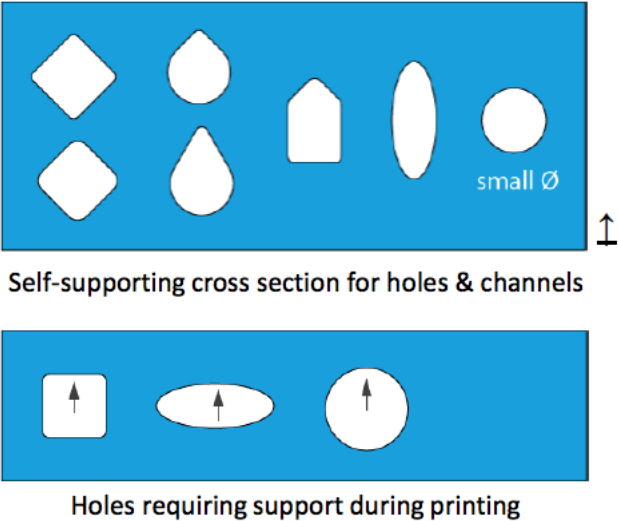
Figure 2.2: Internal Features [16]
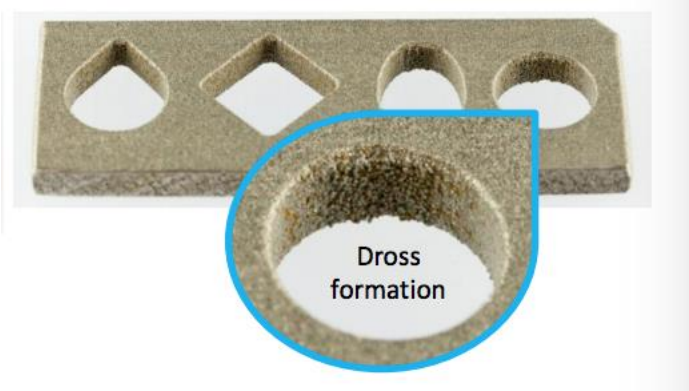
Figure 2.3: Formation of Dross on Downward Faces [16]

Design for Metal Additive Manufacturing (DFMAM) also includes part orientation relative to the build platform. Parts should be orientated to reduce the number of overhanging features and corresponding support structures. Parts should also be orientated to reduce internal downward faces that cannot be accessed by post-processing machines. For example, round internal channels may have supporting structures that are unable to be accessed by support removal tools. Also, when possible, the build direction should be selected to minimize the overall height of the object within the build chamber, which reduces the build time and the amount of needed material [21].There is also a direct correlation between the height of a build and the cost of fabrication. Therefore, the engineer must consider the build orientation of the part during the design process.

A part's orientation on the build platform must also be considered before the printing process can begin. Parts should not be oriented parallel with the recoater blade to minimize the probability of the recoater blade crashing into the part [22]. It is better for the recoater blade to first pass over a corner of the part than to first pass over a long flat wall. Therefore, it is recommended to rotate a part 5 to 45 degrees around the Z axis. This concept is illustrated below in Figure 2.4 where the gray rectangle represents the part and the blue bar represents the recoater blade.
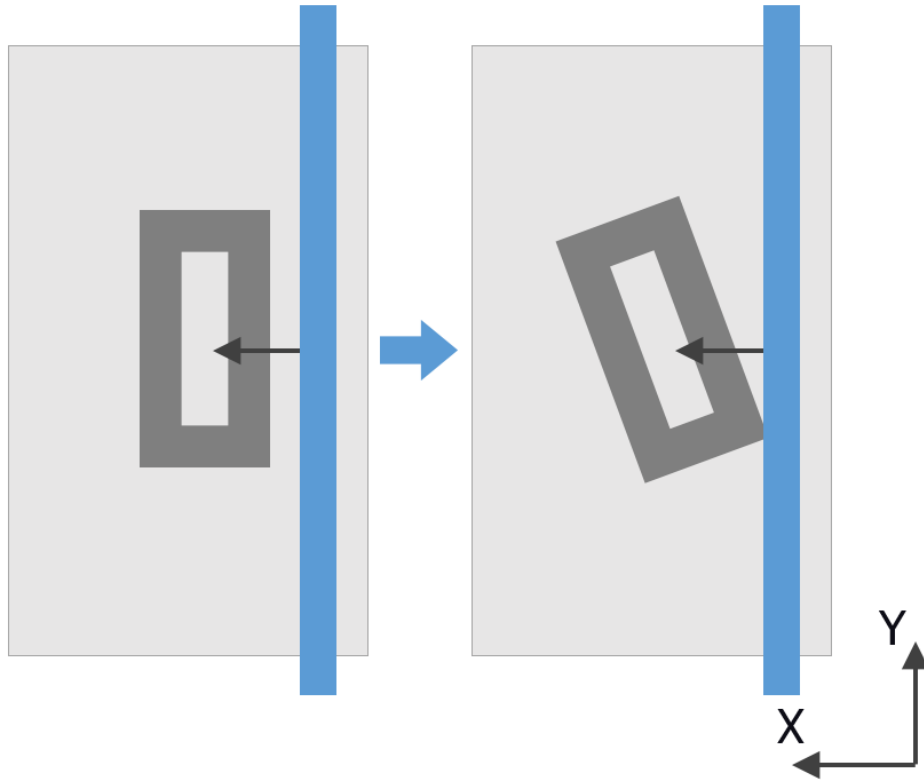
Figure 2.4: Build Orientation Relative to the Recoater Blade [22]

A part's location on the build platform should also be considered prior to the printing process. When nesting multiple parts on a build platform, it is best to add some space behind the parts along the recoating axis so that the parts are not in a straight line relative to the recoater blade [22]. Therefore, if one part fails to print properly, it will not affect the success of the other objects on the build platform. This principle is illustrated in Figure 2.5 where the grey circular objects represent the parts to be printed and the blue bar represents the recoater blade.
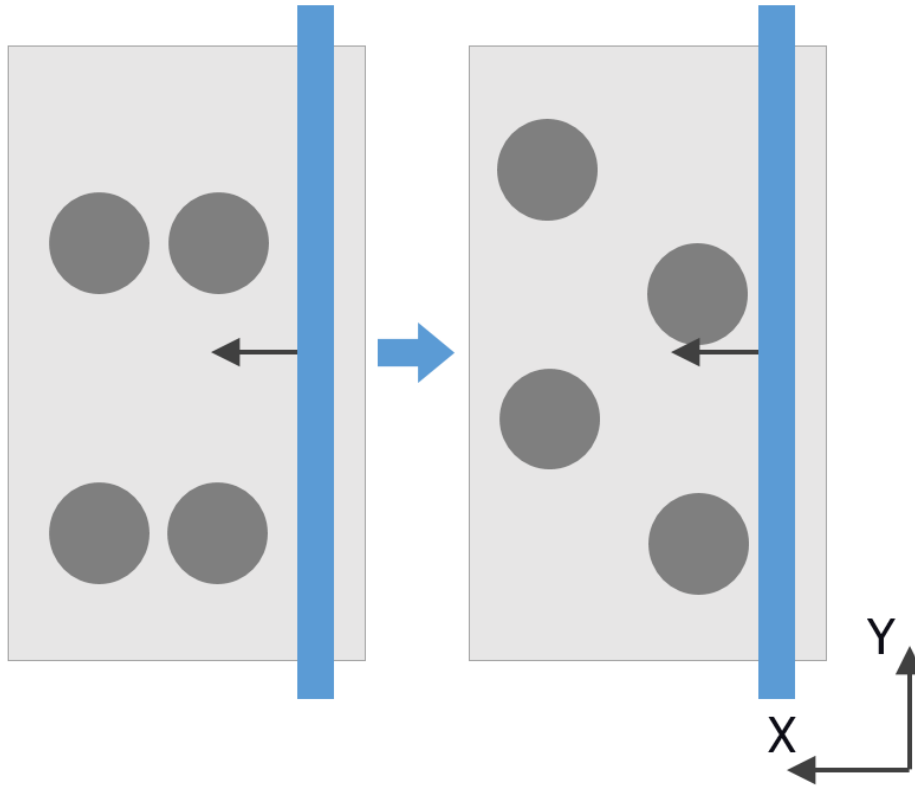
Figure 2.5: Part Location on the Build Platform [22]

The number of parts to be manufactured also affects the build orientation of the part [21]. Therefore, batching is considered to be a part of the DFMAM process. For example, if only one part is to be fabricated, the part can then be oriented to minimize the height of the object. However, if multiple parts are to be manufactured, the object may need to be oriented to occupy a smaller footprint on the build platform. Therefore, prior to designing the part, the engineer must consider the number of parts to be manufactured.

Finally, prior to (re)designing a part for metal additive manufacturing, the potential cost must be considered. There are multiple factors that affect the cost of an additively manufactured part. Part volume, support structure volume, build height (Z axis), inert gas consumption, post-processing, and the volume

of parts to be fabricated. The reduction of a part's volume would reduce the amount of material needed, which would decrease the build time and the material cost. Parts can be designed in such a way to minimize or even eliminate the need for support structures, which would reduce the material cost, machine run time, and the post-processing time. Because of the layer-by-layer nature of additive manufacturing, the build height greatly affects the run time of the fabrication process. Jobs that have extensive build times consume more time, power, and inert gas. Parts that require a large amount of support material or a part-on-part support structures affect the amount of necessary post-processing. In general, metal additively manufactured parts cost more than traditionally manufactured parts. Therefore, the pros and cons of metal additive manufacturing must be considered during the preliminary design phase of a project.

Each of these limiting factors must be considered during the design phase relative to the desired additive manufacturing process.

2.5   Finite Element Analysis

Finite Element Analysis (FEA) is a numerical and computer-based technique used to solve complex engineering design problems [23]. Finite Element Analysis is useful for predicting how a product will react to real-world forces, vibrations, and other physical effects [24]. FEA can be used to determine whether a product will fail or perform according to the way it was intended to perform. FEA also enables design engineers to simulate the performance of a part or system before building a physical prototype [25]. FEA helps designers to understand stress levels, the magnitude and direction of deformation, temperatures, and responses to vibrations prior to the prototyping phase [25].

Finite Element Analysis begins by "breaking down a real object into a large number (thousands to hundreds of thousands) of finite elements, such as little cubes" [24]. A 3D model that has been divided into these finite elements is called a mesh. A single bad element within a mesh has the potential to degrade the results of the analysis. Mesh quality is determined by the size and the angles of the elements [26]. Mesh problems usually occur when the element angles are either really large (close to 180 degrees)

or really small (close to 0 degrees) [26]. There are two different element types that are commonly used in a mesh to represent the geometry of the part (tetrahedral and hexahedral). Tetrahedral elements are commonly used to characterize curved and angled geometries [27]. The size of a tetrahedral mesh can easily be reduced to increase the resolution near complex features of interest. For simple geometries, a hexahedral mesh can sufficiently represent a part with a smaller number of elements [27]. Therefore, a hexahedral mesh usually has fewer elements than a tetrahedral mesh, thus reducing the time for the computer to calculate the solution. The element type depends on the complexity of the geometry, the computing power of the computer, and the desired accuracy of the mesh. FEA uses mathematical equations to determine the forces applied to each individual element. As the elements are made smaller and smaller, the results of the analysis will begin to converge on a more accurate solution. The analysis results can be verified by computing calculations by hand at a specific point or by placing a strain gage on the part. The analysis is verified if the results of the hand calculations and/or the strain gage align with the FEA results.

2.6 Topology Optimization

Topology Optimization is used to find the most optimum distribution of material within a part to minimize mass and to maximize stiffness [3]. Topology Optimization works by taking a solid block of material and removing material from it to minimize or maximize an objective such as mass, displacement, stiffness, etc. [28]. These parameters must be optimized with respect to a set of pre-defined constraints, such as maximum allowable stress, maximum displacement, volume, shape, and the desired manufacturing method [29]. Boundary conditions must also be applied to the model to simulate the forces acting upon the part. One of the main strengths of topology optimization is the efficiency of computing gradients for large problems with many design variables [30].

The topology optimization process begins by defining the design space, which is the initial geometry that forms the boundary of the optimized shape. The design space includes the maximum allowable volume in addition to holes and slots for mating geometries. Next, a mesh is created within the

design space to divide the part into many finite elements. According to [31], it is typical for each finite element within the design domain to be defined as a design variable, allowing a variation in density [31]. Therefore, the accuracy of the optimization depends on the size of the elements within the mesh. Next, loads are applied to the geometry to simulate the applied real-world forces. The design space is then optimized based on the parameters mentioned above (stress, displacement, mass, etc.). The results can be validated through finite element analysis. If the results of the analysis are unsatisfactory, the design engineer can change the parameters of the experiment to manipulate the results of the optimization process. Several iterations of this process may be needed to achieve a satisfactory result.

2.7 Pedal Stroke Cycle of a Cyclist

In order to generate accurate FEA and topology optimization results, the mechanics of a bicycle pedal stroke must be understood in order to apply the proper loading conditions to the crank arm. It is important to understand which angles of the pedal stroke receive the maximum amount of force applied by the cyclist. The corresponding geometries must be strengthened to withstand the forces so that the structure does not experience failure.

One cycle of a bicycle pedal stroke corresponds to one complete revolution (360°) of the crank arm. The pedal cycle consists of a down-stroke phase and an up-stroke phase. The down-stroke phase ranges from 0° (TDC) to 180° (BDC), and the up-stroke phase ranges from 180° to 360°. As seen in Figure 2.6, the greatest forces are applied during the down-stroke of the pedal cycle after 90° [32]. However, the specific angle where the maximum force is applied can vary based on the riding style of the cyclist.
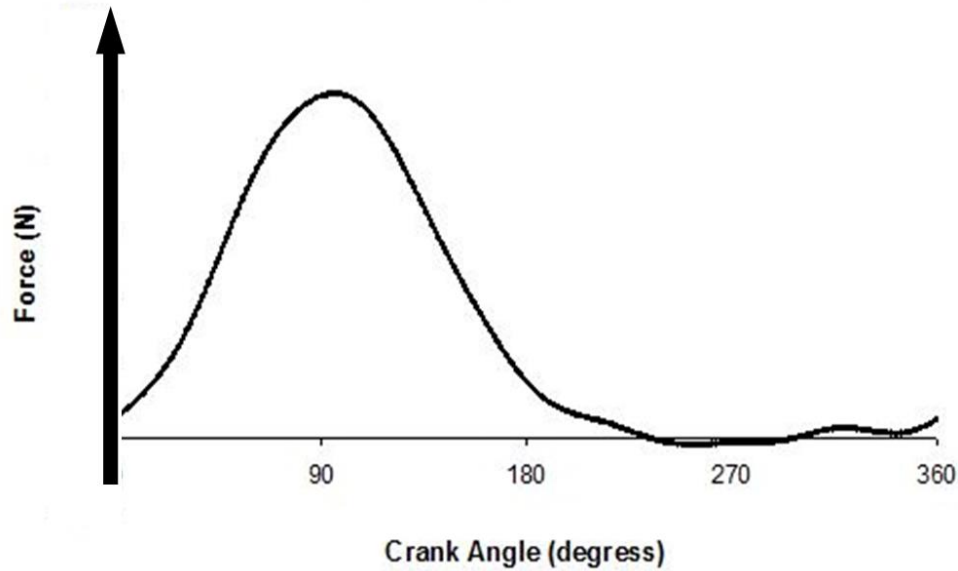
Figure 2.6: Force vs Crank Angle [32]

The forces applied by a cyclist to the pedal do not always transmit to forward motion. Some of the force is applied parallel to the crank arm, which wasted and not transmitted to the drivetrain of the bicycle. This parallel force is known as radial force. Only the force that is applied perpendicular to the crank arm is transmitted to the drivetrain of the bicycle. This perpendicular force is known as tangential force, which is required to propel the bicycle forward. The difference in these forces can be seen in Figure 2.7 [33]. Not only is tangential force generated during the down-stroke of the pedal cycle, but there is also a small tangential force created simultaneously by the opposing foot during the up-stroke of the pedal cycle. As a cyclist applies force during the downstroke to the right pedal, the cyclist is simultaneously pulling up on the left pedal. These tangential forces need to be calculated to properly determine the amount of torque that is to be applied to the axle geometry in both the FEA and the topology optimization studies.

17
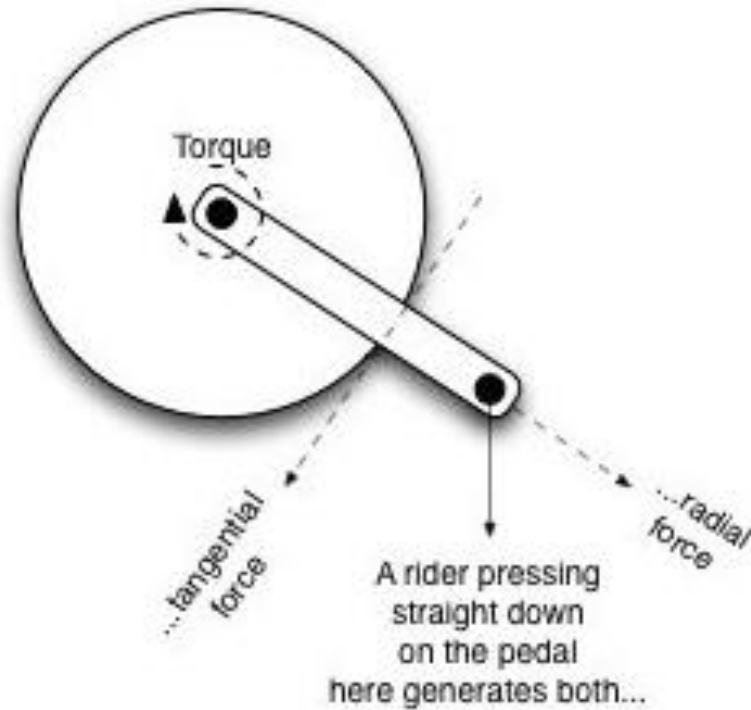
Figure 2.7: Radial Force and Tangential Force [33]

2.8 Bicycle Crank Arm Terminology

The terminology used to describe the features of the Sugino RD2 crank arm is shown in Figure 2.8. First, the spider of the crank arm consists of the five finger-like features protruding from the axle geometry. These features will be referred to as spider legs throughout this thesis. The pedal hole geometry is where the pedal is attached to the crank arm. The axle geometry is used to connect the opposing crank arm to the drivetrain through a diamond-shaped axle. This diamond-shaped hole will be referred to as the axle geometry throughout this thesis.
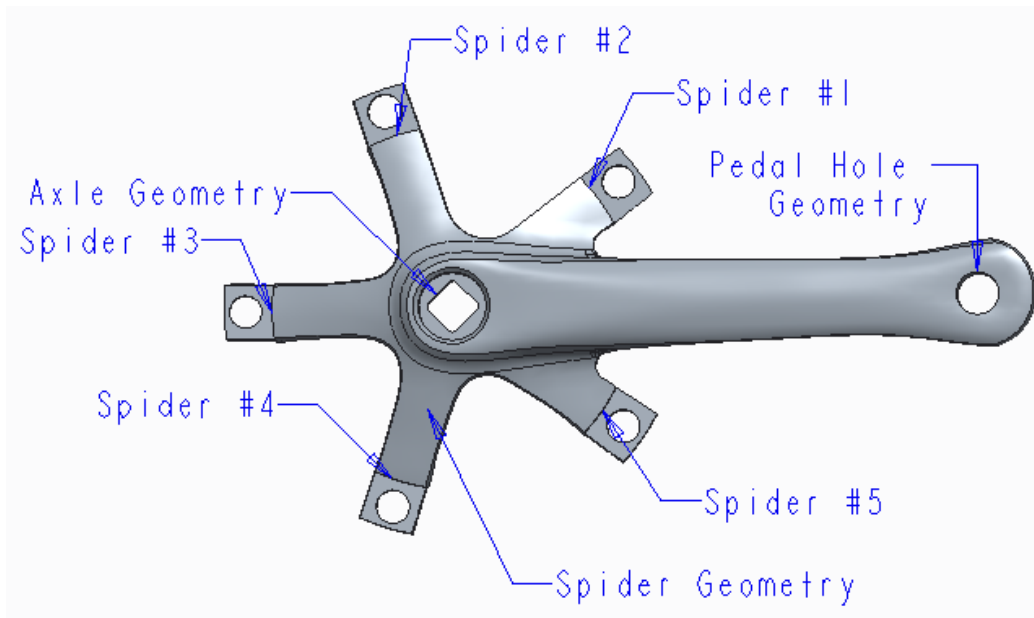
Figure 2.8: Naming Convention of the Crank Arm

The critical dimensions of the crank arm are shown in Figure 2.9. The bolt holes on each spider leg are 10.4 mm in diameter and they are located on a 130 mm diameter bolt-hole circle. The pedal hole is 13.3 mm in diameter and is located 165 mm from the center of the axle geometry.
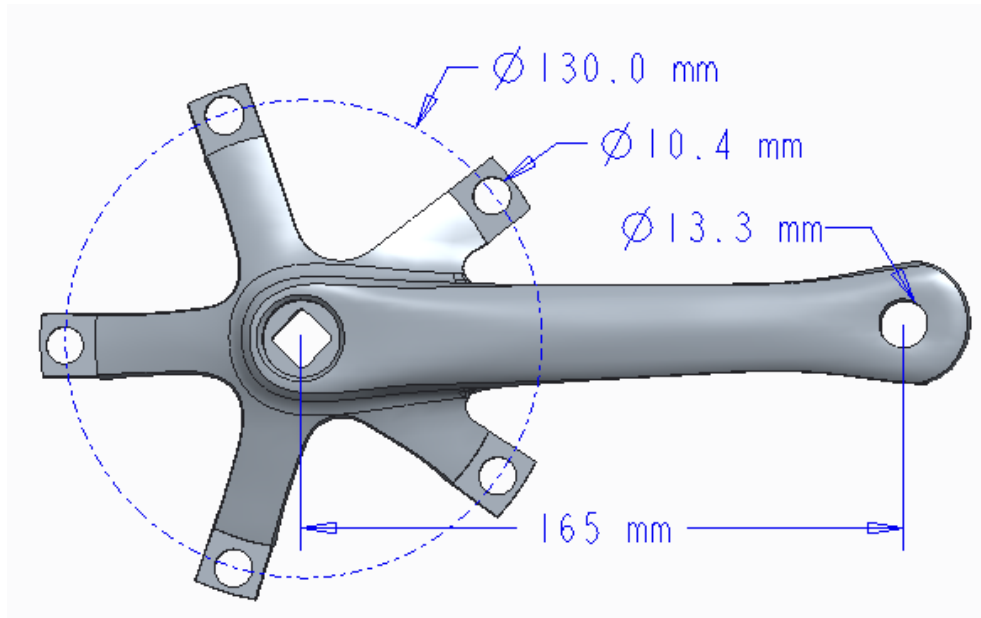
Figure 2.9: Critical Dimensions of the Crank Arm

CHAPTER 3:   METHODS

This section presents the methods that were used to develop the loading conditions that were to be applied to the crank arm during the theoretical analysis phase in addition to the physical testing phase. This section also discusses the methods that were used to perform the theoretical analyses and the methods that were used to conduct the experimental analyses. The theoretical analysis section includes the methods used to conduct the finite element analysis study, the topology optimization study, and the design verification process. The experimental analysis section discusses the methods used to fabricate the crank arms, to design and fabricate the testing apparatus, and the methods used to conduct the physical testing of the crank arms.

3.1   Creating a 3D Model of the Crank Arm

With the assistance of Monty Graham and Mike Clare, a three-dimensional (3D) model of the original Sugino RD2 crank arm was generated. Three-dimensional point cloud data was collected using the Rapid Center's GOM ATOS II white light scanner, a type of coordinate measuring machine that uses advanced measurement and projection techniques to produce high quality data and precision accuracy for full-object dimensional analysis [34]. The point-cloud model was then stitched together to create a 3D solid model of the crank arm. This 3D model was used to conduct the initial FEA and the topology optimization study.

3.2   Mathematical Model of the Loading Conditions Applied to the Crank Arm

A mathematical model was developed to determine the forces that were to be applied to the crank arm during an intense cycling effort. These forces were used to determine the loading conditions for the Finite Element Analysis model, the Topology Optimization study, and the physical testing of the crank arm. Experiment data was obtained from a study conducted by Stone and Hull [35] who measured the pedal forces in the X, Y, and Z directions (see Figure 3.1). Data points from these curves were extracted using ImageJ software and then imported into Excel for analysis (Figure 3.2).

21
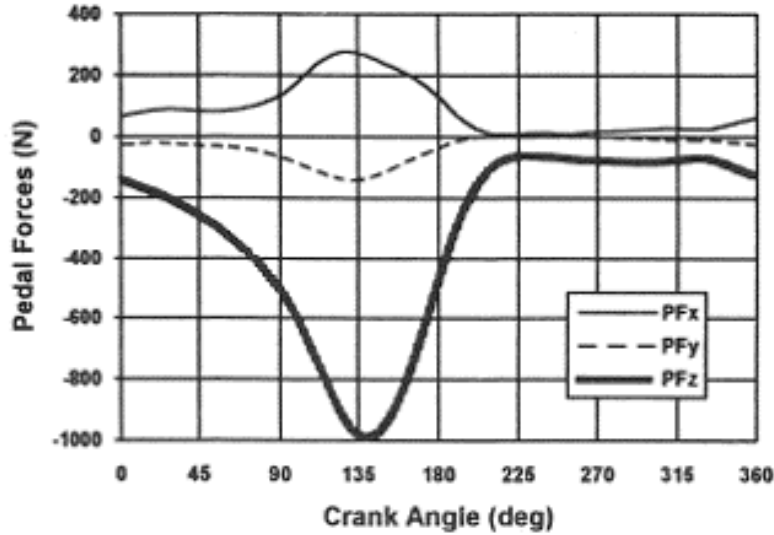
Figure 3.1: Pedal Forces (N) vs Crank Angle (deg) [34]

For this study, the Z axis is considered to be in the vertical direction, the X axis is to the front of the bicycle, and the Y axis is considered to be to the left or the right of the cyclist. Only the pedal forces in the X and Z directions were used to generate the loading conditions for this research. The pedal forces in the Y direction (F_Y) were small and considered to be negligible. First, the resulting data curves from Figure 3.1 needed to be converted into individual coordinate points. ImageJ, an open source image processing program designed for scientific multidimensional images, was used to convert the force vs. angle curves into coordinate points for further calculations [36]. Two separate operations were performed on the image in Figure 3.1. The first operation was used to determine the pedal forces in the X direction (F_X), and the second operation was used to determine the pedal forces in the Z direction (F_Z). The conversion process began by importing the graph shown above (Figure 3.1) into the Image J software. Next, the coordinate system of the image was selected and defined within the software. Numerous points were placed along the curve under consideration. 72 points were used to depict the PF_X curve and 115 points were used to represent the PF_Z curve. The software generated X and Y coordinates for each point

22

along the curve that corresponded to the angle in degrees and pedal force in Newtons. These data points were then imported into Excel. Figure 3.2 displays a plot of the pedal forces in the X and Z directions that was generated from the extracted data points.
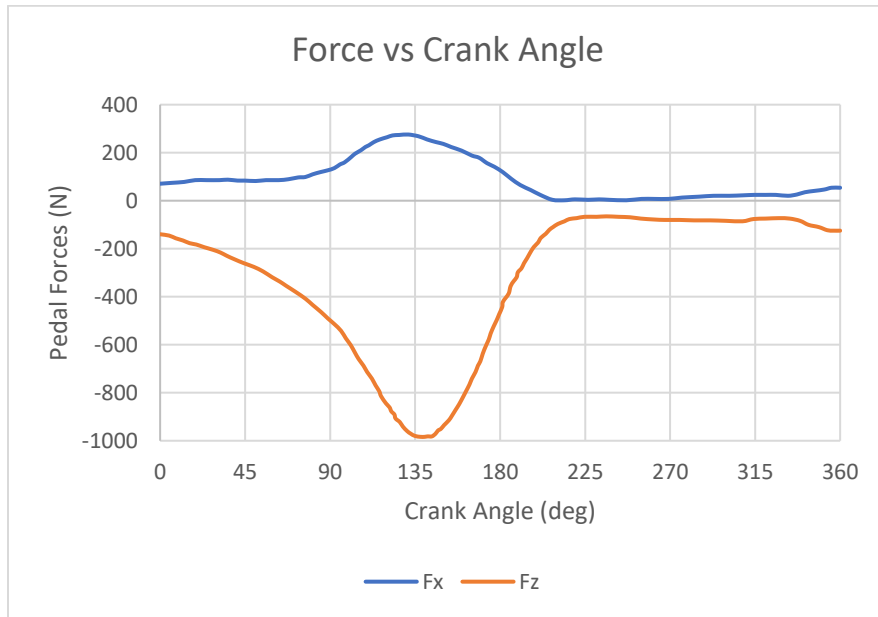
Figure 3.2: Extracted Excel Data: Force vs. Crank Angle

The resulting coordinate points were then interpolated to calculate the angle and force in 15-degree increments. Equation 3.1 was used to interpolate the data, where x equals the desired angle and y equals the corresponding force.

$$y = y_1 + (x - x_1)\frac{y_2 - y_1}{x_2 - x_1}$$

(3.1)

This interpolation calculation resulted in a set of a forces (F_X and F_Z) in 15-degree increments ranging from 0 degrees (Top Dead Center) to 360 degrees. This study only focused on the angles ranging from 0 degrees (TDC) to 180 degrees. However, to simplify the data for future calculations, a new coordinate system was implemented where 0 degrees is when the crank arm is parallel with the riding surface. Therefore, the new analysis ranged from 90 degrees to -90 degrees. Next, the magnitude of the resultant pedal force vectors (F_R) were calculated by using equation 3.2.

$$F_R = \sqrt{F_X{}^2 + F_Z{}^2} \tag{3.2}$$

The maximum pedal force was calculated by applying the previous formula to the X and Z forces for when the angle of the crank arm equaled 135 degrees. When $\phi = 135\,°$: $F_X = 270.67\ (N)$ and $F_Z = -980.07\ (N)$.

$$F_{R\ max} = \sqrt{270.67^2 + -980.07^2} = 1016.76\ (N) \tag{3.3}$$

After the magnitude of the resultant pedal force vectors were calculated, the direction of the vectors could then be determined by using equation 3.4.

$$\psi = arctan\left(\frac{F_x}{F_z}\right) \tag{3.4}$$

Equation 3.5 was used to calculate the final crank angle (Θ), which was obtained by adding the resultant angle (ψ) to the initial crank angle (ϕ).

24

$$\theta = \phi + \psi \tag{3.5}$$

A rotation matrix was employed to calculate the X and Z coordinates of the pedal bolt hole on the crank arm after the arm had been rotated by the final crank angle. The two-dimensional rotation matrix is shown in equation 3.6.

$$R(\theta) = \begin{bmatrix} \cos(\theta) & -\sin(\theta) \\ \sin(\theta) & \cos(\theta) \end{bmatrix} \tag{3.6}$$

The rotation matrix was then multiplied by the original x and y coordinate point. This multiplication creates a new coordinate point (x' and y'). Equation 3.7 represents this coordinate transformation.

$$\begin{bmatrix} x' \\ z' \end{bmatrix} = [R(\theta)] \begin{bmatrix} x \\ z \end{bmatrix} \tag{3.7}$$

Equations 3.8 and 3.9 display how x' and z' were calculated from the above rotation matrix multiplication. The initial x coordinate equals the length of the crank arm (L_C), which is 165 mm, and the initial Z coordinate is 0 mm.

$$\begin{bmatrix} x \\ z \end{bmatrix} = \begin{bmatrix} 165 \\ 0 \end{bmatrix}$$

The expanded form of the rotation matrix is shown below.

$$x' = x\cos(\theta) - z\sin(\theta) \quad \rightarrow \quad x' = 165\cos(\theta) - 0\sin(\theta) = 165\cos(\theta) \tag{3.8}$$

$$z' = x\sin(\theta) + z\cos(\theta) \quad \rightarrow \quad z' = 165\sin(\theta) - 0\cos(\theta) = 165\sin(\theta) \tag{3.9}$$

Finally, the resultant vector (F_R) was divided into separate X and Z vectors relative to the local coordinate system of the crank arm. This creates the proper loading conditions to be applied

to the crank arm during the finite element analysis study and the topology optimization study. The equations used to create the separate force vectors for ANSYS are derived from Figure 3.3. The equations are shown below (see equation 3.10 and 3.11).
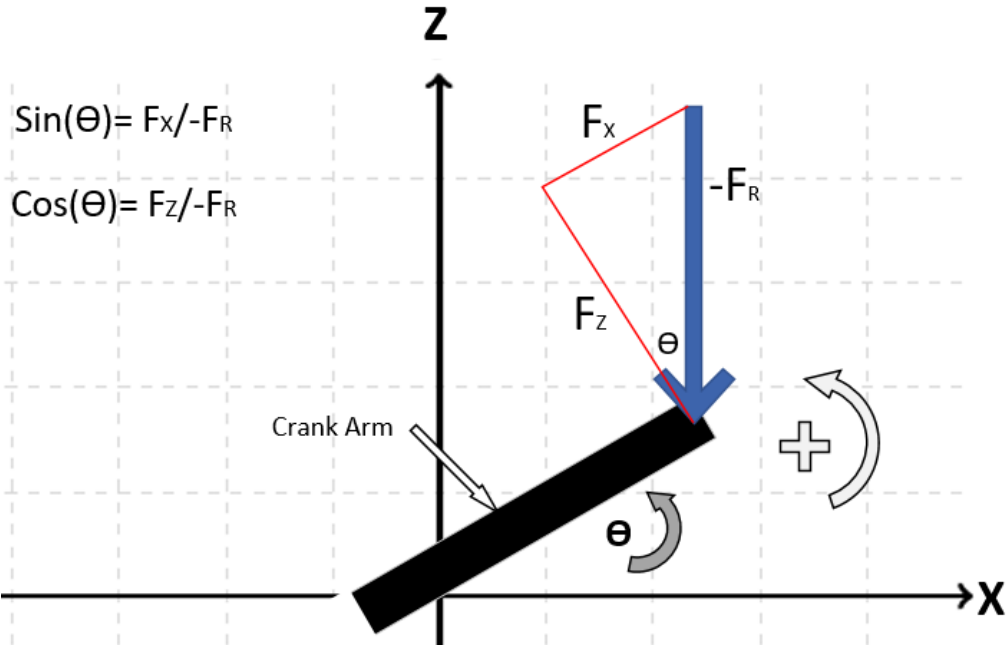
Figure 3.3: ANSYS Force Derivation

$$Loading\ force\ in\ the\ X\ direction\ (N) \rightarrow F_X = -F_R * \sin(\theta) \qquad (3.10)$$

$$Loading\ force\ in\ the\ Z\ direction\ (N) \rightarrow F_Z = -F_R * \cos(\theta) \qquad (3.11)$$

The F_X and F_Z forces take into account the final angle of the crank arm (Θ). To verify the calculation, the arctangent of F_X divided by F_Z should equal the final crank angle (Θ) relative to the horizontal axis (see equation 3.12).

$$x' = \theta = \arctan\left(\frac{F_X}{F_Z}\right) \tag{3.12}$$

Next, the moment that was created by the forces acting on the pedal was calculated using equation 3.13. The force used for the pedal moment calculation was the pedal force resultant vector (F_R). The distance equaled 61 mm, which is the distance from the center of the pedal to the center of the mounting threads (shown in Figure 3.4 below)

$$M_P = F \; x \; D \;\; \rightarrow \;\; M_P = F_R(N) \; x \; 61(mm) \tag{3.13}$$

The maximum pedal moment can be found by multiplying the maximum resultant pedal force by the length of the pedal (equation 3.14).

$$M_P = 1016.76 \; (N) \; x \; 61 \; (mm) = 62022.4 \; (mNm) \approx 62 \; Nm \tag{3.14}$$
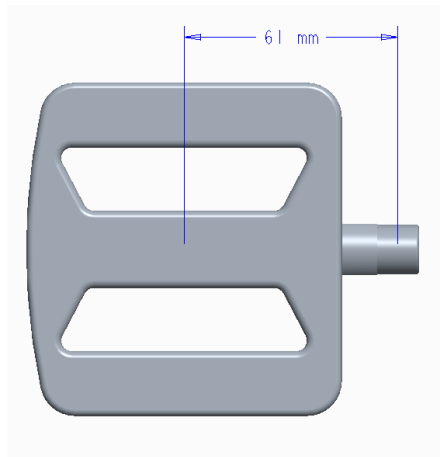
Figure 3.4: Distance at which the Force was Applied by the pedal to the Crank Arm

Finally, the forces that were applied by the axle to the crank arm were calculated. Not only does a cyclist apply forces to the crank arm during the down-stroke of the pedal cycle, but the opposing foot simultaneously pulls up on the pedal during the upstroke of the pedal cycle. The torque that is created by the upstroke pedal motion must also be applied to the axle geometry of the crank arm. In order to determine the correct axial moment, the F_X and F_Z curves were shifted by 180 degrees, which is half of the pedal cycle (Figure 3.5). The curves were shifted so that it is easy to see the corresponding pedal force data of the down-stroke and the up-stroke forces for any given angle. Both the down-stroke forces and the up-stroke forces can easily be determined by looking at the different curves for a given angle. For example, the pedal forces applied in the Z direction at -45° (relative to the horizontal axis) can be determined by looking at the data shown in Figure 3.5. When the crank is angled at -45°, the down-stroke force applied in the Z direction ($F_{Z\ down-stroke}$) equals -980 Newtons, and the up-stroke force applied in the Z direction ($F_{Z\ up-stroke}$) equals -75 Newtons. Also at -45°, the down-stroke force applied in the X direction ($F_{X\ down-stroke}$) equals 270 Newtons, and the up-stroke forces applied in the X direction ($F_{X\ up-stroke}$) equals 25 Newtons.
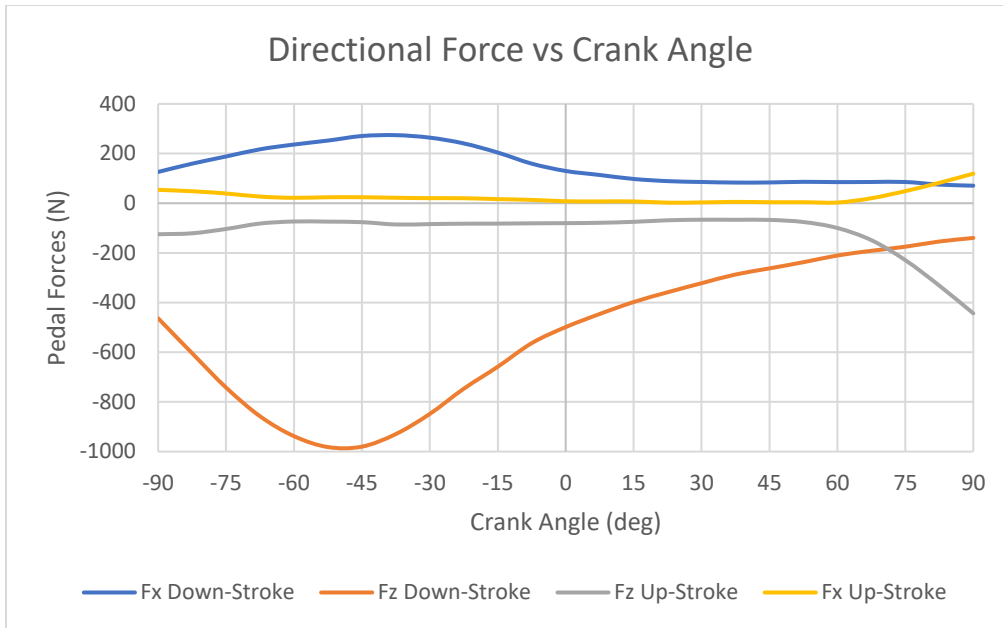
Figure 3.5: Directional Force vs Crank Angle

Next, the tangential force was calculated by using the up-stroke pedal force data gathered from Figure 3.5. The equations to calculate the tangential force were derived from Figure 3.6. The applied upstroke forces ($F_{X\,up-stroke}$ and $F_{Z\,up-stroke}$) were divided into separate force vectors. The radial force is considered to be negligible because it is applied parallel to the crank arm and does not cause the crank to rotate. The tangential force is applied normal to the crank arm, thus causing it to rotate. After the magnitude of the tangential force was calculated, the torque was then calculated by multiplying the tangential force times the length of the crank arm. The equations and the steps for this process are shown below.
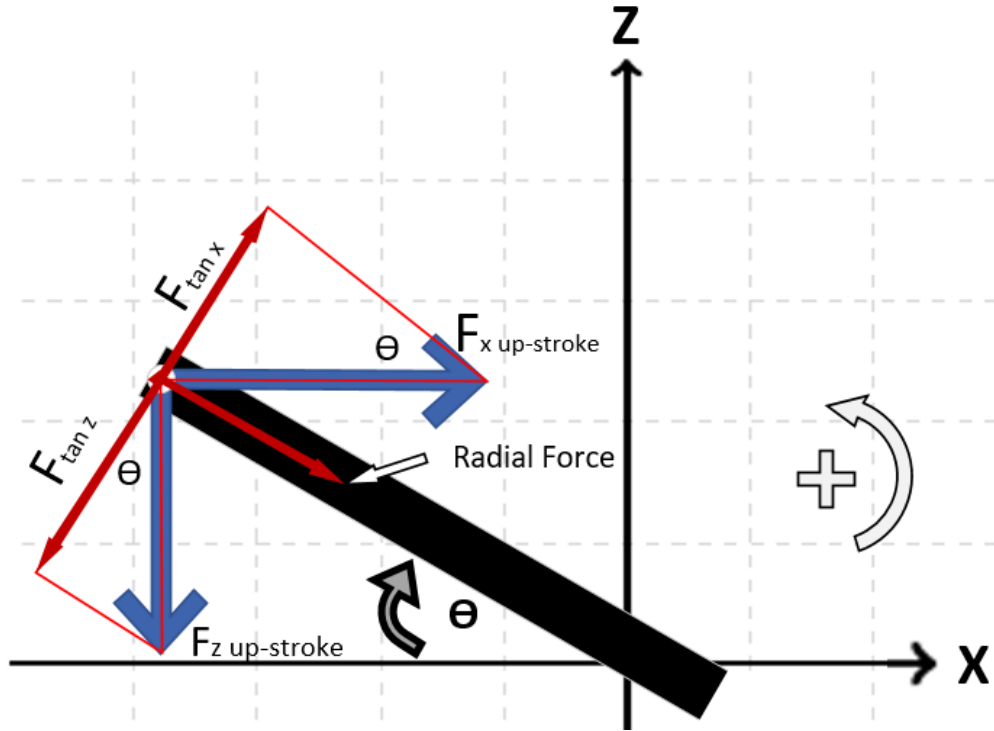
Figure 3.6: Tangential Force

The tangential force equations are shown in equations 3.15 and 3.16.

$$F_{Tan_X} = abs[F_{X\ up-stroke} * \sin(\theta)] \tag{3.15}$$

$$F_{Tan_Z} = abs[F_{Z\ up-stroke} * \cos(\theta)] \tag{3.16}$$

When the crank is at − 45 degrees (relative to the horizontal plane), θ = -60.439°, $F_{X\ up-stroke}$ = 24.138 Newtons, and $F_{Z\ up-stroke}$ = -76.196 Newtons. Using the equations above (3.15 and 3.16), the tangential force was calculated for both vectors (see equations 3.17 and 3.18).

30

$$F_{Tan_X} = abs[24.138\ (N) * \sin(-60.439)] = 20.996\ Newtons\ (clockwise) \qquad (3.17)$$

$$F_{Tan_Z} = abs[-76.196\ (N) * \cos(-60.439)] = 37.591\ Newtons\ (counter-clockwise) \qquad (3.18)$$

Next, equations 3.19 and 3.20 were used to calculate the differential of the two tangential forces to determine the direction and magnitude of the tangential force.

$$F_{Tan} = F_{Tan_Z} - F_{Tan_X} \qquad (3.19)$$

$$F_{Tan} = 37.591\ Newtons\ (counter\ clockwise) - 20.996\ Newtons\ (clockwise)$$
$$= 16.60\ Newtons\ (counter-clockwise) \qquad (3.20)$$

Finally, the torque was calculated by multiplying the tangential force by the length of the crank arm (equations 3.21 and 3.22). As previously noted, the length of the crank arm is 165 mm.

$$Torque = F_{Tan} * L_C \qquad (3.21)$$

$$Torque = 16.60\ (N) * 165\ (mm) = 2.738\ Nm\ (counter-clockwise) \qquad (3.22)$$

These steps were repeated to calculate the torque applied to the axle geometry of the crank arm when the opposing pedal is experiencing down-stroke forces (θ = -60.439°, $F_{X\ up-stroke}$ = 270.67 Newtons, and $F_{Z\ up-stroke}$ = -980.07 Newtons). The resulting torque applied to the axle geometry during the down-stroke of the opposing pedal was *40.9 Nm (clockwise).*

The final loading conditions for the optimization study are shown below in Table 3.1. Four load steps were used to properly simulate the loading conditions for each angle under consideration. The forces in step 1 represent the forces applied to the crank arm during the down-stroke of the pedal cycle, and step 3 represents the forces applied to the crank arm during the up-stroke of the pedal cycle. Steps 2 and 4 were set to equal zero so the crank arm would return to

31

equilibrium before changing from the down-stroke data to the up-stroke data. Therefore, the ANSYS

solver would determine the results according the following order:

- Step 1: Down-stroke loading conditions

- Step 2: Equilibrium

- Step 3: Up-stroke loading conditions

- Step 4: Equilibrium

Table 3.1: Topology Optimization Loading Conditions

ANSYS Topology Optimization Loading Conditions					
	Pedal Force (N)		Pedal Moment (N · mm)		Axle Moment (N · mm)
	Z-axis	X-axis	Z-axis	X-axis	Y-axis
Step 1	-501.62	884.41	-53949	30599	2738.3
Step 2	0	0	0	0	0
Step 3	0	0	0	0	-40934
Step 4	0	0	0	0	0

Table 3.2 presents the loading conditions for all the angles under consideration in the study. This

research only focused on the final crank angles between 90° and - 90° relative to the horizontal axis.

There were 12 angles (θ) that occurred within these limits. The table displays the loading conditions for

the down-stroke loading conditions (load steps 1, 5, 9, etc.) and the up-stroke loading conditions (load

steps 3, 7, 11, etc.), as well as the initial crank angle (ϕ), final crank angle (θ), and the corresponding

load step number. For each angle, Table 3.2 also displays the pedal force data in both the Z and X axes

and the total resultant force, the pedal moment data in both the Z and X axes, and the axle moment, which rotates about the Y axis. The data shown in Table 3.1 was used for the topology optimization study, and the data displayed in Table 3.2 was used during the comprehensive FEA studies and during the design verification process.

Table *3.2*: ANSYS Loading Conditions for all Angles Under Consideration

ANSYS LOADING CONDITIONS FOR ALL STEPS									
				Pedal Force Data (N)			Pedal Moment Data (Nmm)		Axle Moment Data (Nmm)
Pedal Cycle	Initial Angle (φ)	Final Angle (θ)	Step #	Z - Axis	X - Axis	Total Force (Resultant)	Z - Axis	X - Axis	Y - Axis
Down-Stroke	90	63.163	1	70.709	-139.8	156.66	-8527.5	-4313.3	15482
			2	0	0	0.00	0	0	0
Up-Stroke			3	0	0	0.00	0	0	0
			4	0	0	0.00	0	0	0
Down-Stroke	75	48.932	5	127.98	-146.9	194.81	-8959.6	-7807.2	18779
			6	0	0	0.00	0	0	0
Up-Stroke			7	0	0	0.00	0	0	-8319.7
			8	0	0	0.00	0	0	0
Down-Stroke	60	37.987	9	178.84	-139.7	226.91	-8519.3	-10909	12674
			10	0	0	0.00	0	0	0
Up-Stroke			11	0	0	0.00	0	0	-18720
			12	0	0	0.00	0	0	0
Down-Stroke	45	27.307	13	244.68	-126.3	275.37	-7705.8	-14925	9536.2
			14	0	0	0.00	0	0	0
Up-Stroke			15	0	0	0.00	0	0	-32128
			16	0	0	0.00	0	0	0
Down-Stroke	30	15.111	17	321.67	-86.86	333.19	-5298.4	-19622	10437
			18	0	0	0.00	0	0	0
Up-Stroke			19	0	0	0.00	0	0	-47610
			20	0	0	0.00	0	0	0
Down-Stroke	15	1.196	21	409.56	-8.554	409.65	521.78	-24983	12326
			22	0	0	0.00	0	0	0
Up-Stroke			23	0	0	0.00	0	0	-65289
			24	0	0	0.00	0	0	0
Down-Stroke	0	-14.604	25	498.68	129.93	515.33	7925.7	30419	12470
			26	0	0	0.00	0	0	0
Up-Stroke			27	0	0	0.00	0	0	-74219
			28	0	0	0.00	0	0	0
Down-Stroke	-15	-32.221	29	583.09	367.5	689.24	22417	-35563	9995.3
			30	0	0	0.00	0	0	0
Up-Stroke			31	0	0	0.00	0	0	-73994
			32	0	0	0.00	0	0	0
Down-Stroke	-30	-47.293	33	602.53	652.79	888.36	39820	-36754	6923.2
			34	0	0	0.00	0	0	0
Up-Stroke			35	0	0	0.00	0	0	-62905
			36	0	0	0.00	0	0	0
Down-Stroke	-45	-60.439	37	501.62	884.41	1016.76	53949	-30599	2738.3
			38	0	0	0.00	0	0	0
Up-Stroke			39	0	0	0.00	0	0	-40934
			40	0	0	0.00	0	0	0
Down-Stroke	-60	-74.147	41	264.23	930.46	967.25	56758	-16118	145.39
			42	0	0	0.00	0	0	0
Up-Stroke			43	0	0	0.00	0	0	-4753.7
			44	0	0	0.00	0	0	0
Down-Stroke	-75	-89.229	45	10.298	765.58	765.65	46700	-628.17	6252.3
			46	0	0	0.00	0	0	0
Up-Stroke			47	0	0	0.00	0	0	29403
			48	0	0	0.00	0	0	0

3.3 Theoretical Analysis

This section provides an overview of the methods that were used to analyze the original crank arm, optimize the design, and verify the newly designed crank arm. This section discusses how the Finite Element Analysis model was created and how the topology optimization study was conducted. Finally, this section also describes the process of how the faceted optimized body was smoothed, edited, and verified. ANSYS version 19.1 was used to perform the following operations.

3.3.1 Finite Element Analysis

Two Finite Element Analysis (FEA) studies were performed to examine the how the crank arm reacted under the loading conditions. The first FEA model was solved at the angle where the greatest resultant force occurred. This occurred when the original crank angle, relative to the horizontal plane, equaled -45 degrees. The loading conditions used for the initial FEA study are shown on page 32 in Table 3.1. The second FEA was designed to analyze the model for all final crank angles (θ) between 90° and -90° in increments of 15°. There were 12 angles that occurred within this range (see Table *3.2* on page 32 for the loading conditions). The corresponding loading conditions of these angles were analyzed within the second FEA study.

First, a static structural module was implemented into the workspace of ANSYS Workbench. Under the engineering data tab, a stainless-steel material was added to the project. Next, the 3D CAD model of the crank arm was imported into the system. The boundary conditions and parameters of the FEA study were established within the ANSYS Mechanical software package. The first step within ANSYS Mechanical was to assign the stainless-steel material to the geometry of the crank arm. Next, a tetrahedral element was chosen over a hexahedral element because tetrahedral elements are better for capturing complex geometries and they support adaptive mesh refinement [27]. The tetrahedral mesh was created with a maximum element size of 6.0 mm and a minimum element size of 1 mm. The 'capture proximity' setting was enabled, which reduced the size of the elements that are located along the curves and edges of the model. The 'smoothing' setting was changed from medium to high, which also increased

the resolution of the mesh. The mesh had 197,311 elements and 298,441 nodes. Each node has 6 degrees of freedom (transverse movement in the X, Y, and Z directions and rotational movement about the X, Y, and Z axes). Therefore, the mesh had 1,790,646 degrees of freedom. The resulting mesh can be seen in Figure 3.7.
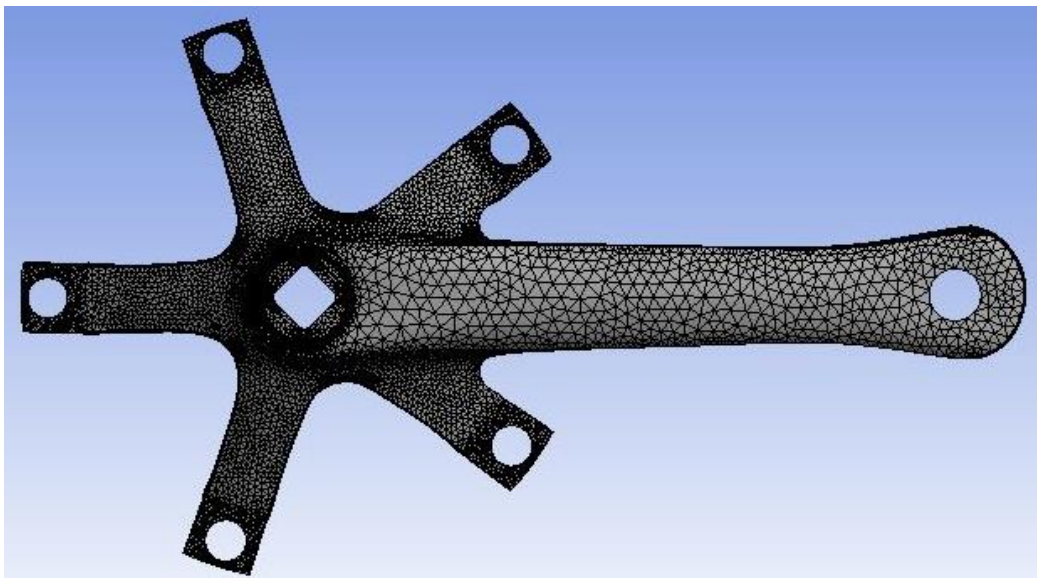
Figure 3.7: FEA Mesh

Next, the boundary conditions were applied to the model. The pedal force was applied to the interior geometry of the pedal hole, and the forces were divided into separate X and Z force vectors. The pedal moment was also applied to the interior geometry of the pedal hole, and the X axis was selected as the axis of rotation. Next, the axle moment was applied to the diamond-shaped interior void located in the

middle of the spider. Finally, separate fixed supports were applied to each of the five spider holes. The applied boundary conditions can be seen in Figure 3.8.
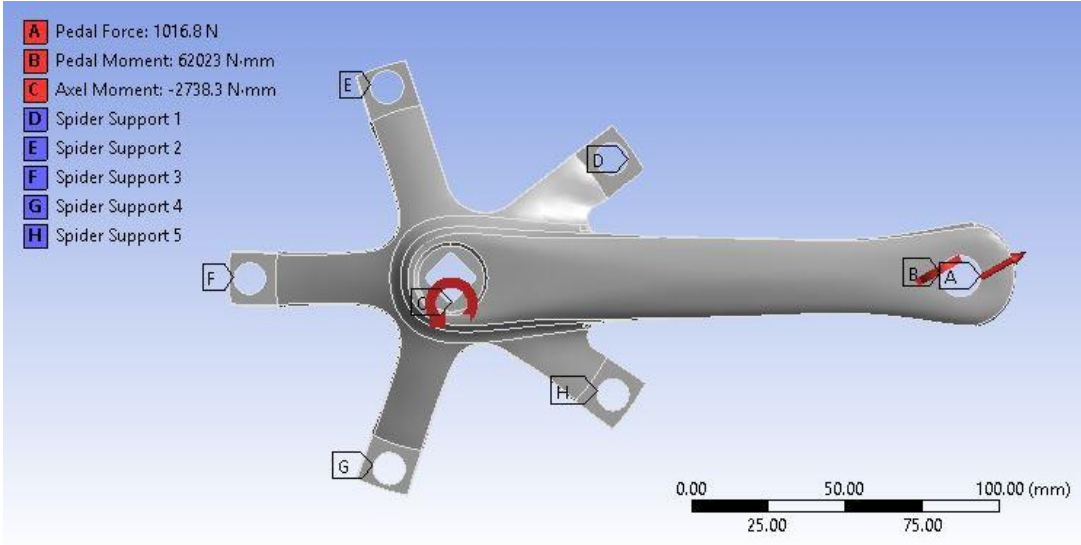
Figure 3.8: FEA Boundary Conditions

After the boundary conditions were applied to the system, the desired solution elements were added to the study. Under the solution tab, equivalent stress, normal stress (along the x axis), total deformation, directional deformation (vertical, horizontal, and lateral), equivalent strain, and normal strain (along the x axis) were added to the solution tab of the experiment.

The first analysis was conducted under the loading conditions that correspond with a crank angle of -45°. Four load steps were used to simulate these loading conditions. The force values applied during step one can be seen in Figure 3.8. A second analysis was conducted with the loading conditions that corresponded to the crank angles under consideration. 12 angles were analyzed ranging from 90° to -75°

in increments of 15°. The forces at -90° were not considered for this model because the final crank angle

(θ) equaled -105°, which is out of the range of this study (90° to -90°). 48 steps were used to define the

loading conditions at each corresponding angle (four steps per angle). Steps 1, 5, 9, etc. were used to

define the down-stroke loading conditions, and steps 3, 7, 11, etc. were used to define the up-stroke

loading conditions. The two studies were then solved based upon their respective boundary conditions.

The results from the FEA study can be seen in section 4.1 on page 92.

3.3.2 Topology Optimization

The results from the first FEA study were then imported into ANSYS's topology optimization

module. The optimization module used the previously defined boundary conditions and the solution

elements from the first FEA to define the optimization study. First, the optimization region and the

exclusion regions were defined. The optimization region included the entire body, and the exclusion

region consisted of the boundary conditions plus other critical geometrical areas. These regions can be

seen in Figure 3.9.
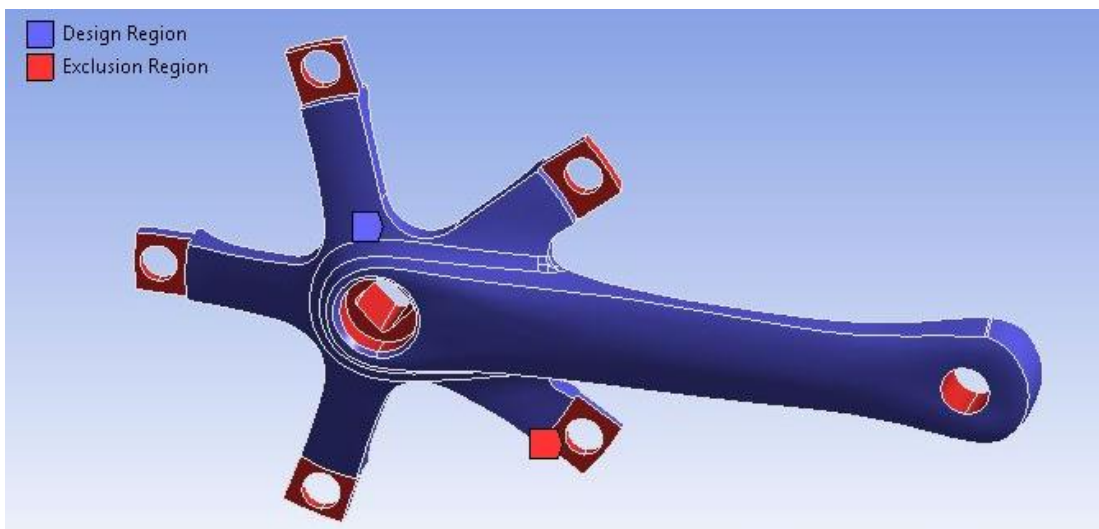
Figure 3.9: Optimization Regions

Next, the optimization objectives were defined. The objectives of this study were to minimize compliance during steps 1 and 3. Several additional parameters were then added to the study. First, a mass constraint was added and set to retain 50% of the original mass. A global von-Mises stress constraint of 250 MPa, which is 50% of the 500 MPa yield strength, was also added. This maximum stress constraint of 250 MPa was implemented into the design process so that the final design would have a factor of safety equal to 2. Finally, a minimum member size constraint of 8 mm was applied to the model. The study was then solved based on the objectives and the parameters. The resulting geometry can be seen in Figure 3.10 and Figure 3.11.
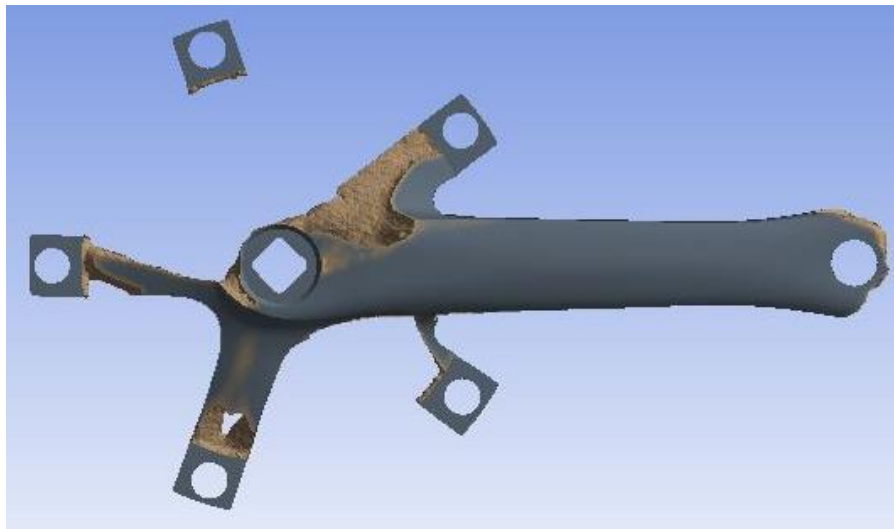
Figure 3.10: Top View of the Optimized Crank Arm

Figure 3.11: Front View of the Optimized Crank Arm

Additional results from the topology optimization study can be seen in section 4.1.2 on page 95.

3.3.3 Design Verification

Two separate design validation studies were performed on the optimized crank arm. The first validation study analyzed the original optimized body. The second validation study analyzed the geometry that had been redesigned using design for metal additive manufacturing (DFMAM) principles. The two optimized crank arms could then be compared back to the original crank arm to consider how optimization study affected the performance of each crank arm.

For the first validation study, the optimized geometry was transferred to a design validation static structural module in ANSYS Workbench. From this module, ANSYS SpaceClaim was opened to smooth and refine the faceted optimized geometry. As seen in Figure 3.10, the optimization study determined that the geometry of spider leg #2 was not needed. Therefore, the faceted geometry of Spider leg #2 was removed (see Figure 3.12).
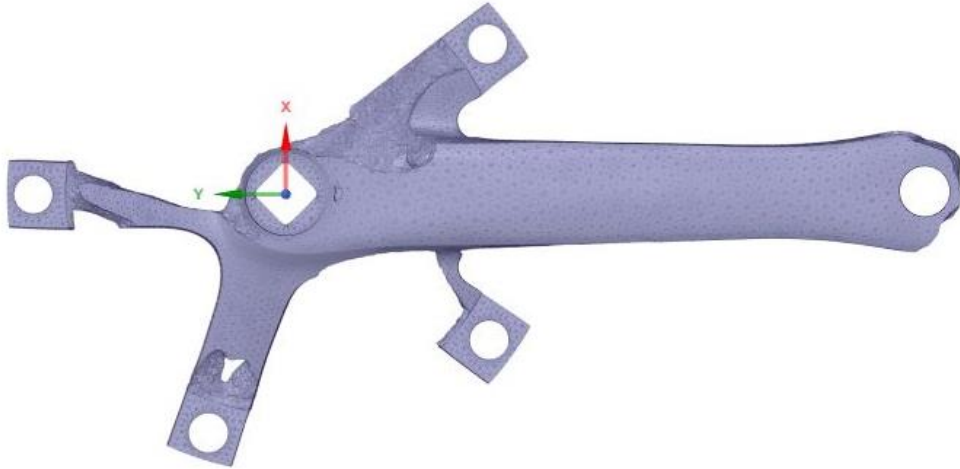
Figure 3.12: Removal of Spider #2

Next, a shrinkwrap tool was applied to the geometry (see Figure 3.13). The shrinkwrap tool removes small gaps that may occur between adjacent facets. As the name implies, the shrinkwrap tool creates a faceted wrap around the model that closes gaps according to the specified size. For this model, a gap size of 1 mm was used, the preserve features tab was selected, and the angle threshold was set to 60°.
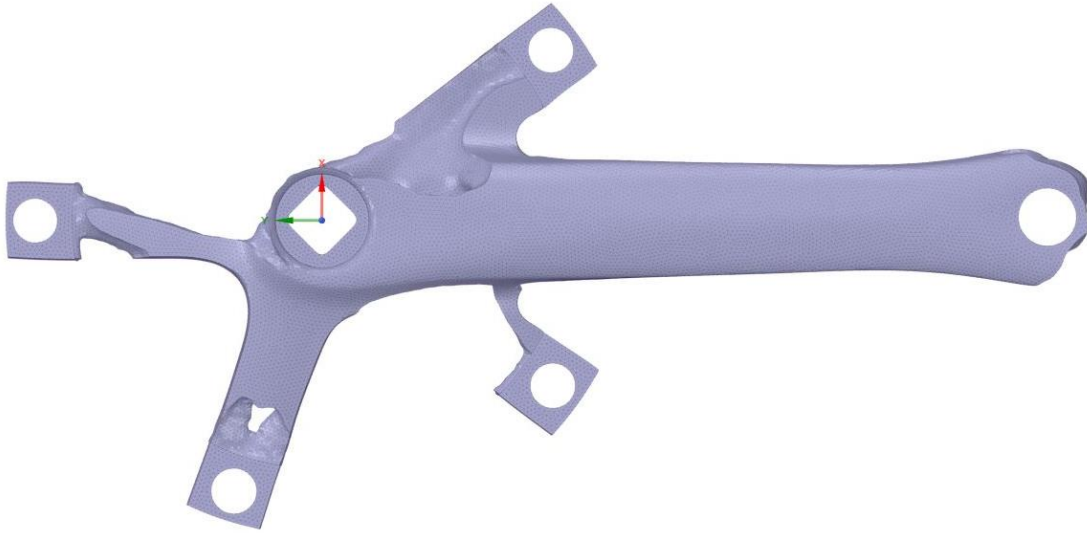
Figure 3.13: After application of the Shrinkwrap tool

Next, the mating geometries (spider holes and pedal hole) were edited to ensure that the

dimensions had not changed during the optimization process. Using the cylinder tool, solid bodies were

created within these holes (see Figure 3.14). The spider holes were changed to equal 10.4 mm in

diameter, and the diameter of the pedal hole was set to 13.3115 mm. During a later step, these solid

bodies will be subtracted from the crank arm, thus creating correctly dimensioned features with clean and

sharp edges.
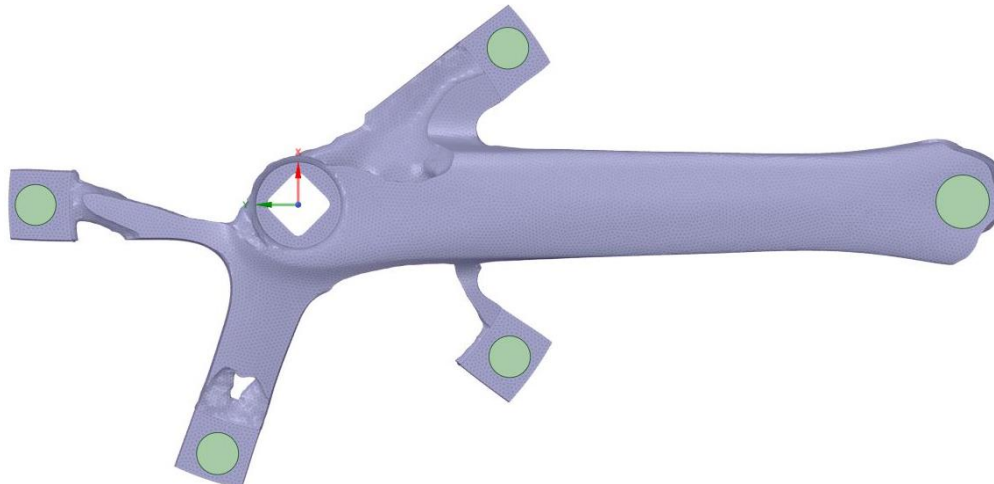
Figure 3.14: Resizing of Mating Geometries

Two smoothing operations were performed to smooth the faceted shrink-wrapped model. First, an approximate smooth was used to create more facets within the body. Next, a local smooth was used to smooth any remaining jagged edges. This local smooth was performed several times until the results were satisfactory. The resulting geometry is displayed in Figure 3.15.
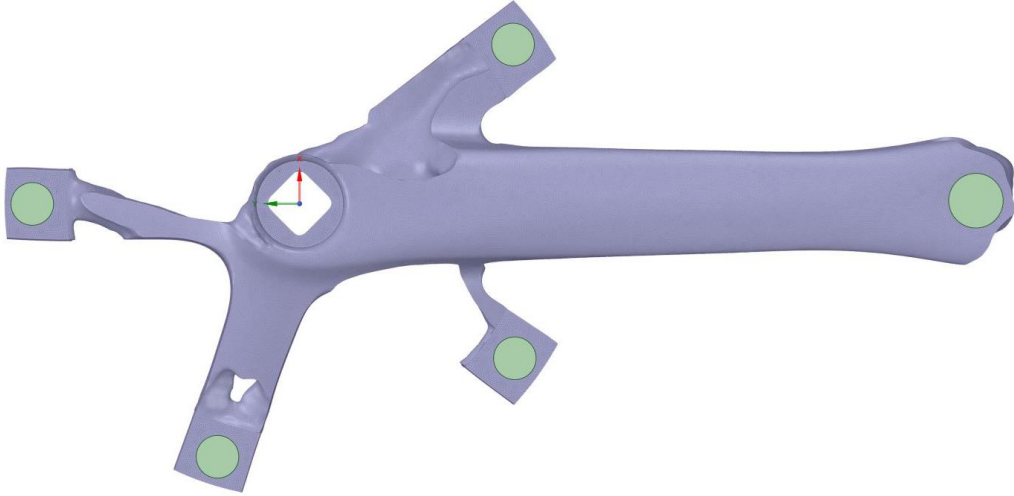
Figure 3.15: Smoothed Geometry

The solid bodies shown in Figure 3.14 were then subtracted from the faceted body. This resulted

in properly dimensioned features with sharp edges (see Figure 3.16).
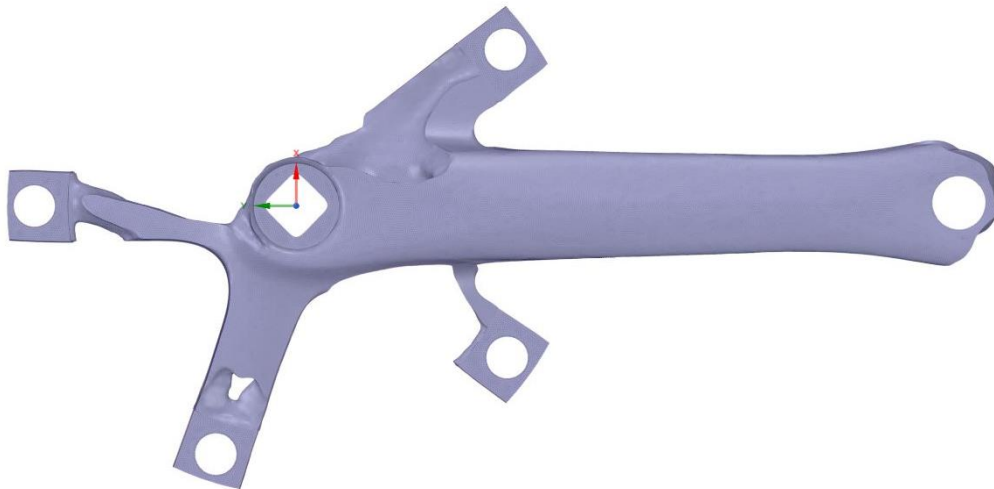
Figure 3.16: Finalized Mating Geometries

Next, the fix sharps tool was used to fix any remaining sharp edges. The check facets tool was then used to check for errors within the geometry, and the fix facets tool was used to fix any errors. Finally, the faceted body was converted into a solid body so that it could be imported into the design validation static structural module.

Within the FEA module in ANSYS Mechanical, the solid body was converted into virtual topology. According to the ANSYS help page, virtual topology represents all definitions of face or edge groups, and all definitions of virtual split edges, virtual split faces, and virtual hard vertices within a model [37]. Without the use of the virtual topology tool, boundary conditions could not be applied to the optimized solid body. The virtual topology can be seen in Figure 3.17.
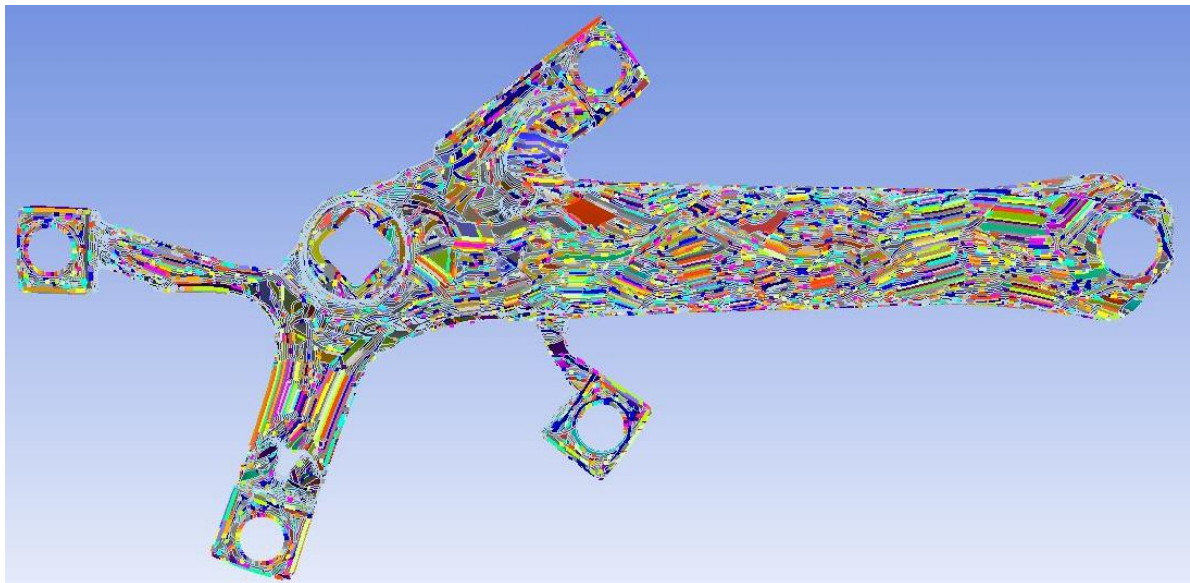
Figure 3.17: Virtual Topology

After the virtual topology was created, the stainless-steel material was reassigned to the optimized body. Next, a mesh was applied to the model using the same settings that were previously discussed in section 3.3.1 on page 35. This validation mesh can be seen in Figure 3.18.

Figure 3.18: Validation Mesh

Except for the fixed support located on spider leg #2, the same boundary conditions from section 3.3.1 were then added to the model. Because the validation static structural module is connected to the original static structural module, the solution elements did not need to be reapplied. The study was then solved to determine how the optimized model would perform under the loading conditions. The results from this analysis are shown in section 4.1.3 on page 96.

As previously mentioned, a second design validation study was needed to apply DFMAM principles to the optimized geometry to increase the printability of the crank arm. First, the build orientation of the part was considered. Because this research only required the fabrication of two crank arms (the original crank arm and the DFMAM optimized model), the part was oriented to reduce the height of the object in the Z direction while still being able to print the necessary features. Because the shaft of the crank arm was hollow, it was determined that the crank arm would be printed horizontally, which is the orientation of the crank arm shown in Figure 3.10. However, if a larger volume of parts were needed, it would be more efficient to print the crank arm standing up vertically so that more parts could be fabricated in a single printing operation. Therefore, the optimized geometry was edited according DFMAM principles to increase the part's manufacturability.

Like the first validation study, the original optimized body was transferred to a separate design validation static structural module in ANSYS Workbench. From this module, ANSYS SpaceClaim was opened to edit the geometry according to DFMAM principles. First, the faceted geometry that comprised spider leg #2 was deleted. Figure 3.19 displays the resulting geometry, and the figure also shows the internal hollow cavity within the shaft. In order to print the crank arm in the orientation shown below, the internal overhanging features must be eliminated so that the internal cavity is not filled with support material.
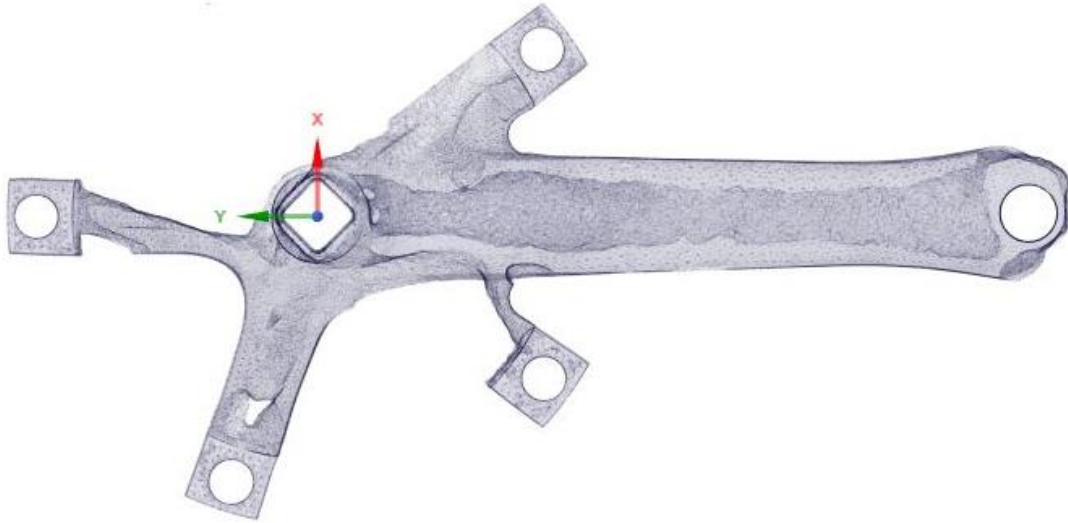
Figure 3.19: Removal of Spider #2 and Transparent View

Therefore, the top of the internal channel was changed to have a diamond-shaped cross-section. A swept blend, which creates a solid body by joining together multiple cross-sectional sketches, was used to change cross-section of the internal void. Seven sketches were used within the swept blend to create the proper solid body. Two of the cross-sectional sketches are shown below in Figure 3.20 and Figure 3.21. Figure 3.22 displays the summation of the seven cross-sectional sketches.
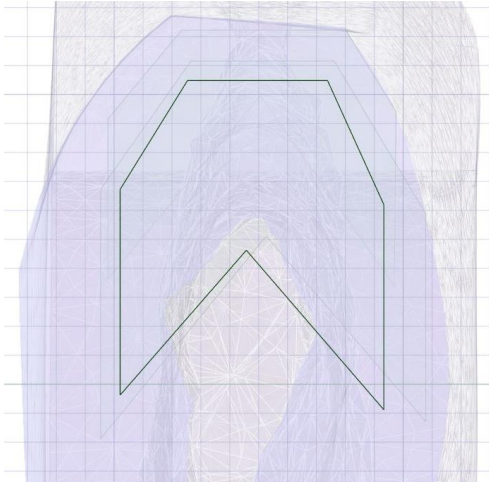
Figure 3.20: Internal Cross-Sectional Sketch #1
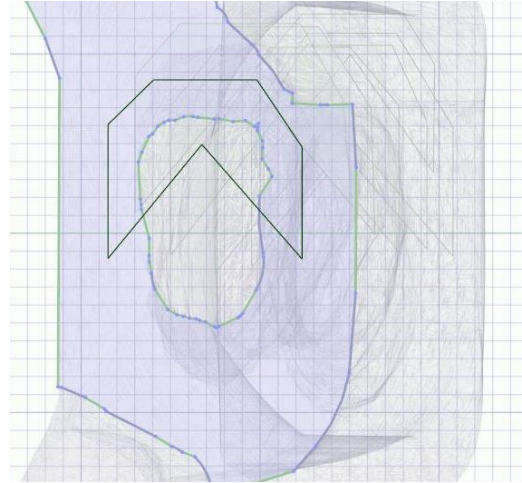
Figure 3.21: Internal Cross-Sectional Sketch #2
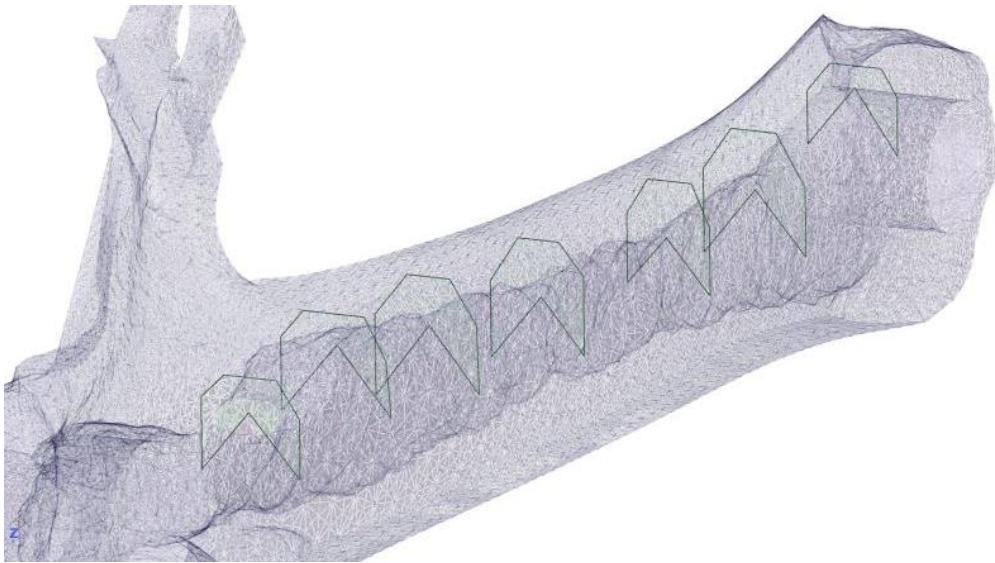
Figure 3.22: Summation of Cross-Sectional Sketches

By using the swept blend tool under the design tab, a solid body was created by joining together each cross-sectional sketch. This solid body can be seen in Figure 3.23.
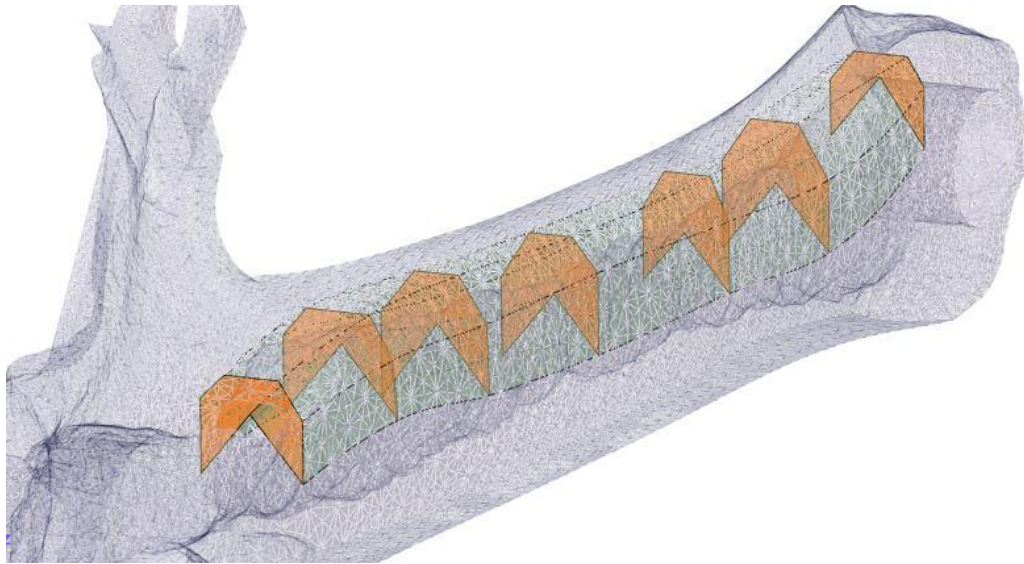
Figure 3.23: Interior Solid Body

Next, the geometry of spider leg #5 was also enhanced by using a swept blend. Only two sketches were used to create the necessary improvements. The new resulting geometry can be seen in Figure 3.24.
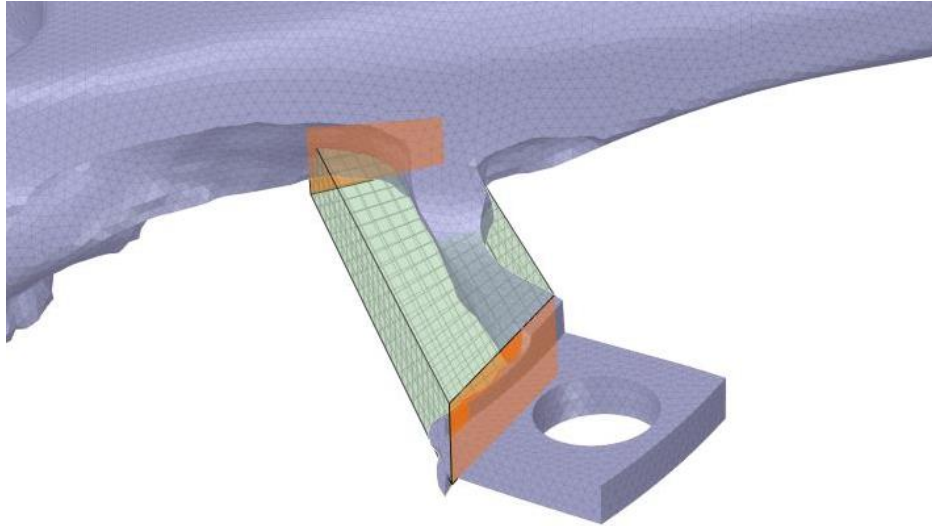
Figure 3.24: Spider leg #5 Enhancement

Next, the cylinder tool was used to thicken the geometry surrounding the axle hole. Two separate cylinders were used to enhance the axle hole geometry, and the shell command was used to remove the interior material of the cylinders. The resulting features are displayed in Figure 3.25.
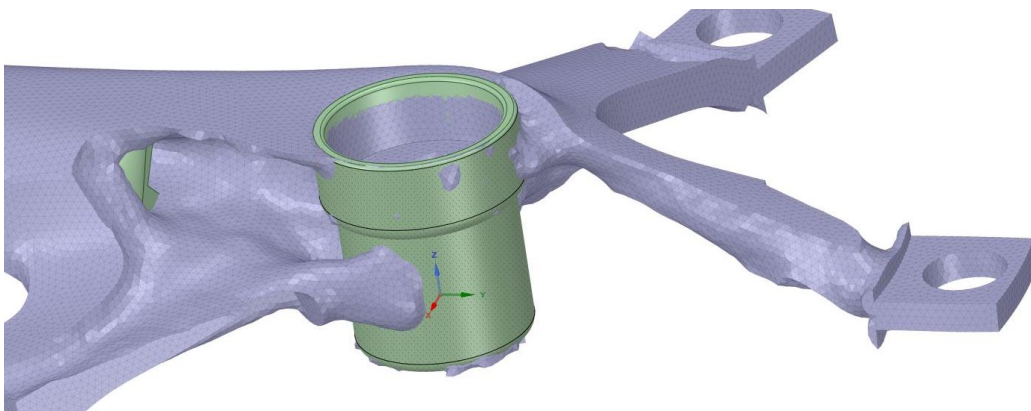
Figure 3.25: Enhancement of Axle Geometry

Finally, a small supporting structure on the underside of the crank arm was repaired with a rectangular solid body. Figure 3.26 displays the original problematic supporting feature, and Figure 3.27 displays the repaired structure.
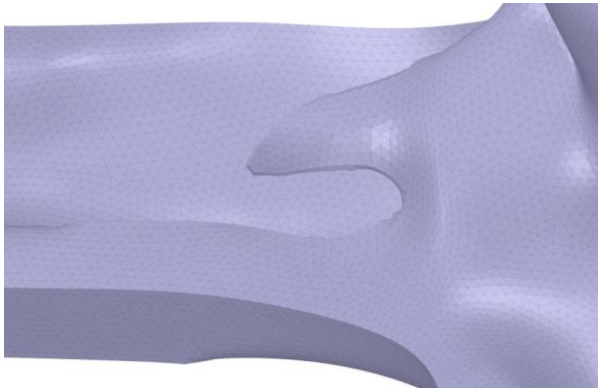
Figure 3.26: Problematic Structure
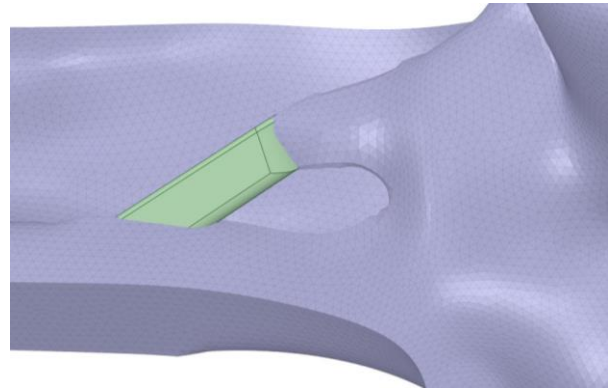
Figure 3.27: Repaired Structure

Like the first design validation study, the cylinder command was used to insert solid bodies into the pedal hole and the spider hole geometries. These solid bodies were inserted to ensure the holes were the correct size and to keep the shrinkwrap tool from rounding the corners of the holes. The pull tool was used to set the diameter of the pedal hole to 13.3115 mm and the spider holes were changed to equal 10.4 mm in diameter. The resulting solid bodies are displayed in Figure 3.28.
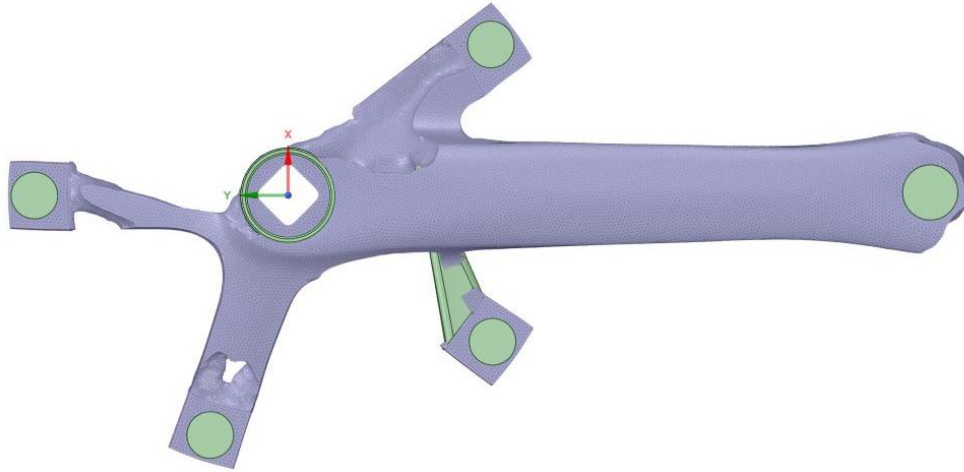
Figure 3.28: Solid Bodies

The merge tool was then used to merge the interior diamond-shaped feature, spider leg #5's supporting body, the two cylinders surrounding the axle geometry, and the rectangular body that was used to enhance the small supporting structure into the faceted body. Next, the solid geometries inside of the mating holes were subtracted from the faceted body, thus creating properly dimensioned interior features. The shrinkwrap tool was then used to create a faceted wrap around the model to close any existing gaps in the model. For this shrinkwrap, a gap size of 1 mm was used, the preserve features tab was selected, and the angle threshold was set to 60°. Two separate smoothing operations were then used to refine the faceted shrink-wrapped body. First, an approximate smooth was used to refine the size of the faceted triangles. Next, a local smooth was used to smooth any remaining course features. The fix sharps command was used to smooth the remaining sharp edges of the model. Finally, the body was examined for errors by using the check facets tool. The resulting geometry was then converted into a solid body so that it could be imported into the design validation static structural module.

Within the FEA module in ANSYS Mechanical, the solid body was converted into virtual topology. Without the use of the virtual topology tool, the boundary conditions could not be applied to the optimized solid body. The resulting virtual topology can be seen in Figure 3.29.

Figure 3.29: DFMAM Virtual Topology

After the virtual topology was created, the stainless-steel material was reassigned to the optimized body. Next, a mesh was applied to the model using the same settings discussed in section 3.3.1 on page 35. This validation mesh can be seen in Figure 3.30.

Figure 3.30: DFMAM Validation Mesh

Except for the fixed support located on spider leg #2, the same boundary conditions from section 3.3.1 were then added to the model. Because the validation static structural module is connected to the original static structural module, the solution elements did not need to be reapplied. The study was then solved to determine how the DFMAM optimized model would perform under the loading conditions. The results of the analysis are displayed in section 4.1.3.2 on page 99.

3.4 Experimental Analysis

The following section describes the methods that were used to fabricate the crank arms with the EOS M 290 Direct Metal Laser Sintering (DMLS) additive manufacturing machine. Also discussed are the methods used to design the testing apparatus and the connecting rod assembly along with the processes used to fabricate both structures. Finally, this section explains the methods that were used to physically test the crank arms.

3.4.1 Fabricating the Crank Arms

After the theoretical simulations had been completed, the EOS M 290 was used to fabricate both the original crank arm and the DFMAM optimized crank arm. First, ANSYS SpaceClaim was used to

save the solid geometries of the crank arms as STL files. Materialise Magics, a versatile data preparation and STL editing software for additive manufacturing, was then used to orient the part and create the support material for both crank arms [38]. EOS Print 2.0 was used to orient the parts on the build platform of the M 290.

First, the STL files were imported into Materialise Magics to orient each part, generate the necessary support structures, and manipulate the support structures to reduce the amount of part-on-part support material. The optimized crank arm was oriented so that the shaft of the crank was near horizontal relative to the build platform (see Figure 3.31). Next, the necessary block support structures were generated within the software. The support structures were then manipulated to increase the printability of the structure and the reduce the amount of post processing. For example, the base of the thin support structures was changed to keep the structures from being pushed over by the recoater blade. The resulting structures were transformed from thin vertical structures to triangular structures. Next, several support structures were angled to reduce the amount of part-on-part support (see Figure 3.33).
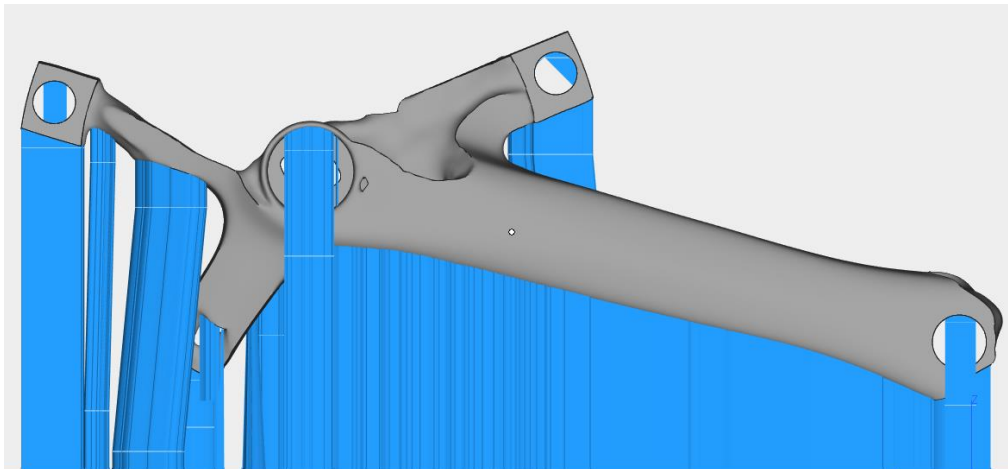
Figure 3.31: Front View of Support Structures
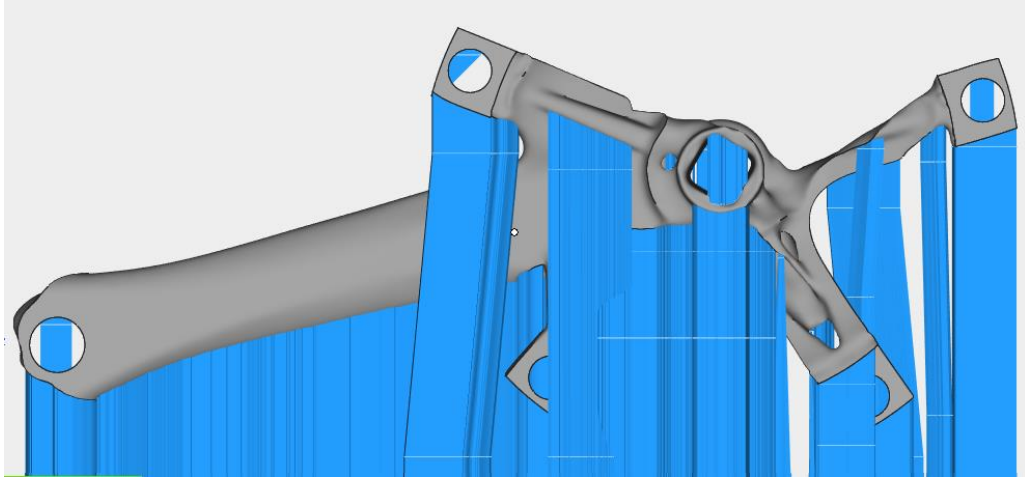
Figure 3.32: Back View of Support Structures
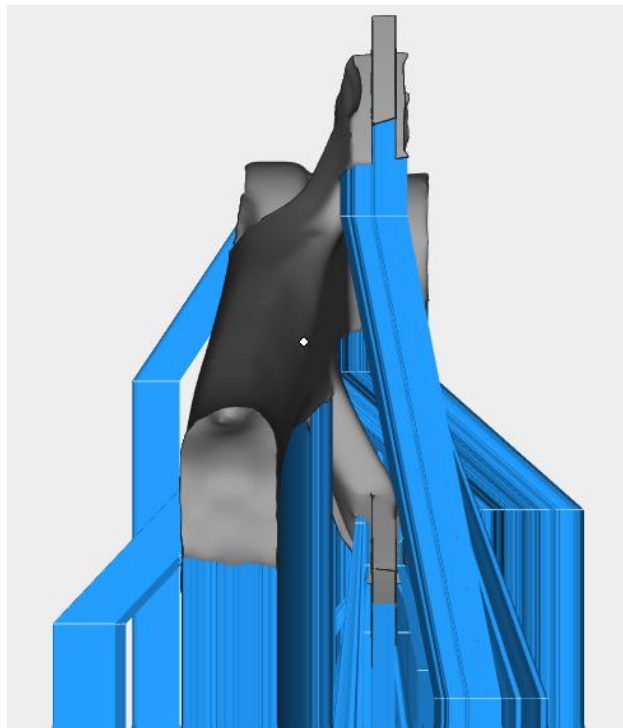
Figure 3.33: Right View of Support Structures

This process was then repeated for the original crank arm, which is shown below in Figure 3.34.
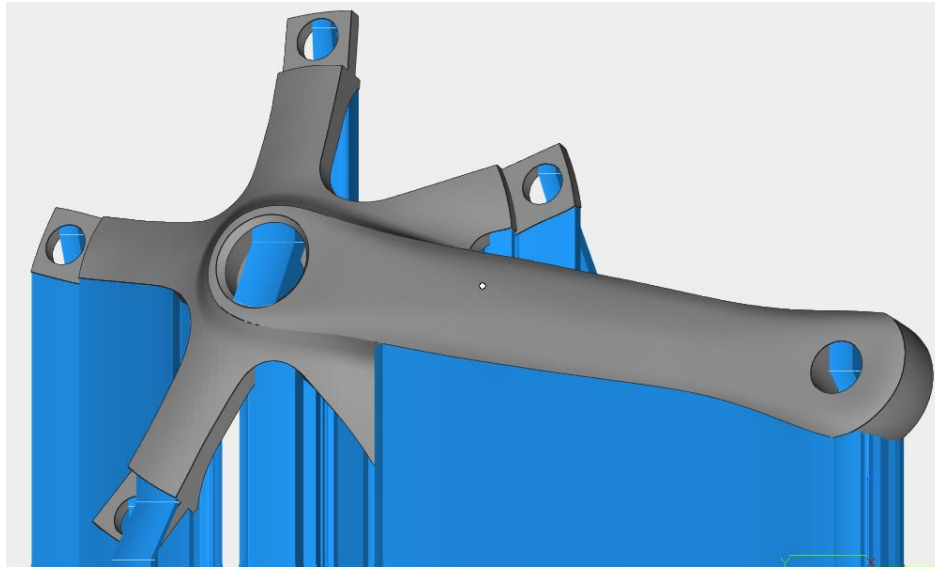
Figure 3.34: Applied Support Material to Original Crank Arm

The two parts were then imported into EOS Print 2.0 to be placed on the build plate (see Figure 3.35). According to the DFMAM guidelines previously mentioned in section 2.3.1 on page 8, the crank arms were orientated at a slight angle so that the recoater blade would not strike parallel to the crank arms. The parts were also placed on the build platform so that they were not in a straight line. Therefore, if one part failed, the remaining crank arm would not be affected by the failure of the first part. The build files were then transmitted to the EOS M 290 to be manufactured.
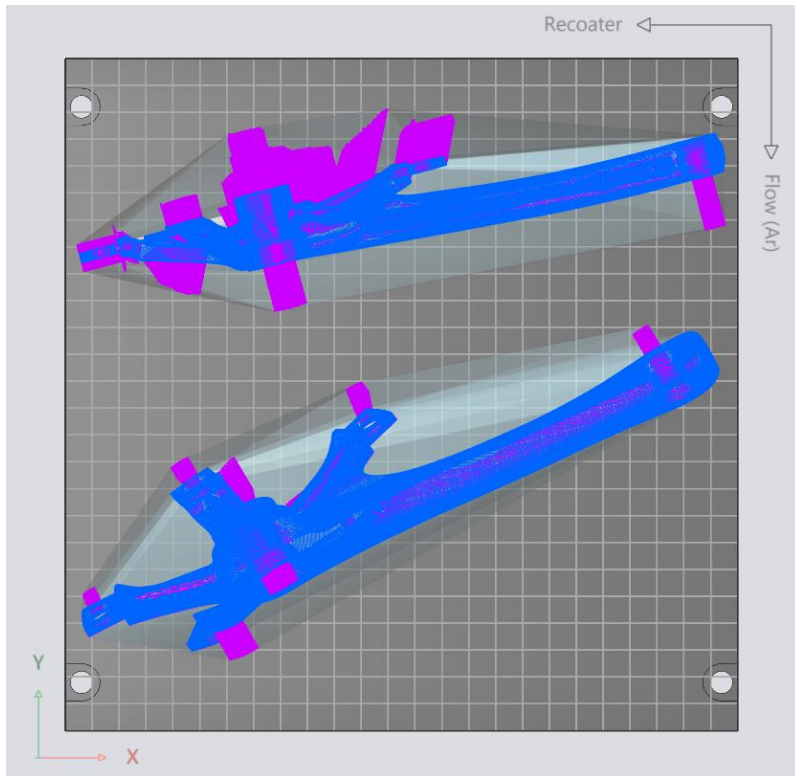
Figure 3.35: Build Plate Part Orientation

The optimized crank arm printed successfully, but the original crank arm failed because the
recoater blade collided with the support structure. This problem is further discussed in section 4.2.1.
Because the original crank arm failed to print, a secondary printing operation was needed. The original
crank arm was imported into Magics and oriented in such a way to reduce the overall height of the build
(Z axis). The crank arm was also oriented to reduce the amount of support structures on complex
geometries. The resulting print orientation and support material is shown in Figure 3.36.
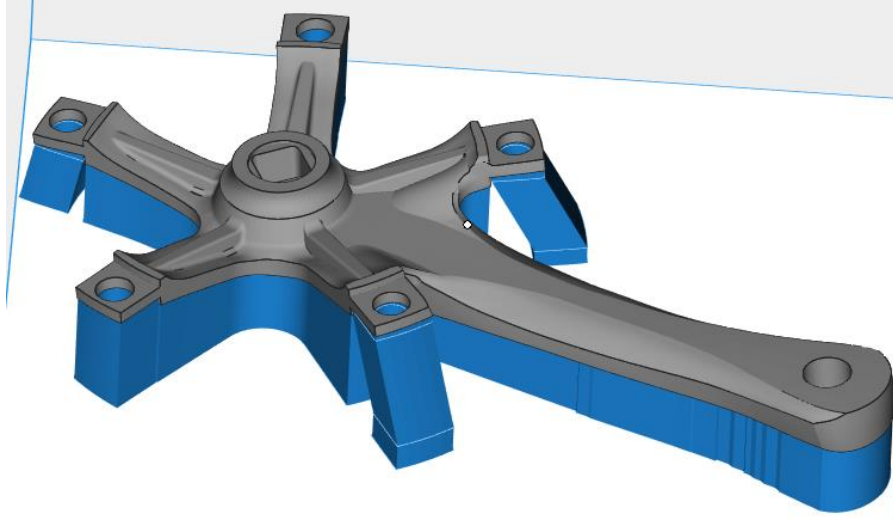
Figure 3.36: Orientation and Support Structures of the Original Crank Arm

The part was then imported into EOS Print 2 to orient the part on the build platform. The part was slightly rotated to keep the recoater blade from colliding with the part according to DFMAM guidelines. The final part orientation can be seen in Figure 3.37. The build file was then transmitted to the EOS M 290 to be manufactured. The fabricated crank arms can be seen in section 4.2.1.
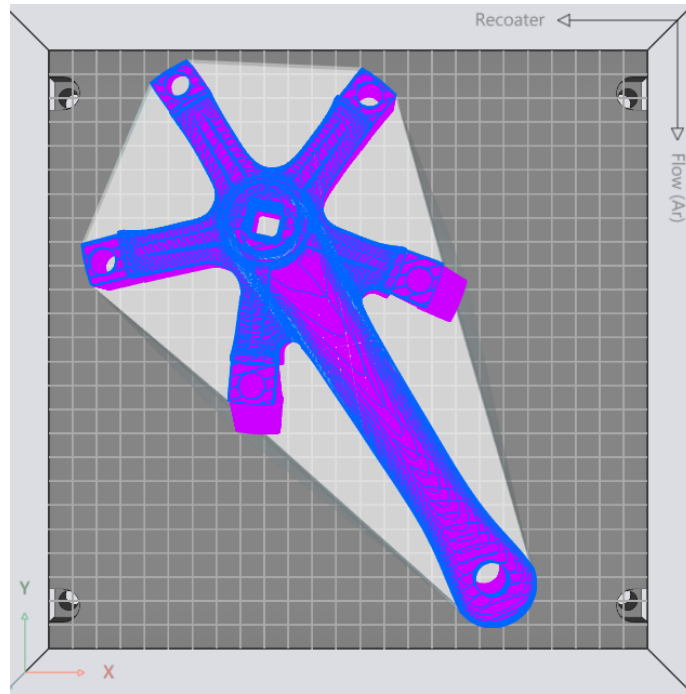
Figure 3.37: Build Plate Orientation of Print the Second Printing Operation

3.4.2 Design of the Testing Apparatus

The objective of the test fixture was to hold the crank arm in the Instron 5967 universal testing machine so that the crank arm could be tested. The fixture had to allow the crank arm to be tested at various angles that correspond with the previously calculated loading conditions. Because the tensile tester can only apply forces along a vertical axis (Z axis), the apparatus also needed to be able to move horizontally to ensure that the force would be applied at the proper angle. The assembly must also be structurally rigid so that it does not deflect during testing. Due to the capabilities of the Haas Z4 500 laser cutter, the testing apparatus was designed to be constructed with ¼" steel plate. The 3D CAD model of the structure is shown below in Figure 3.38.
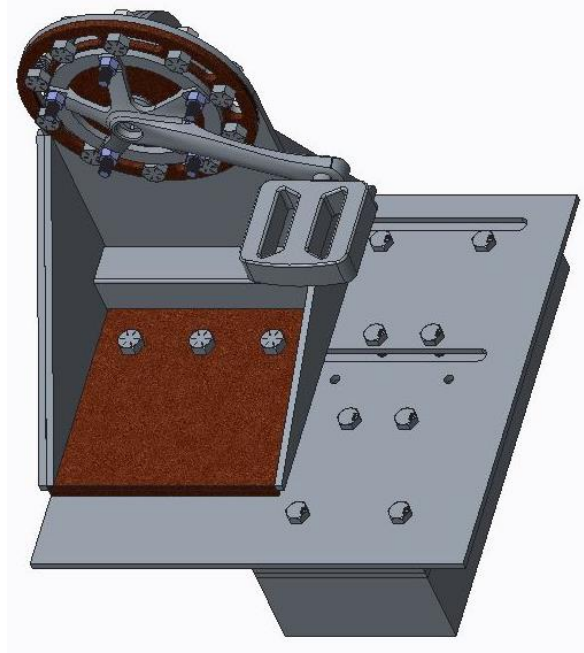
Figure 3.38: 3D CAD model of the Testing Apparatus

The first problem to be solved during the design process concerned the rotational movement of the crank arm. First, a circular plate was created to match the bolt-hole pattern of the spider geometry on the crank arm (see Figure 2.9). This enabled the crank arm to be bolted to the circular plate. Next, a vertical crank mounting plate was created so that the crank arm could be held perpendicular to the test platform. 10 slots were then cut in both the circular plate and the vertical crank mounting plate. These slots were designed to be 12.7 mm wide to allow a standard ½" bolt to fit within the slots. Bolts were used to clamp the circular plate to the crank mounting plate. The friction caused by the clamping force from the bolts was designed to keep the two pieces from rotating during testing. To adjust the angle of the crank, the user would first loosen the bolts, rotate the crank arm to the desired angle, and finally tighten the bolts.

When the crank arm rotates, the coordinates of the hole where the pedal is attached to the crank changes. Therefore, the fixture must be able to move horizontally in the X direction to keep the center of the pedal aligned with the vertical loading axis of the tensile tester. To achieve this horizontal motion, two 12.7 mm wide slots were cut at a length of 300 mm in the stationary base plate. Five holes were cut in the movable base plate that corresponded with slots in the stationary base plate. Therefore, to align the pedal underneath the vertical axis, the operator must loosen the five bolts, align the structure, and tighten the bolts.

Not only does the center of the pedal need to be aligned with the vertical loading axis of the tensile tester in the X direction, but it also needs to be aligned in the Y direction. Therefore, to align the pedal underneath the vertical axis in the Y direction, the crank mounting plate was shifted off-center by 101.825 mm. The vertical red rod in Figure 3.39 represents the load path of the tensile tester. As shown in the following figure, the load path travels through the center of the pedal in both X and Y directions.
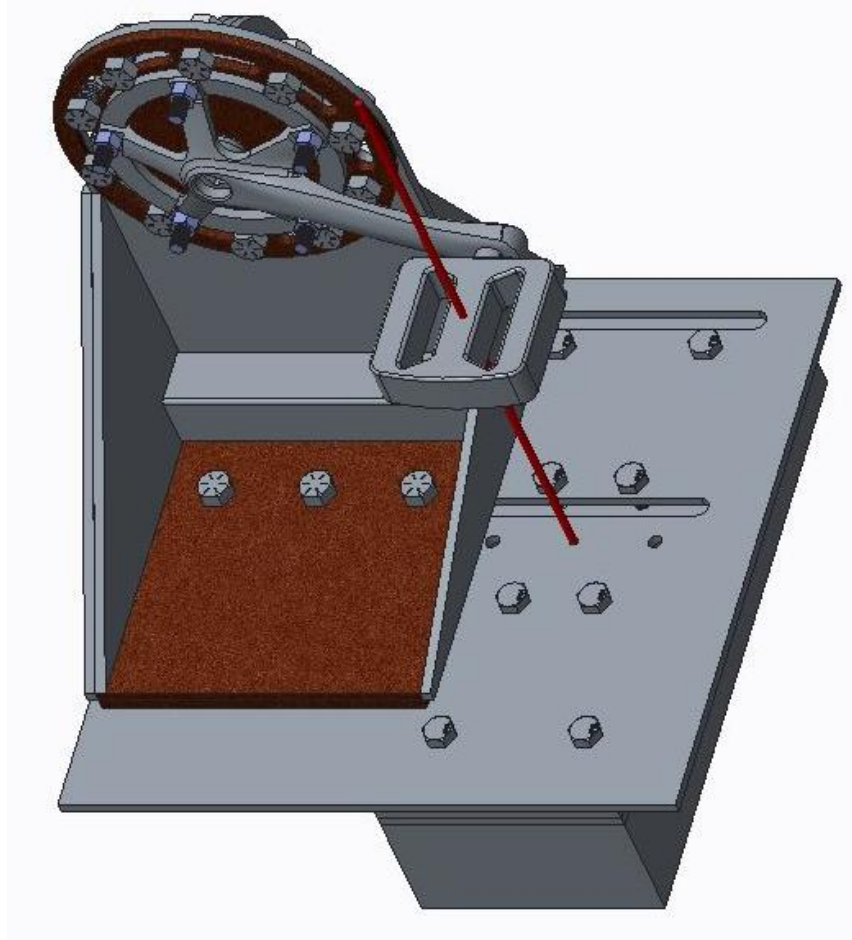
Figure 3.39: Load Path of the Tensile Tester

Next, the bolt-hole pattern on the base of the Instron tensile testing machine was measured and transferred to the stationary base plate. According to the Instron 5960 series manual, the bolt holes on the base of the tensile tester required M10 x 1.5 bolts [39]. Therefore, the bolt holes on the stationary base plate were designed to be 10 mm clearance holes. These bolts enabled the test fixture to be securely attached to the base of the tensile tester. A wooden test piece was cut by the laser cutter to verify that the bolt-hole pattern was correctly measured. Figure 3.40 shows the wooden test piece used to verify the bolt-hole pattern.
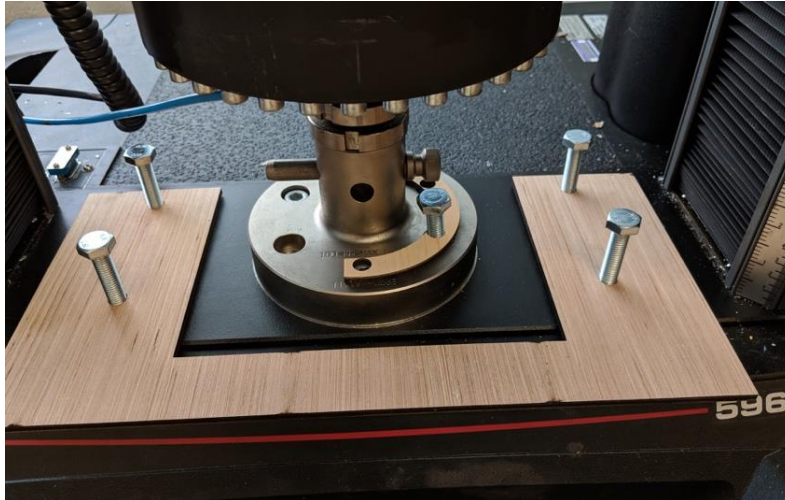
Figure 3.40: Bolt-Hole Pattern Measurement Verification

Two ¼" steel plates with slots that correspond to the bolt holes on the adjustable mounting plate were added between the stationary base plate and the base of the tensile tester to allow the operator enough room to use a wrench to tighten the bolts. These two plates can be seen below in Figure 3.41.
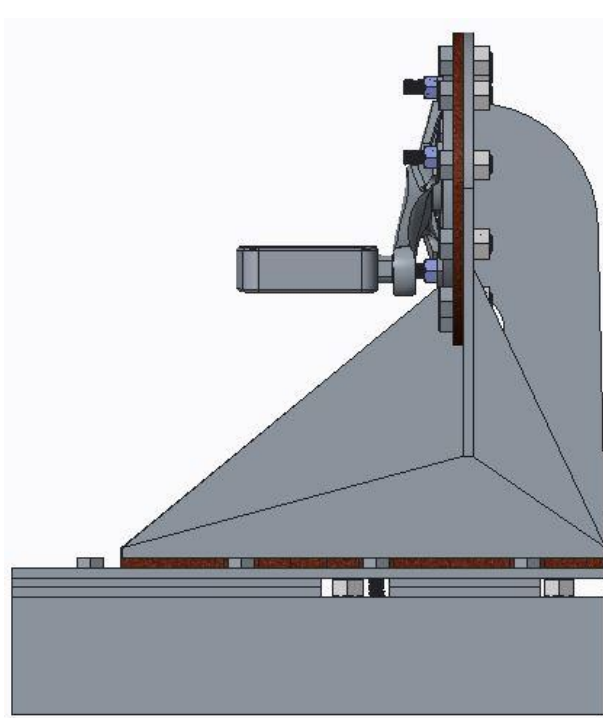
Figure 3.41: Right View of the Test Structure

Multiple support structures were then added to keep the vertical crank mounting plate from bending during loading. Each of the support triangles are attached to the vertical crank mount and to the moveable base plate. The front support triangle was designed to be short so that the crank arm would be allowed to freely rotate without obstruction. Because the crank arm will only be tested from 90 degrees to -90 degrees, the rear support triangle was designed to be taller and more supportive. The square tubing located at the bottom of the vertical crank mount was designed to add rigidity to the base of the structure. Finally, several additional support structures were added to the back side of the vertical crank mounting plate to reinforce the plate. These support structures can be seen below in Figure 3.42.
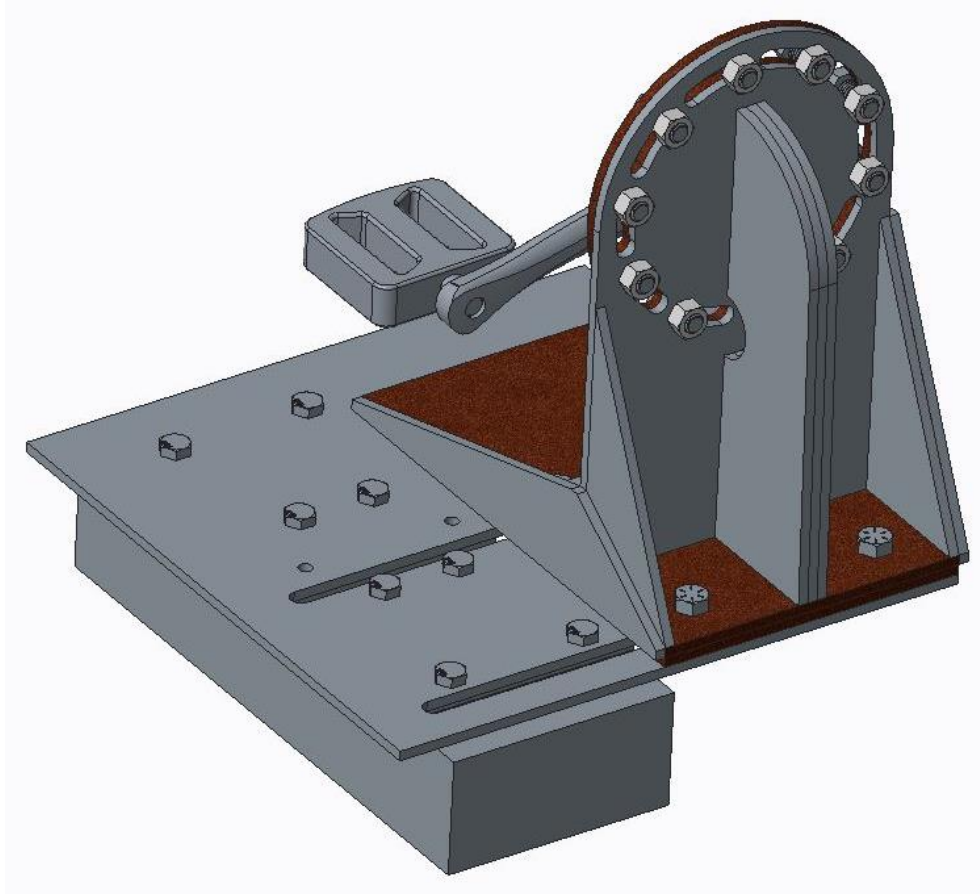
Figure 3.42: Rear Support Structures

Finally, a bending beam calculation was performed on the stationary mounting plate to ensure the plate would not excessively deform under loading. According to R. C. Hibbeler, the maximum deflection formula for a cantilevered beam is shown in equation 3.23, where P equals the applied force, L equals the length of the beam, E equals the modulus of elasticity, and I equals the area moment of inertia [40].

$$\delta_{max} = \frac{PL^3}{3EI} \tag{3.23}$$

The force to be considered is the maximum pedal force resultant vector, which is 1016.8 Newtons. The length is measured from the center of the spider to the center of the back-most bolt hole, which is shown in Figure 3.43. This distance equals 122.5 mm.
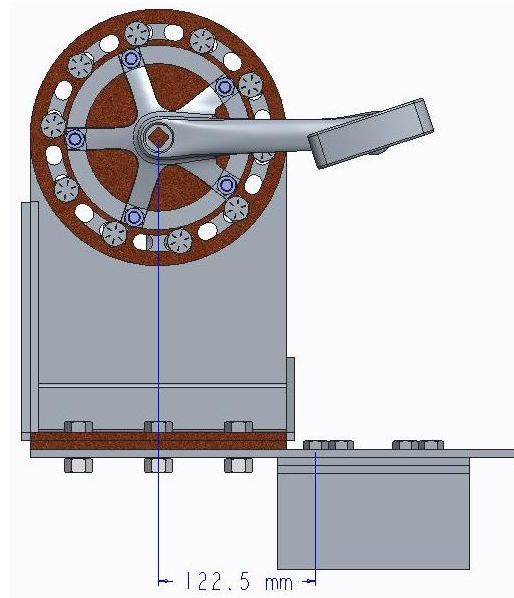
Figure 3.43: Bending Beam Length Dimension

According to R. C. Hibbeler, the modulus of elasticity of structural steel alloy is 200 GPa [40]. The area moment of inertia is calculated by using equation 3.24, where b equals the width of the base plate and h equals the thickness of the material [40]. The dimensions of the base plate are shown in Figure 3.44.

$$I = \frac{1}{12}bh^3 \tag{3.24}$$
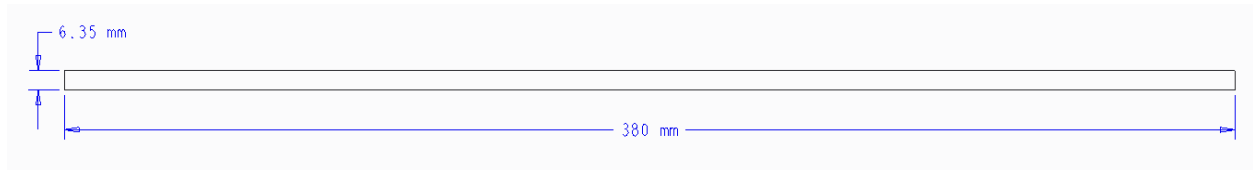
Figure 3.44: Base Plate Dimensions

Therefore, the area moment of inertia equals $\frac{1}{12} * 380(mm) * 6.35(mm)^3 = 8108.2 \ mm^4$

The maximum deflection is calculated below in equation 3.25 by using the previously stated formula (equation 3.23).

$$\delta_{max} = \frac{1016.1(N) * 122.4(mm)^3}{3 * 200E^6 \left(\frac{N}{mm^{\wedge}2}\right) * 8108.2(mm^4)} = 0.000383 \ mm \tag{3.25}$$

The base plate will only deflect 0.000383 mm under loading, thus verifying that the stationary mounting plate is of suitable thickness.

3.4.3 Design of the Connecting Rod Assembly

A connecting rod assembly was designed to connect the pedal hole on the crank arm to the load cell of the Instron tensile tester. A 3D model of the connecting assembly is shown below in Figure 3.45.

Figure 3.45: Connecting Rod Assembly

First, a steel rod was modeled to represent the original pedal shown in Figure 3.46. The distance from the center of the pedal to the center of the threaded stud is 61 mm, and the center of the threaded stud is 6 mm from the shoulder of the pin. The new pedal was designed to match these same dimensions so that the same amount of torque would be applied to the crank arm. The new pedal design is shown in Figure 3.47.
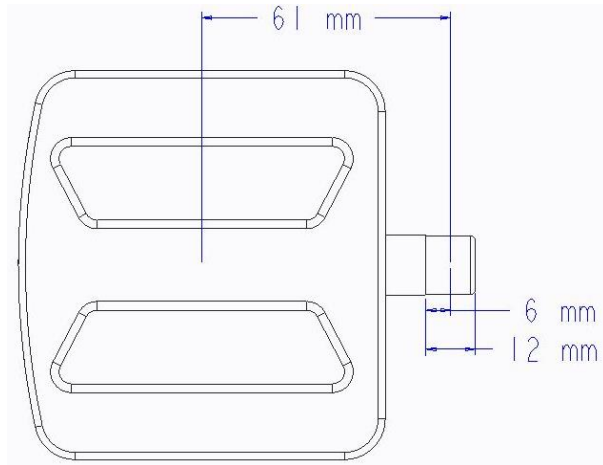
Figure 3.46: Dimensions of the Original Pedal
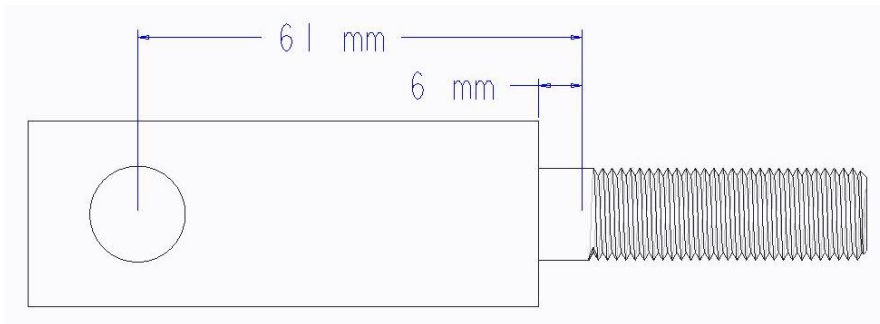
Figure 3.47: Connecting Pedal

The new pedal was designed to fit freely inside of the pedal hole of the crank arm. A nut will be threaded on the cylinder to secure the pedal to the crank arm. Next, a bracket was designed to connect the pedal to the load-bearing rod (Figure 3.48). The pivot holes on the bracket were designed so that the existing ½ inch Instron sheer pins could be used.
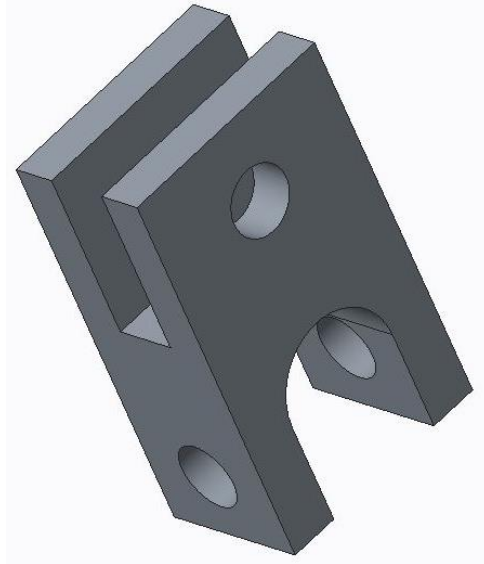
Figure 3.48: Connecting Bracket

Finally, a bar was modeled to attach the connecting bracket to the load cell of the Instron tensile testing machine (see Figure 3.45).

3.4.4 Fabricating the Test Fixture

3.4.4.1 Cutting the Test Fixture Pieces

After the design was finalized and approved, the fabrication process began. Hass's Z4 500 laser cutter was used to cut the ¼" steel stock. The laser cutter has a maximum cutting power of 500 Watts and a maximum cutting platform of 48 inches long by 18 inches wide. OneCNC was the post-processing software that was used to create the tool paths and generate the G and M code for the Haas Z4 500 laser cutter.

First, a two-dimensional Creo drawing was created that contained each of the individual parts within the assembly. Next, the drawing was saved as a DXF file, which created a 2D file that is readable by the OneCNC post-processing software. The geometry of each part and the quantity needed was then defined within the OneCNC software. Next, the parts were nested within the available stock material. The

nest feature within OneCNC determines the most optimum part orientation to minimize the amount of wasted material. After the parts were nested, the program generated the corresponding toolpaths. The power was set to the maximum 500 Watts, and the feed rate was set to 0.4 inches per minute. These toolpaths were then posted to the Haas laser cutter. Multiple steel sheets were needed to cut all the parts. Due to the slow feed rate, this cutting process took 7 days to complete.

After each sheet was cut by the laser, an angle grinder was used to cut away any remaining material that the laser did not fully cut. The angle grinder was also used to remove the slag left by the laser and to deburr the course edges. A drill bit was used to deburr the through holes to create the proper tolerances. Figure 3.49 below displays the pieces after they were cut and deburred.

Figure 3.49: Test Fixture Pieces

3.4.4.2 Assembling the Test Fixture

A Millermatic 35 MIG welder was used to assemble the test fixture. The process began by tack-welding together all the pieces to ensure proper fit and alignment. After the structure had been fully assembled with tack-welds, all the joints were bead welded. The most critical aspect of the assembly was the placement of the vertical crank mounting plate. This plate needed to be welded perpendicular to the movable base plate and it was to be offset 85 mm from the rear edge. First, digital calipers were used to mark the correct location from the rear edge. Next, a right-angled magnet was used to hold the vertical plate perpendicular to the movable base plate. A square was used to confirm that the two plates were indeed perpendicular. This arrangement can be seen in Figure 3.50. The two plates were then tack welded together.

Figure 3.50: Attaching the Vertical Crank Mounting Plate to the Movable Base Plate

Next, the two small rear support triangles were added to the assembly. The right-angled magnet was used to hold the two triangles in position while the tack weld was applied. This step is shown below in Figure 3.51.

Figure 3.51: Attaching Rear Supports

Next, the front support triangle and the two full-length support triangles were added. Each piece was held in place using the right-angled magnet and then tack welded to the adjacent structure. The addition of these pieces can be seen in Figure 3.52.
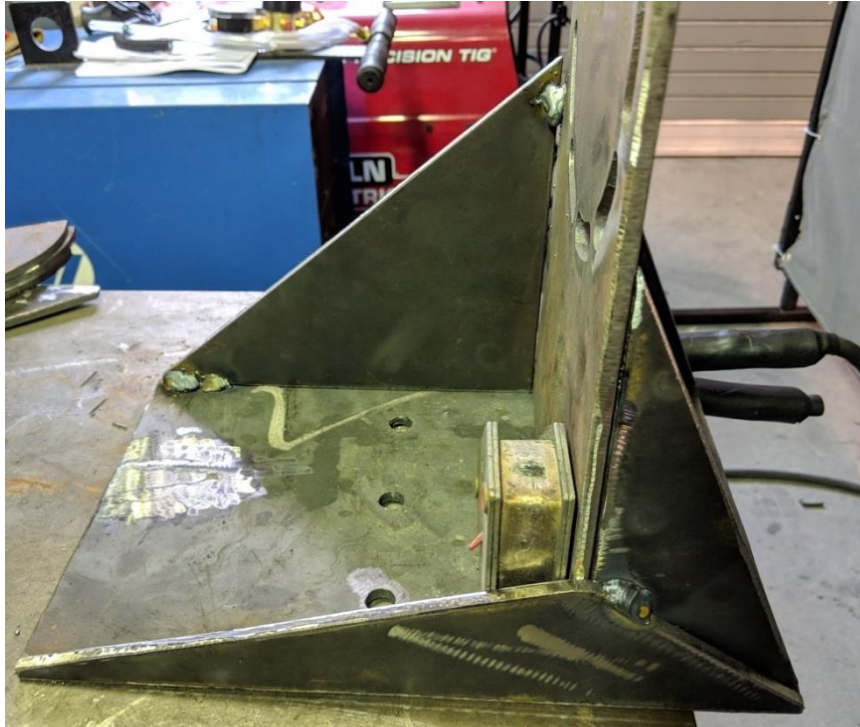
Figure 3.52: Attaching Additional Support Triangles

The three support ribs were then attached to the back side of the vertical crank mounting plate. The first rib was placed 6.35 mm from the center of the movable base plate and held in place with the right-angled magnet, which is displayed in Figure 3.53. Next, the second rib was added adjacent to the first rib. Finally, the third rib was attached to the second rib, which is shown below in Figure 3.54. Both the second and third ribs were initially secured with a C-clamp before they were tack welded to the adjacent structure. Each rib was tack welded to the surrounding structure.

Figure 3.53: Positioning of Rib #1

Figure 3.54: Addition of Ribs #2 and #3

Next, a section of square tubing was cut to size so that it would fit between the two front support triangles. This tubing was placed at the base of the vertical crank mounting plate to add additional support. The tube was initially tack welded to ensure proper alignment.

Figure 3.55: Square Tubing Assembly

The bottom spacer plate was then fastened to the underside of the structure with three C-clamps.

Four ½" bolts were also inserted into the bolt holes to ensure proper alignment between the two plates.

The alignment arrangement is shown below in Figure 3.56. The two plates were then tack welded

together.

Figure 3.56: Attaching the Bottom Spacer

After the entire structure was assembled and the angles were verified, all of the joints were fully welded to ensure maximum strength. The fully welded structure is shown in Figure 3.57 and Figure 3.58.

Figure 3.57: Front View of Assembled Structure

Figure 3.58: Rear View of Assembled Structure

Finally, an angle grinder was used to smooth the rough edges and the welds of the structure. A file was also used to remove any burrs on the internal voids. After the fixture was cleaned, spray paint was applied to protect the steel from rust. The final painted structure is shown in Figure 3.59.
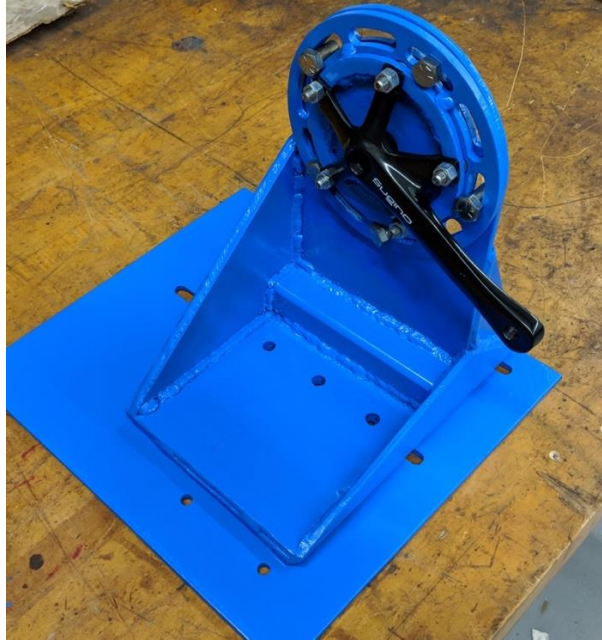
Figure 3.59: Finalized Test Structure

3.4.4.3 Fabricating the Connecting Rod Assembly

After the test structure had been completed, the fabrication of the connecting rod assembly began. Each part of the CAD assembly was saved as an IGES file, which was then imported into the post-processing software. As previously mentioned, OneCNC was used to create the necessary tool paths for each part. Low carbon steel was used for each part of this assembly. Low carbon steel is strong and highly machinable.

To create the pedal, a piece of 1-inch round stock was used. First, the outer diameter of the threaded stud was turned to 0.5 inches on the Haas SL10 turning center. Next, a threading tool was used to cut the threads (½ - 20) on the Haas TL1 lathe. Finally, Haas's VF3 vertical mill was used to create the hole. The final part is displayed in Figure 3.60.

Figure 3.60: Fabricated Pedal

Next, the connecting bracket was fabricated using the VF3 vertical mill. A ½ inch end mill was used to machine the entire part. The finalized bracket can be seen in Figure 3.61.
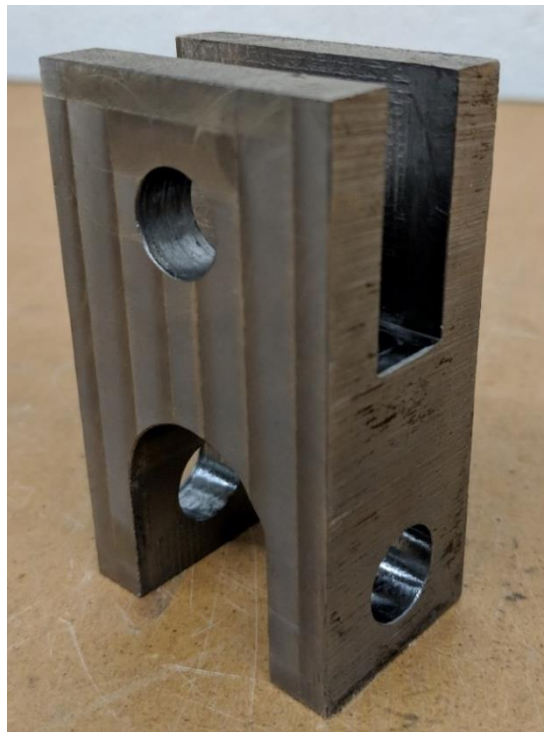
Figure 3.61: Fabricated Connecting Bracket

Finally, the connecting rod was machined with the VF3 vertical mill. A ½ inch end mill was also used to machine this part. The connecting rod can be seen in Figure 3.62.

Figure 3.62: Fabricated Connecting Rod

After the fabrication process had been completed and the parts had been deburred, the connecting rod assembly was then painted to protect the steel from rust. The finalized painted structure can be seen in Figure 3.63
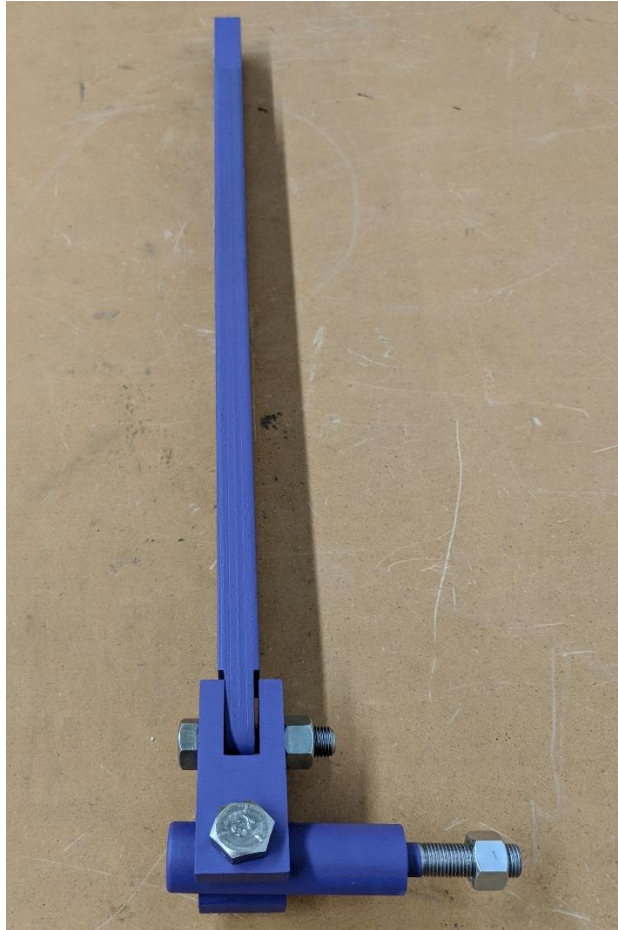
Figure 3.63: Finalized Connecting Rod Assembly

Additional images of the finalized testing apparatus can be seen in section 4.2.2 on page 116.

3.5 Test Methods

Before the testing was initiated, several set-up procedures were performed. First, two strain gauges were added to both the original stainless-steel crank arm and the DFMAM optimized crank arm to measure normal strain. Uniaxial strain gauges were used with a resistance of 120Ω and a gauge factor of 1.93. A general-purpose cold-curing glue was used to adhere the strain gauges to the surface of each crank arm. Figure 3.64 displays one of the strain gauges that was attached to the optimized crank arm.

Figure 3.64: Strain Gauge on the Optimized Crank Arm

Next, a protractor was used to mark the desired test angles on the test structure. First, a horizontal reference line was drawn across the circular crank mounting plate (see Figure 3.65). Next, a protractor was used to draw a line on the test fixture that corresponded to each test angle. This process is shown below in Figure 3.66.

Figure 3.65: Reference Line on Crank Mounting

Plate
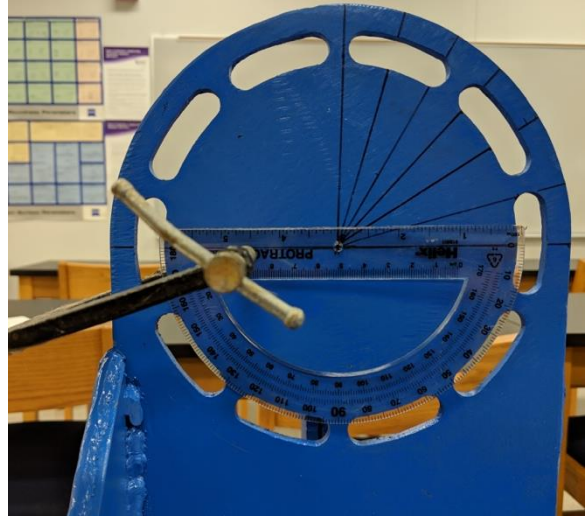
Figure 3.66: Test Angles on Test Fixture

Next, the test method was constructed within the BlueHill 3 software, which controls the Instron universal testing machine. The loading rate at which the tensile testing machine applied the force to the specimen was set to 1 mm/minute. In order to stop the test, the measurement event setting was selected underneath the end of test tab. As a result, the machine will stop applying force to the crank arm when the applied load equals the entered resultant force. The resultant force will be changed between each test so that the magnitude corresponds with the testing angle.

The test structure was then loaded into the Instron tensile tester and the crank arm was attached to the test structure. The crank mounting plate was adjusted to -89° (see Figure 3.67) and the baseplate was tweaked to align the pedal with the vertical loading axis of the tensile testing machine. Two dial indicators were added to the system to measure the deflection in both the Y and Z axes (see Figure 3.68). The strain gauge leads were connected to a P3 strain indicator and recorder, which functions as a bridge

86

amplifier, static strain indicator, and digital data logger [41]. The P3 strain indicator with the attached

leads is shown in Figure 3.69
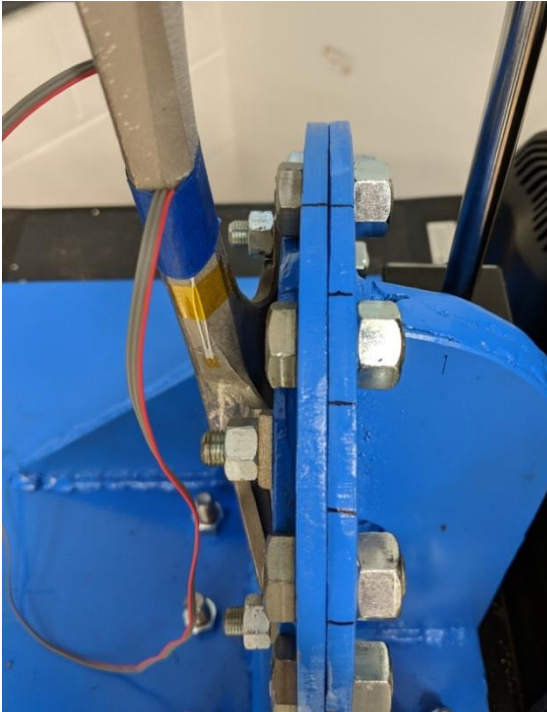
Figure 3.67: Initial Test Angle

Figure 3.68: Dial Indicator Alignment
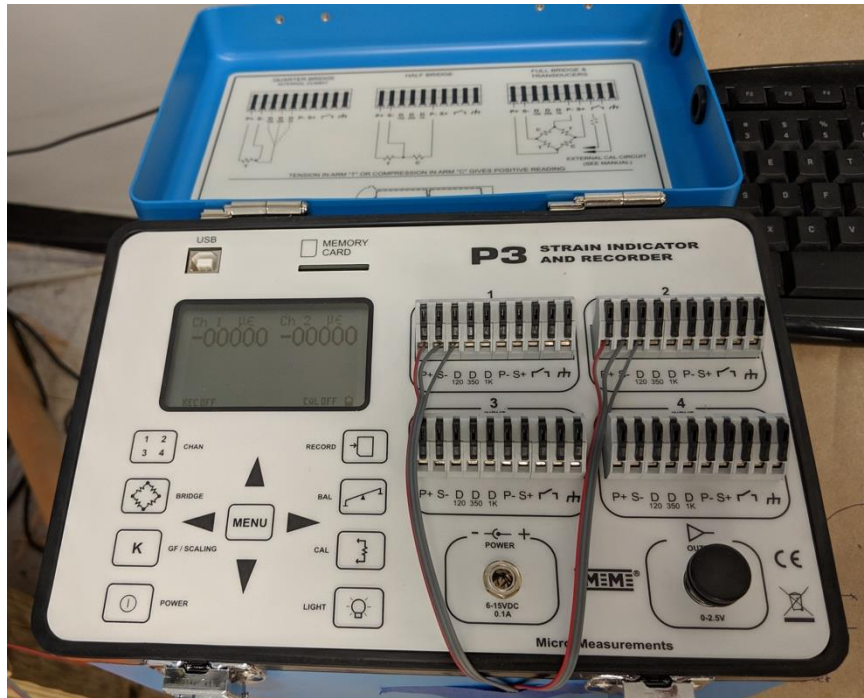
Figure 3.69: P3 Strain Indicator and Recorder

The initial test conditions are shown in Figure 3.70.
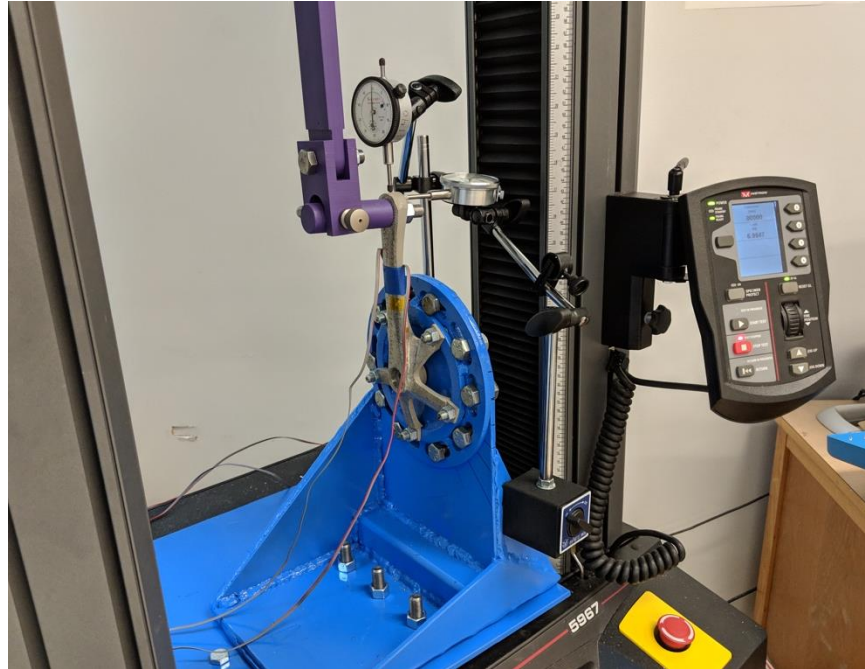
Figure 3.70: Initial Test Conditions of Original Crank Arm

After each test was performed, the following procedure was followed to ensure that the results were consistent and accurate. First, the dial indicators were removed and placed on an adjacent table. The pin that connected the cylindrical pedal to the connecting bracket was then removed. Next, the crosshead of the tensile tester was raised to enable the crank arm to rotate. The 10 crank mounting bolts were loosened or removed, which allowed the crank arm to be rotated to the next test angle. The alignment mark on the crank mounting plate was then aligned with the corresponding mark on the vertical mounting plate (see Figure 3.67 on page 87). After the alignment was verified, the 10 crank mounting bolts were then tightened to secure the two plates together. Next, the four lower bolts that attach the movable base plate to the stationary base plate were loosened. The base assembly was then shifted so that the cylindrical pedal was aligned with the vertical loading axis. The four lower bolts were then tightened to ensure that the test fixture did not move horizontally during the test. Next, the bolt that attached the pedal to the crank

89

arm was loosened so that it could be rotated. The pedal was then rotated so that the loading bolt hole aligned with the pedal mounting bracket. The pedal bolt was then tightened to secure the pedal to the crank arm. Next, the crosshead of the tensile tester was lowered into position and the pin was inserted to reattach the pedal to the mounting bracket. The fine positioning wheel located on the Instron 5967 was used to eliminate any existing pre-load. With the crank arm in position, the dial indicators were attached to the system to measure the deflection in the Y and Z axes. Both dial indicators and the P3 strain indicator were then balanced to ensure proper measurement readings. The appropriate resultant force was entered into the end load value window within the BlueHill 3 software. Next, the gauge length and the load cell of the tensile testing machine was balanced. The test was then initiated by clicking on the start button. After the maximum load was reached, the data from the two strain gauges and the measurements of the two dial indicators were recorded. After the data was recorded, the crosshead was returned to the initial gauge length, and the test files generated by the BlueHill 3 software were saved, which concluded the test. This process was repeated for each of the 12 tests on both crank arms. The loading conditions for each crank angle are shown in Table 3.3. The resultant force was applied by the Instron 5967 universal testing machine at the final crank angle.

Table 3.3: Test Conditions

Initial Angle (ϕ)	Final Angle (Θ)	Total Force (Resultant) (N)
90	63.2	157
75	48.9	195
60	38.0	227
45	27.3	275
30	15.1	333
15	1.2	410
0	-14.6	515
-15	-32.2	689
-30	-47.3	888
-45	-60.4	1017
-60	-74.1	967
-75	-89.2	766

CHAPTER 4:   RESULTS

This section displays the results of both the theoretical analyses and the experimental analyses. The results from the theoretical analysis section include the FEA results, topology optimization results, and the design verification results. The experimental results consist of the additively manufactured crank arms, the finalized testing apparatus, a weight savings analysis, and the test results.

4.1   Theoretical Results

4.1.1   Finite Element Analysis Results

The following section displays the results of the FEA performed on the original stainless-steel crank arm. Figure 4.1 displays the equivalent (von-Mises) stresses that occurred at the optimization angle of -60.4°. Figure 4.2 presents a closer view of where the greatest stresses occurred at the optimization angle. Figure 4.3 shows the magnitude of equivalent deflection that occurred at the optimization angle, and Figure 4.4 displays the maximum amount of deflection that the crank arm experienced, which occurred at -74.1°.
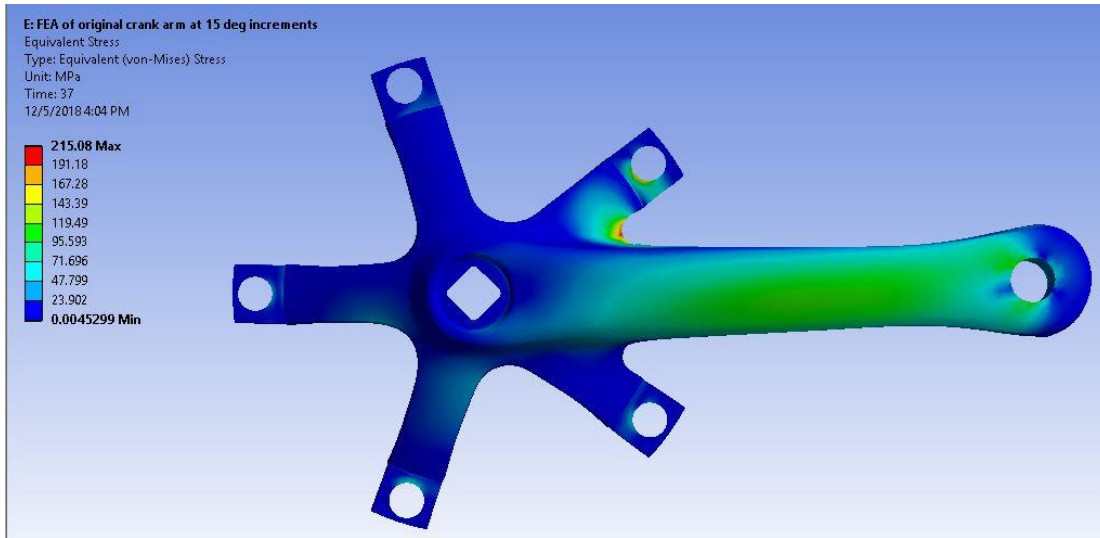
Figure 4.1: Original Crank Arm: Maximum Stress that Occurred at the Optimization Angle (-60.4°)
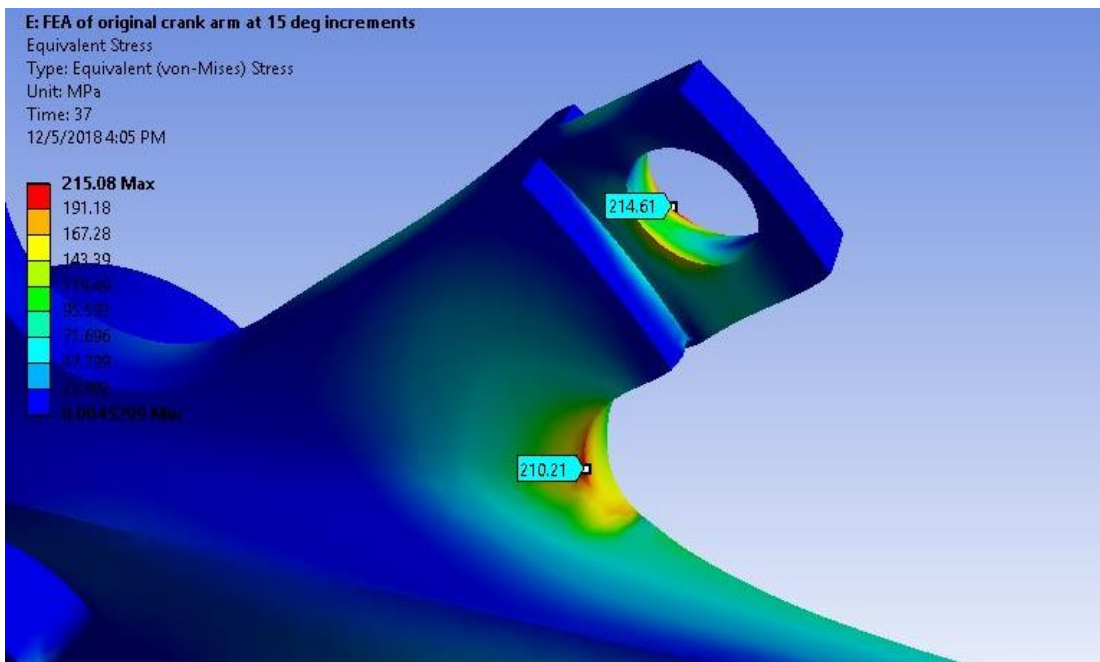
Figure 4.2: Original Crank Arm: Stresses on Spider leg #1 at Optimization Angle (-60.4°)
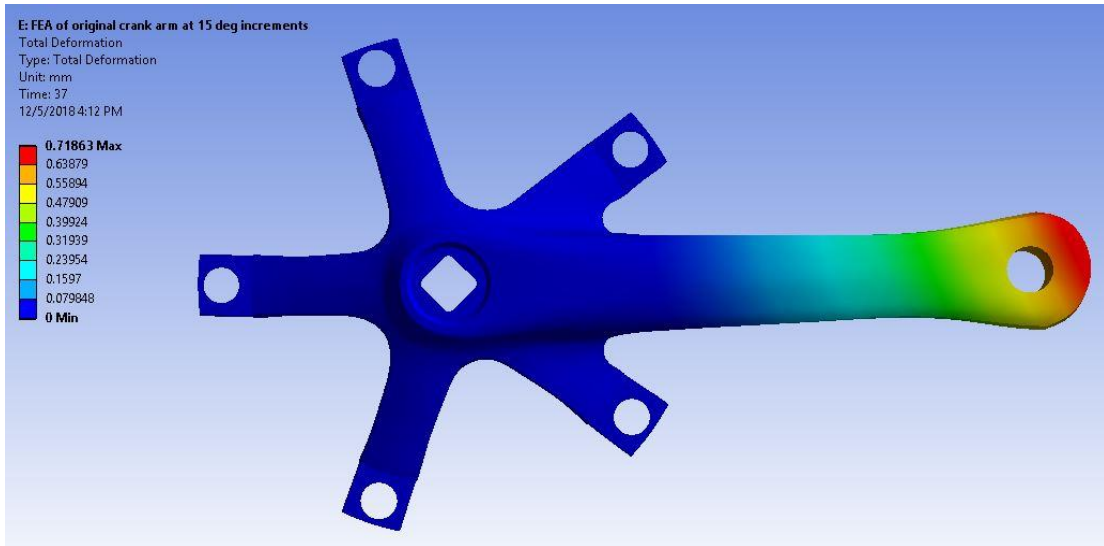
Figure 4.3: Original Crank Arm: Deformation at the Optimization Angle (-60.4°)
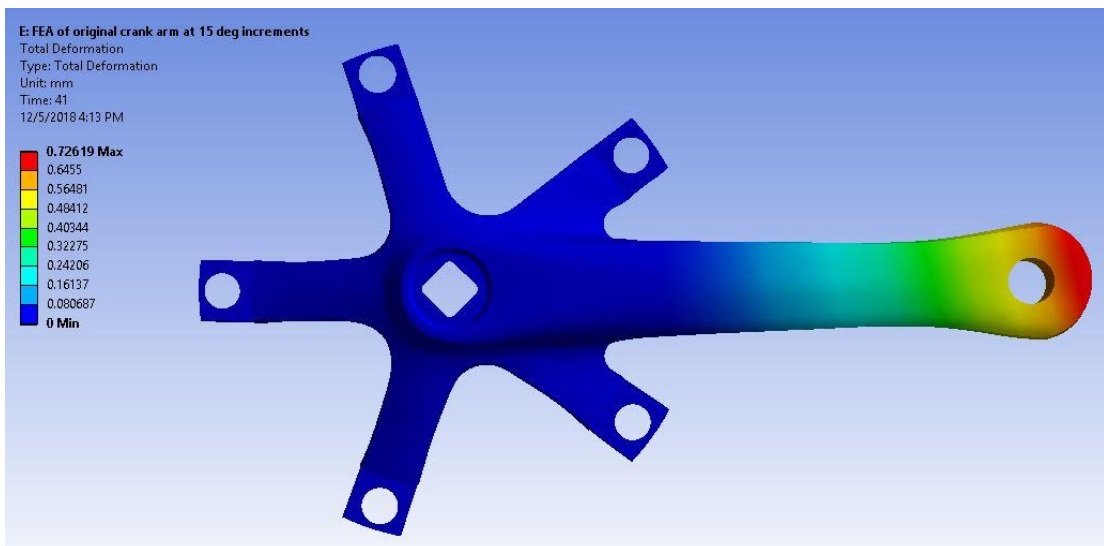
Figure 4.4: Original Crank Arm: Maximum Deflection Occurred at -74.1° (Load Step 41)

4.1.2 Topology Optimization Results

The results from the topology optimization study are displayed below in the following figures. The optimization study determined that the geometry of spider leg #2 was not critical to the part's performance. Therefore, the study removed the surrounding geometry with the exception of the previously defined exclusion regions. Also, as previously shown in Figure 3.19 on page 48, the study determined that the internal geometry of the arm was extraneous and was therefore removed. Material from each spider was also removed to reduce the overall weight of the crank arm.
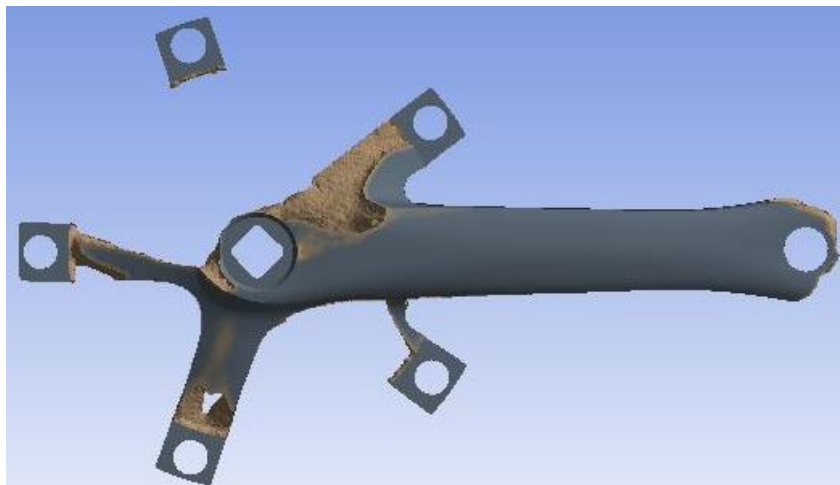
Figure 4.5: Front View of Optimized Crank Arm
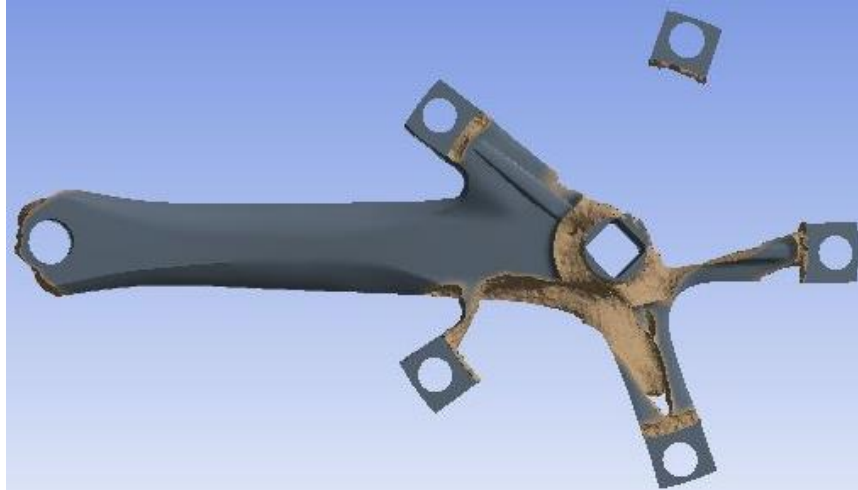
Figure 4.6: Back View of Optimized Crank Arm
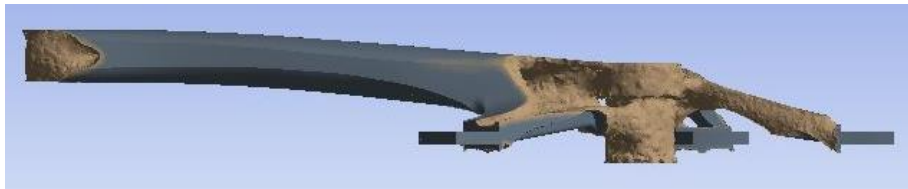
Figure 4.7: Side View of Optimized Crank Arm

4.1.3 Design Verification Results

The following section displays the design verification results of both the original optimized crank arm and the DFMAM optimized crank arm.

4.1.3.1 Original Optimized Crank Arm

Figure 4.8 displays the stresses within the part at -89 degrees (load step = 45), which is the angle where the maximum stress occurred. Figure 4.9 shows the stresses within the part that occur at the optimization angle (-60.4°), and Figure 4.10 displays where the maximum stress occurs at the

optimization angle. Figure 4.11 exhibits the maximum deflection that the crank arm experienced, which

occurred at -74.1°. Figure 4.12 displays the deflection that occurred at the optimization angle (-60.4°).
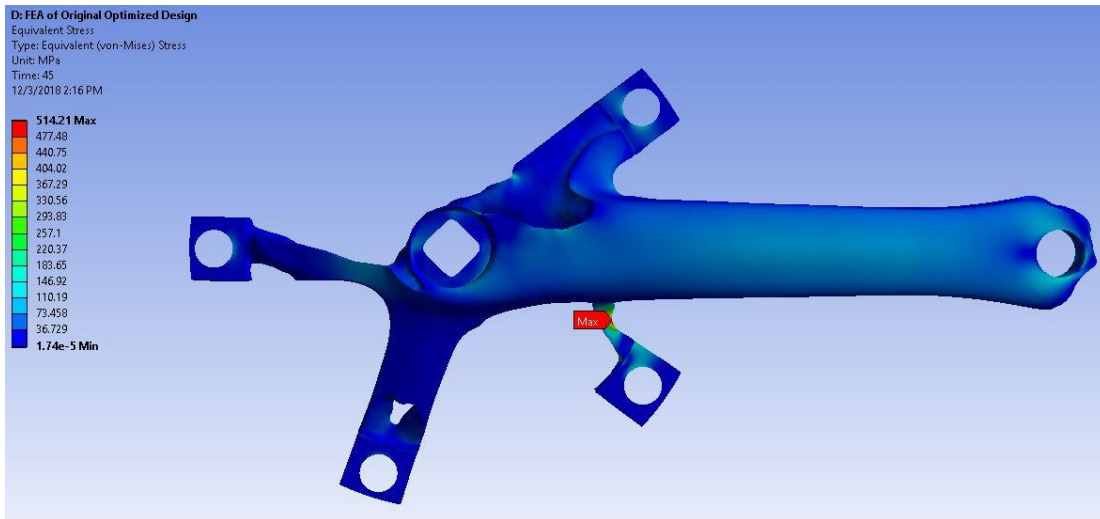
Figure 4.8: Original Optimized Crank Arm: Maximum stress occurred at -89° (Load Step 45)
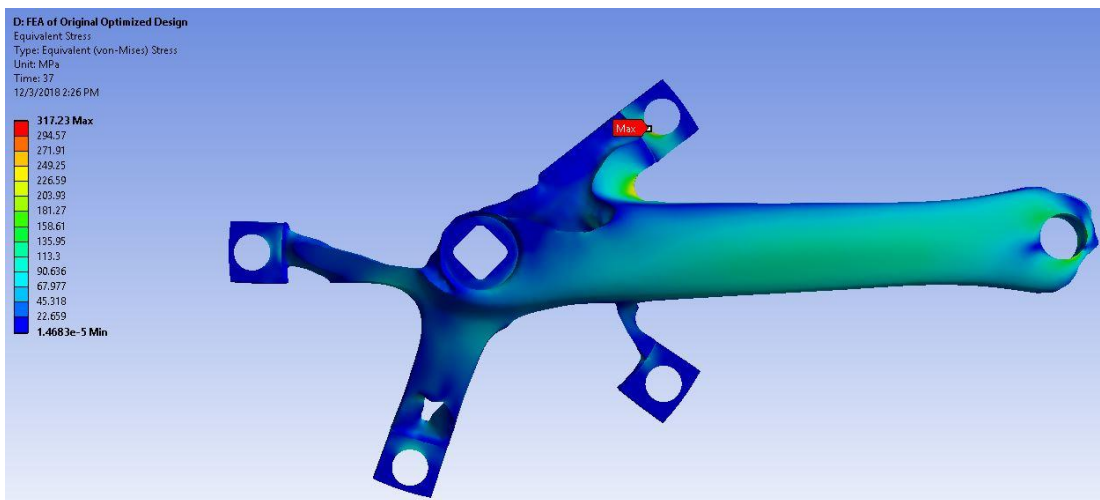
Figure 4.9: Original Optimized Crank Arm: Stresses at Optimization Angle (-60.4 deg)
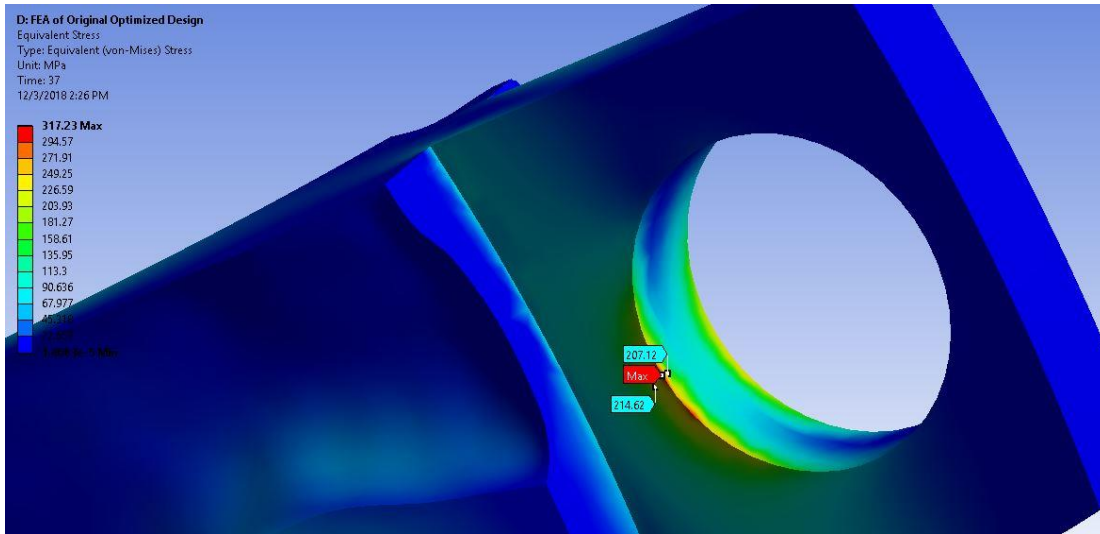
Figure 4.10: Original Optimized Crank Arm: Stresses on Spider #1 at Optimization Angle (-60.4 deg)
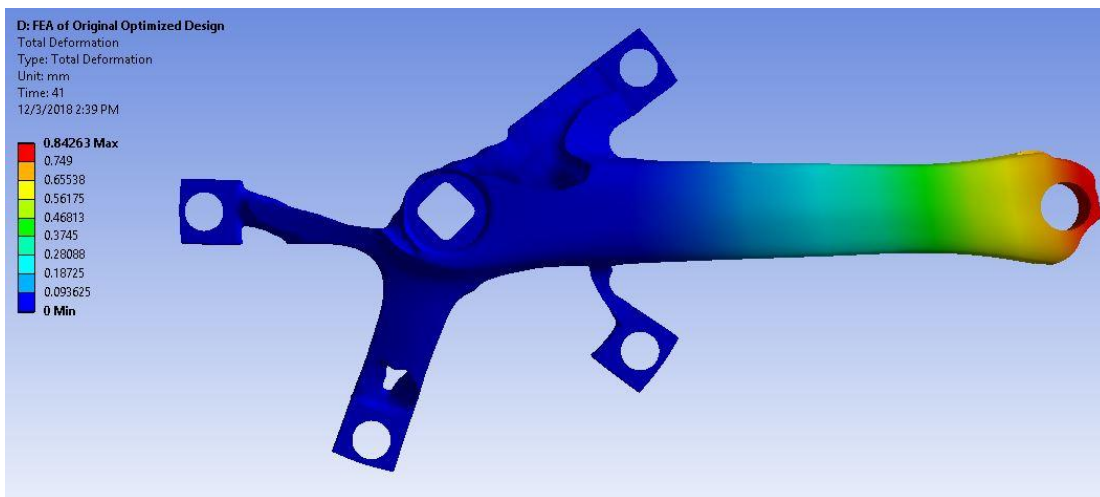
Figure 4.11: Original Optimized Crank Arm: Maximum Deflection at Occurred at -74.1°
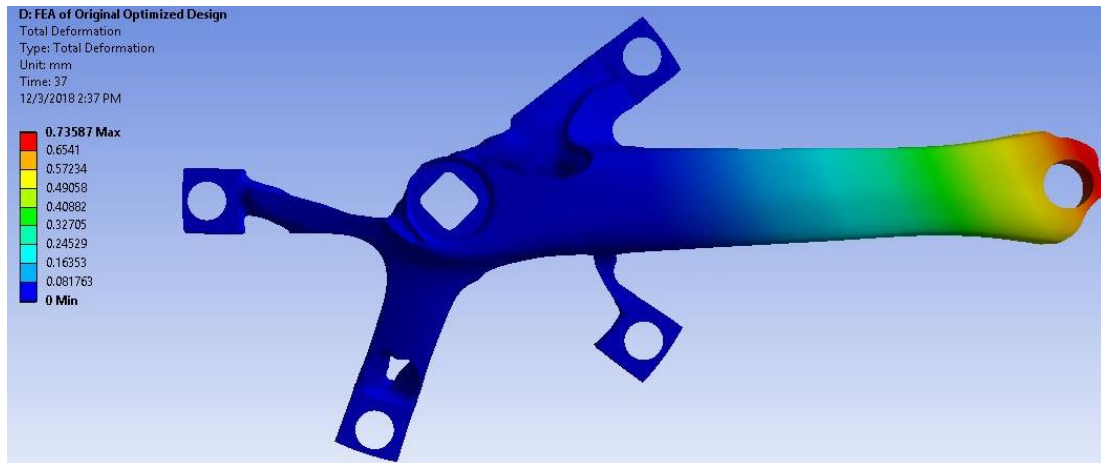
Figure 4.12: Original Optimized Crank Arm: Deflection at Optimization Angle (-60.4°)

4.1.3.2 DFMAM Optimized Crank Arm

The top view of the final DFMAM optimized geometry is displayed in Figure 4.9, and the back view is shown in Figure 4.14. Figure 4.15 displays the stresses within the part at -14.6 degrees (load step # 25), which is the angle where the maximum stress occurred. Figure 4.16 reveals where the stress is most concentrated at the same angle of -14.6°. Figure 4.17 shows the stresses within the part that occur at the optimization angle (-60.4°), and Figure 4.18 displays where the maximum stress occurs at the optimization angle. Figure 4.19 exhibits the maximum deflection that the crank arm experienced, which occurred at -74.1°. Figure 4.20 displays the deflection that occurred at the optimization angle (-60.4°).

99

Figure 4.13: Top View of Finalized DFMAM Geometry

Figure 4.14: Back View of Finalized DFMAM Geometry
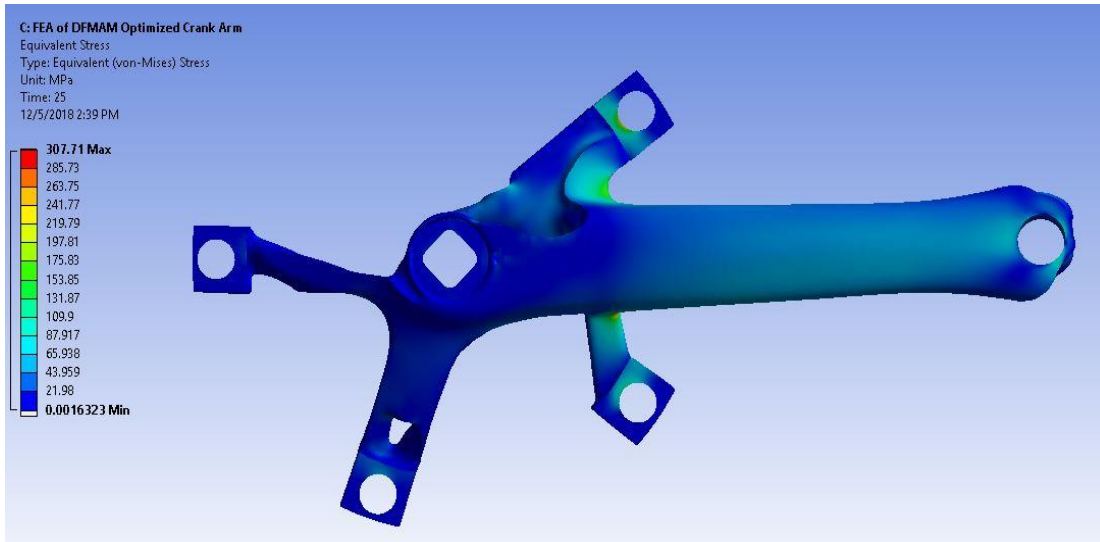
Figure 4.15: DFMAM Optimized Crank Arm: Maximum Stress Occurred at -14.6° (Load Step 25)
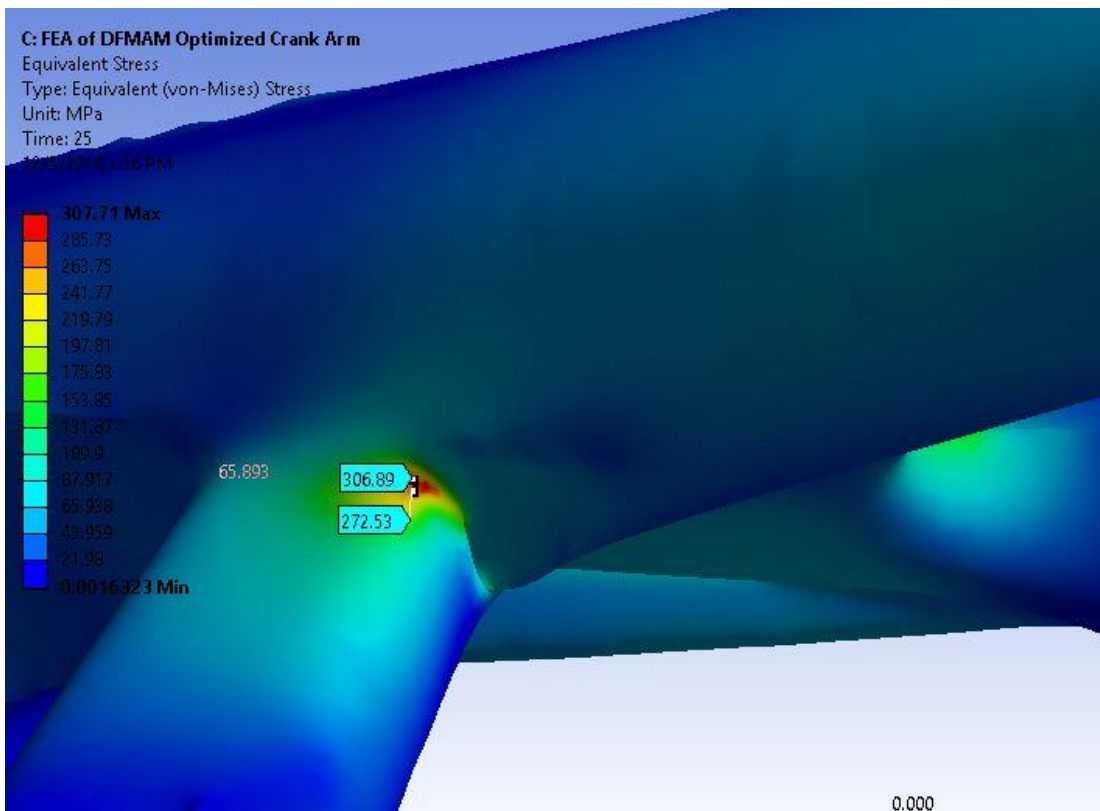
Figure 4.16: DFMAM Optimized Crank Arm: Maximum Stress on Spider leg #5 at -14.6°

101
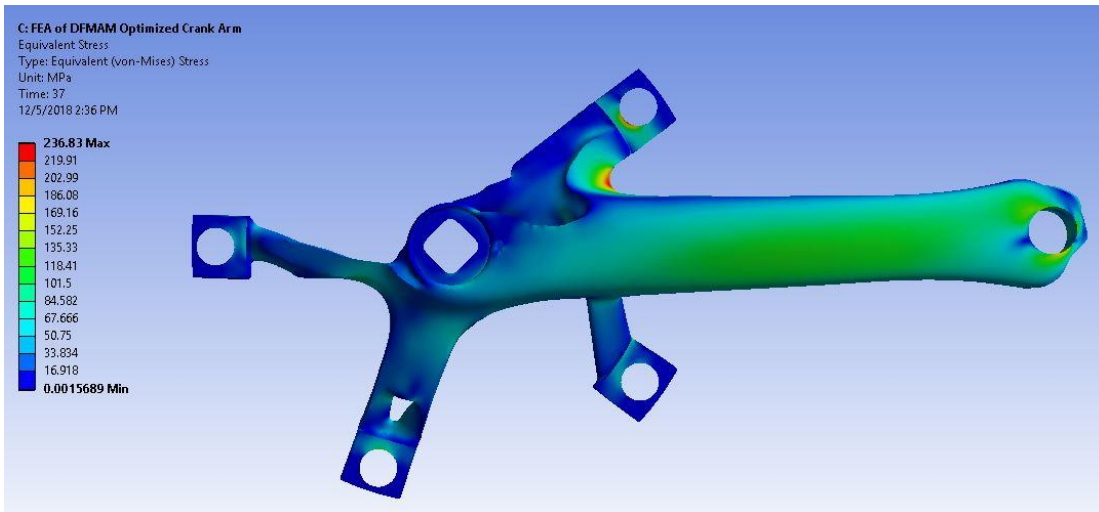
Figure 4.17: DFMAM Optimized Crank Arm: Stresses at Optimization angle (-60.4°)
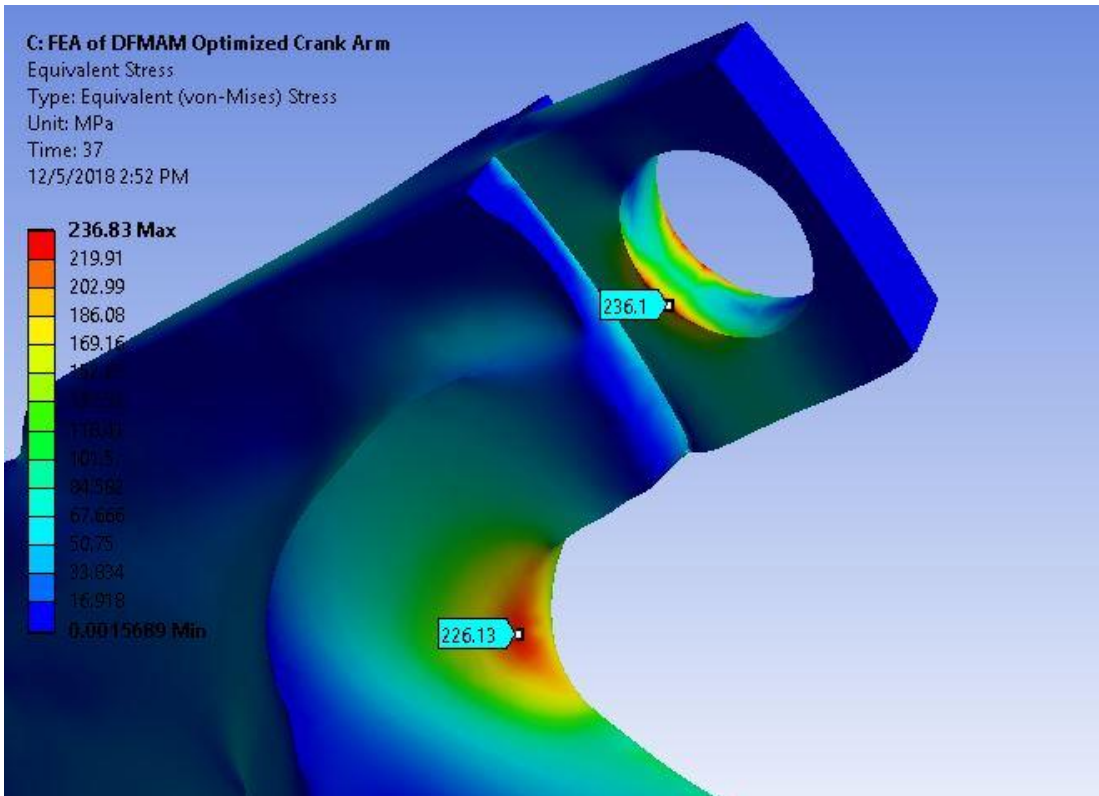
Figure 4.18: DFMAM Optimized Crank Arm: Maximum Stresses at Optimization Angle (-60.4°)
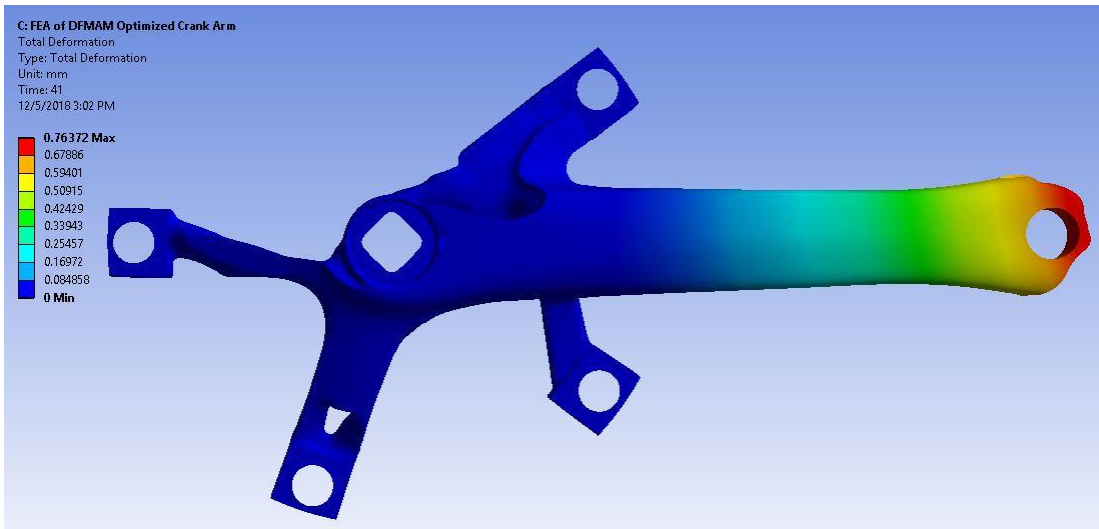
Figure 4.19: DFMAM Optimized Crank Arm: Maximum Deformation occurred at -74.1°
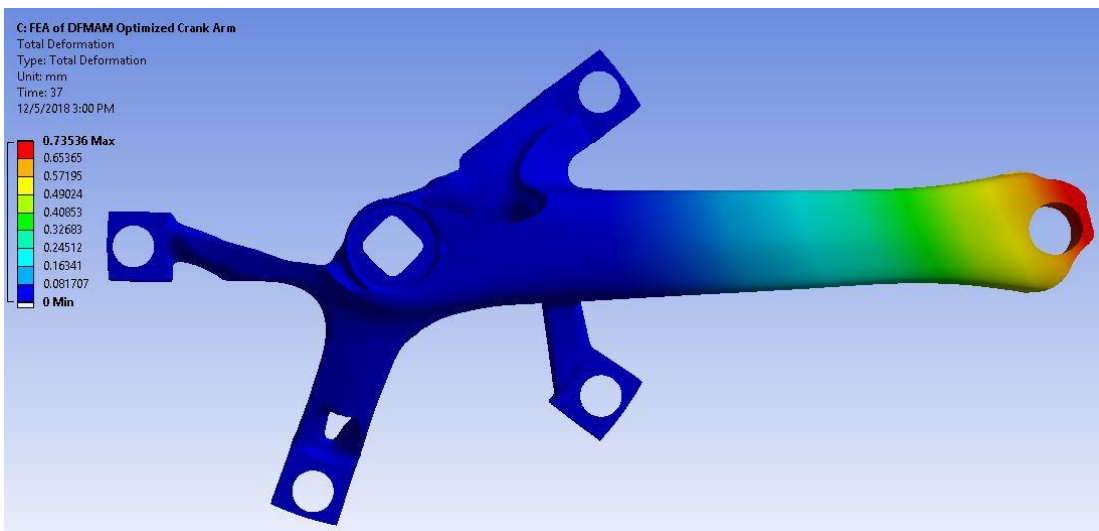
Figure 4.20: DFMAM Optimized Crank Arm: Deformation at Optimization Angle (-60.4°)

4.1.3.3 Theoretical Comparison

The following graphs compare the theoretical results of the original printed crank arm, the initial optimized design, and the DFMAM optimized design. Figure 4.21 displays the maximum stress vs crank angle, Figure 4.22 shows average stress vs crank angle, Figure 4.23 presents the maximum deflection vs crank angle, and Figure 4.24 displays the average deflection vs crank angle. In each of the following graphs, the blue line represents the original design, the orange line represents the optimized design, and the gray line represents the DFMAM optimized design.
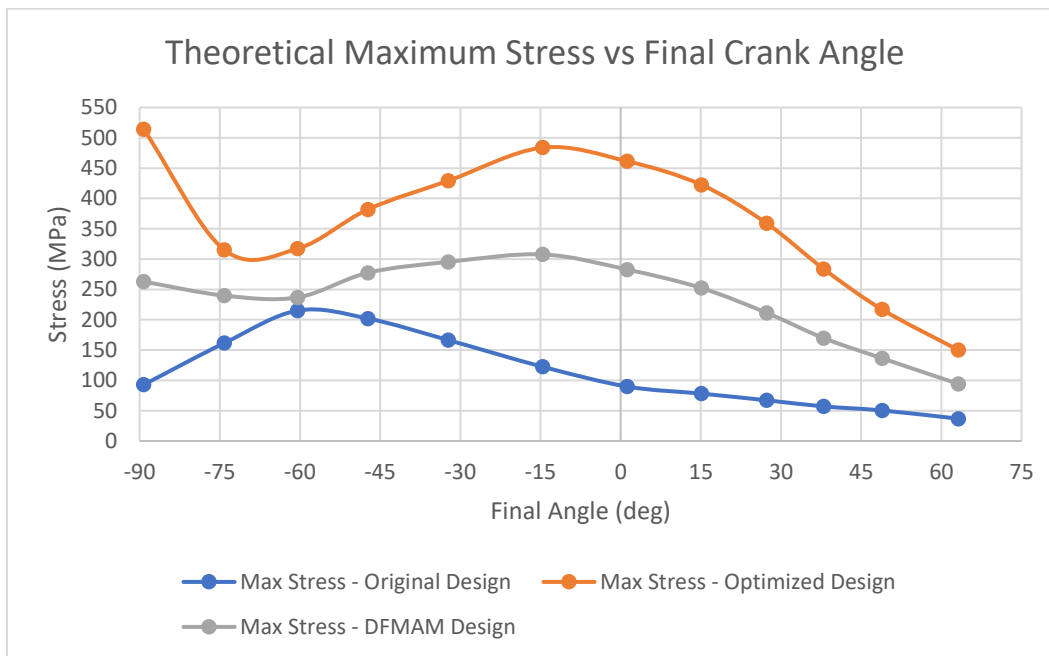
Figure 4.21: Theoretical Maximum Stress vs Final Crank Angle
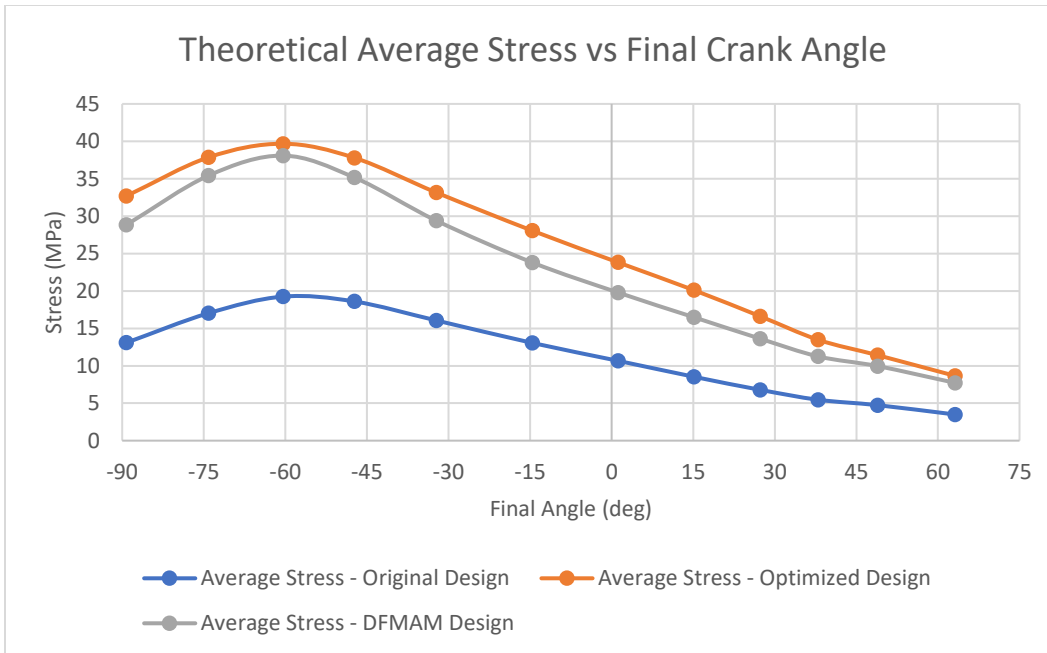
Figure 4.22: Theoretical Average Stress vs Final Crank Angle
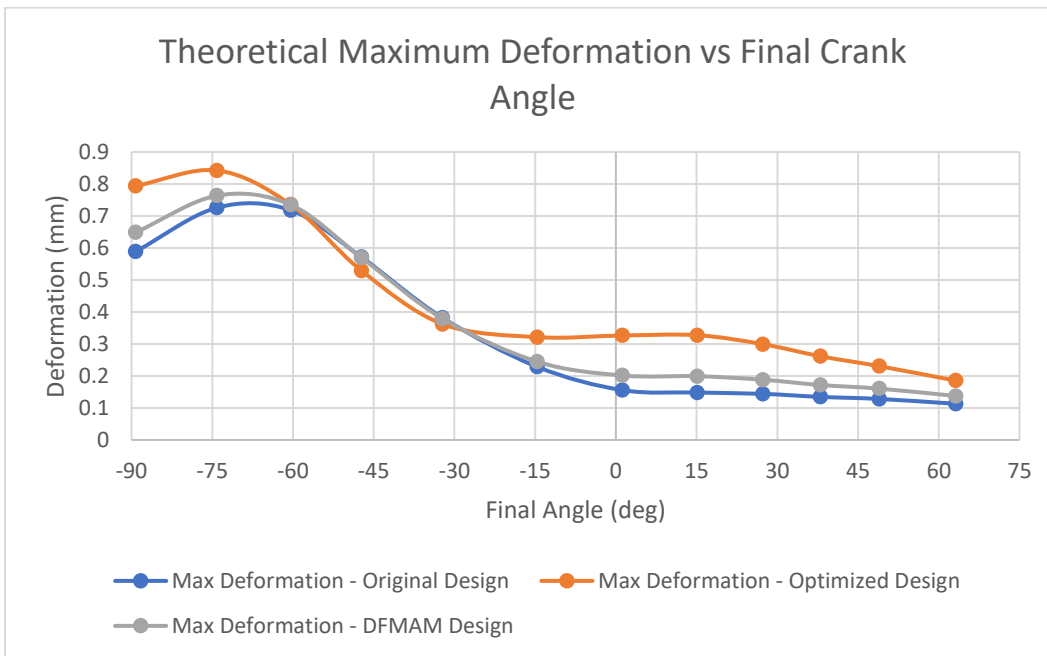
Figure 4.23: Theoretical Maximum Deflection vs Final Crank Angle
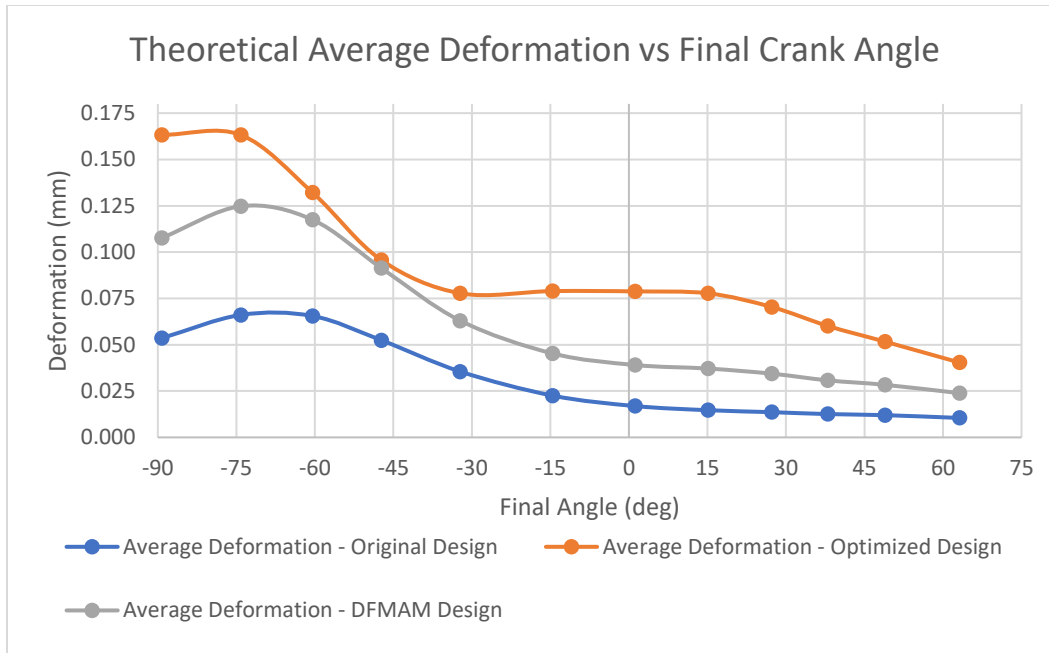
Figure 4.24: Theoretical Average Deflection vs Final Crank Angle

The following two figures compare the differences in both von-Mises stress and total deformation between the DFMAM optimized crank arm and the original crank arm as a percentage. Figure 4.25 compares the differences in von-Mises stress between the DFMAM optimized crank arm and the original crank arm, and Figure 4.26 presents the differences in total deformation between the DFMAM optimized crank arm and the original crank arm.
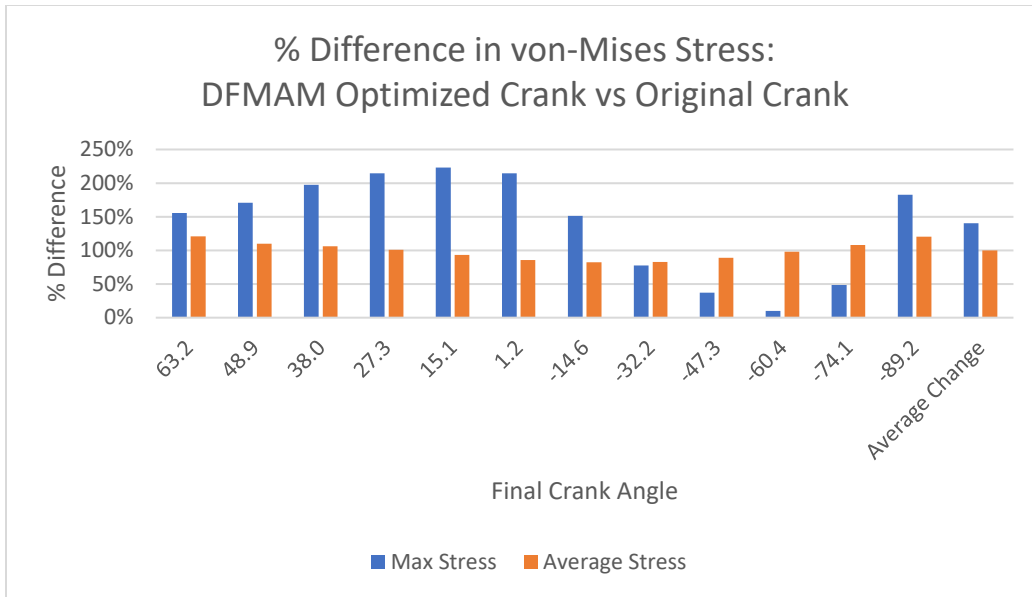
Figure 4.25: Percent Difference in von-Mises Stress: DFMAM Optimized Crank vs Original Crank
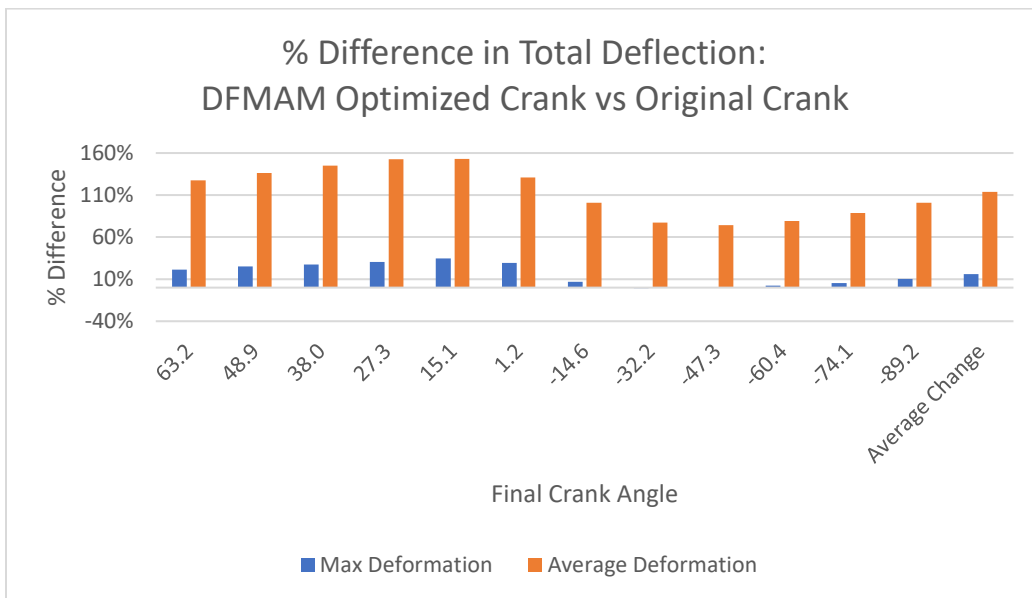
Figure 4.26: Percent Difference in Total Deformation: DFMAM Optimized Crank vs Original Crank

The following tables display the maximum overall value of the maximum stress, maximum average stress, maximum deformation, maximum average deformation, maximum strain, maximum average strain, and at which initial angle, final angle, and the load step these maximums occur.

Table 4.1 displays the results from the original stainless-steel design, Table 4.2 shows the results from the original optimized design, and Table 4.3 presents the results from the DFMAM optimized design.

Table 4.1: Results of Original Stainless-Steel Crank Arm

Original Design				
	Max Value	Initial Angle (deg)	Final Angle (deg)	Load Step #
Greatest Value of Maximum Stress (MPa)	206.31	-45	-60.439	37
Greatest Value of Average Stress (MPa)	19.249	-45	-60.439	37
Greatest Value of Maximum Deformation (mm)	0.72597	-60	-74.147	41
Greatest Value of Average Deformation (mm)	0.066095	-60	-74.147	41
Greatest Value of Maximum Strain (mm/mm)	0.0010711	-45	-60.439	37
Greatest Value of Average Strain (mm/mm)	0.00010175	-45	-60.439	37

Table 4.2: Results of Original Optimized Crank Arm

Initial Optimized Design				
	Max Value	Initial Angle (deg)	Final Angle (deg)	Load Step #
Greatest Value of Maximum Stress (MPa)	514.21	-75	-89.229	45
Greatest Value of Average Stress (MPa)	39.676	-45	-60.439	37
Greatest Value of Maximum Deformation (mm)	0.84263	-60	-74.147	41
Greatest Value of Average Deformation (mm)	1.63E-01	-75	-89.229	45
Greatest Value of Maximum Strain (mm/mm)	2.66E-03	-75	-89.229	45
Greatest Value of Average Strain (mm/mm)	2.06E-04	-45	-60.439	37

Table 4.3: Results of DFMAM Optimized Steel Crank Arm

DFMAM Optimized Design				
	Max Value	Initial Angle (deg)	Final Angle (deg)	Load Step #
Greatest Value of Maximum Stress (MPa)	307.71	0	-14.604	25
Greatest Value of Average Stress (MPa)	38.09	-45	-60.439	37
Greatest Value of Maximum Deformation (mm)	0.76372	-60	-74.147	41
Greatest Value of Average Deformation (mm)	1.25E-01	-60	-74.147	41
Greatest Value of Maximum Strain (mm/mm)	1.60E-03	0	-14.604	25
Greatest Value of Average Strain (mm/mm)	1.98E-04	-45	-60.439	37

4.2 Experimental Results

4.2.1 Fabricated Crank Arms

This section displays both crank arms as they were removed from the EOS M 290 metal additive manufacturing machine. As previously mentioned, the first printing operation was designed to print both the original crank arm and the DFMAM optimized crank arm. However, the original crank arm failed during the initial printing operation. Therefore, a second printing operation was needed to fabricate the original crank arm. This section also discusses the support removal process for both crank arms. Finally, this section analyzes the weight saved by the topology optimization process.

4.2.1.1 DFMAM Optimized Design

During the first printing operation, the recoater blade of the M 290 crashed into several support structures on the original crank arm. This contact bent and deformed multiple support structures. Therefore, the printing of the original crank arm was aborted. Figure 4.27 displays the resulting build plate.
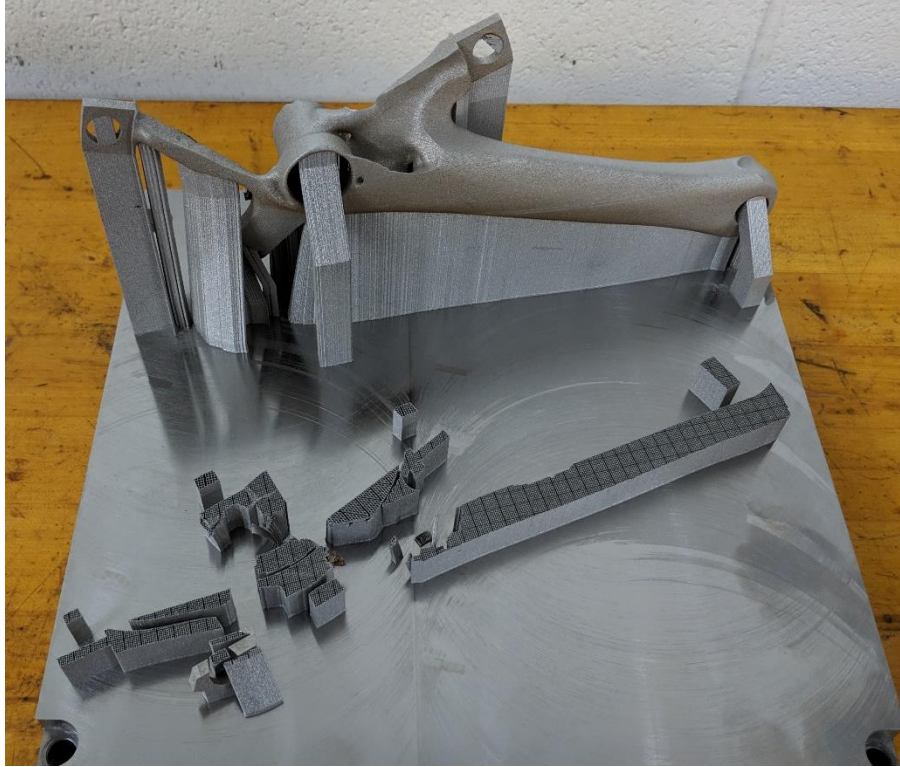
Figure 4.27: Resulting Print #1

Figure 4.28 displays the where the recoater blade contacted the support structures of the original

crank arm. Several thin structures were bent, and several additional structures were badly damaged (see

the red circles in Figure 4.28). Also, the thin structure created in section 3.3.3 (Figure 3.27) was damaged

by the recoater blade (see Figure 4.29). However, it was determined that this damaged structure would not

significantly affect the test results.
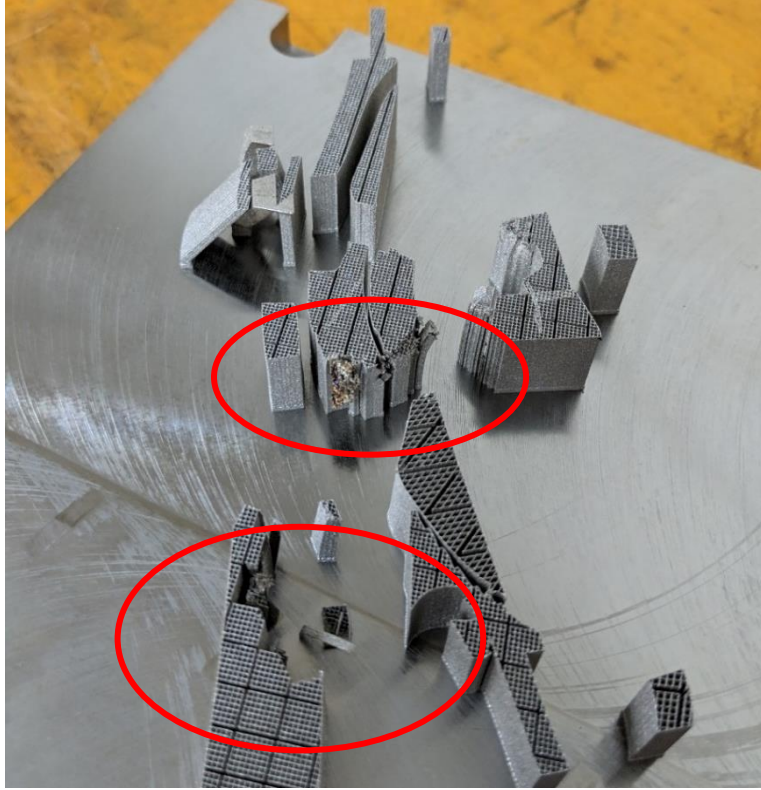
Figure 4.28: Failed Print of the Original Crank Arm
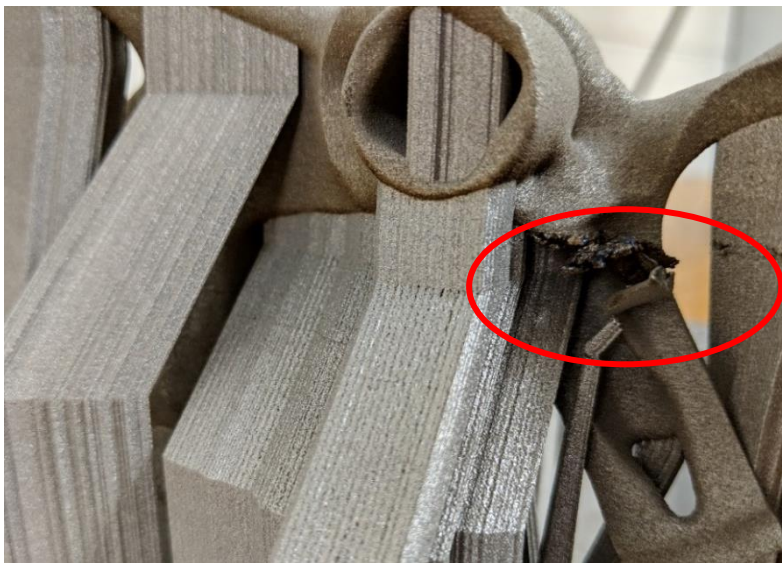
Figure 4.29: Damaged Structure on the DFMAM Optimized Crank Arm

Before the support material could be removed from the DFMAM optimized crank arm, the structure was removed from the build plate by using a horizontal band saw. After the part was removed from the build plate, the support structures were removed by using pliers and a Dremel tool. The thin support structures could be removed from the part using a pair of pliers and the Dremel tool with a cutting wheel was used to weaken the thicker support structures. Finally, the remaining support structures were removed by using the Dremel tool with a grinding wheel.

4.2.1.2 Original Design

A separate printing operation was needed to print a replica of the original crank arm. The resulting part is shown below in Figure 4.30.
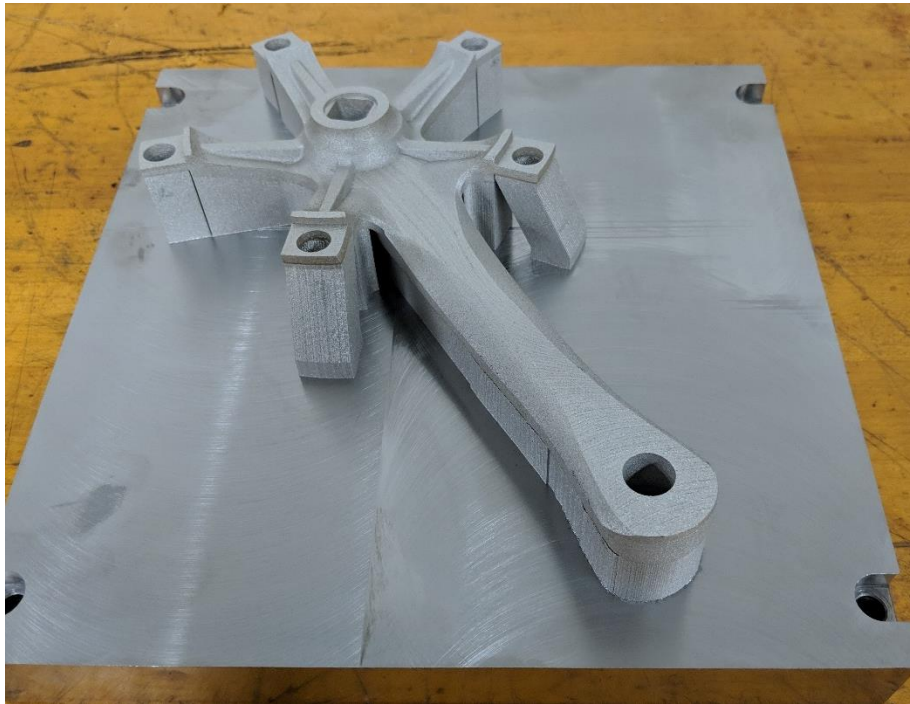
Figure 4.30: Resulting Print #2

After the build plate was removed from the M 290, the structure was removed from the build plate by using a band saw. Next, the support structures were removed from the crank arm by using a hammer. The original crank arm without support material can be seen in Figure 4.31.

Figure 4.31: Original Crank Arm without Support Material

The removal of the support material revealed a course surface finish. Therefore, an angle grinder was used to smooth the surface of the crank arm. The resulting part is shown below in Figure 4.32. The remaining support material surrounding the axle hole geometry was removed by using a Dremel tool with a grinding bit.

Figure 4.32: Finalized Original Crank Arm

The two finalized crank arms are displayed in Figure 4.33 and Figure 4.34.

Figure 4.33: Top View of both Metal Printed

Crank Arms

Figure 4.34: Top View of both Metal Printed

Crank Arms

115

4.2.2 Finalized Testing Apparatus

Figure 4.35 and Figure 4.36 display both the front and back view of the finalized test structure, and Figure 4.37 presents the finalized pedal assembly. Figure 4.38 and Figure 4.39 demonstrate how both the test structure and the pedal assembly were to be mounted to the Instron 5967 tensile testing machine.
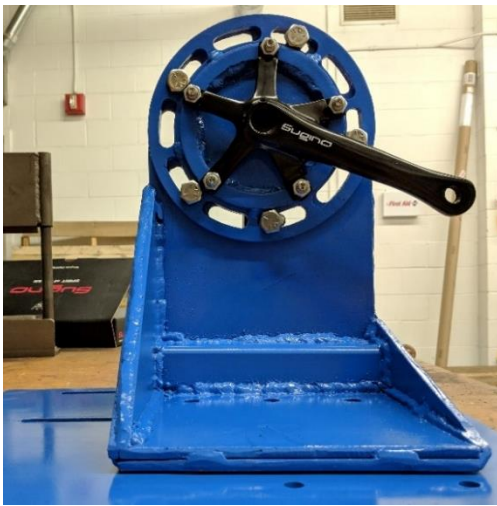
Figure 4.35: Front View of Testing Structure

Figure 4.36: Back View of Testing Structure

Figure 4.37: Finalized Pedal Assembly
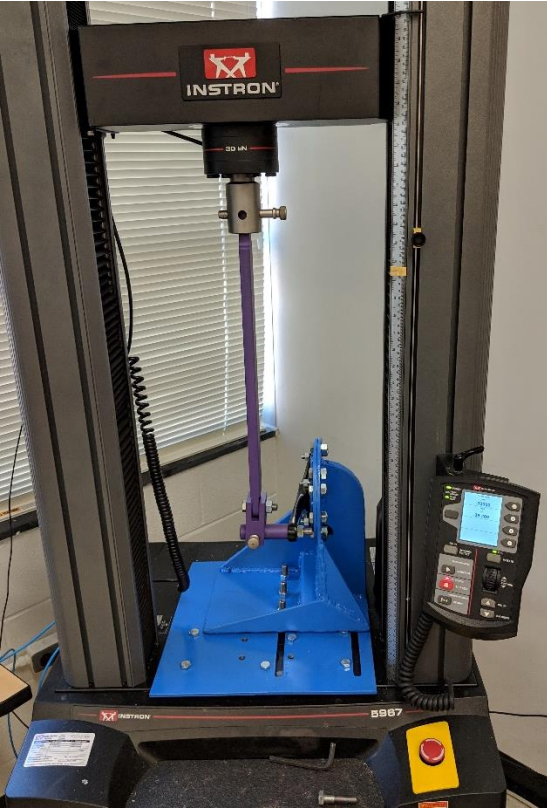
Figure 4.38: Front View of Testing Apparatus

Mounted in the Instron Tensile Tester

Figure 4.39: Side View of Testing Apparatus

Mounted in the Instron Tensile Tester

4.2.3   Weight Analysis

This section discusses the how the topology optimization study affected the weight of the

finalized crank arm. First, the theoretical weight of the original stainless-steel crank arm was determined

by obtaining the part's volume from the CAD model. The weight was then be calculated by multiplying

the volume times the density of the material. The density of the 316L stainless-steel, which was obtained

from the EOS 316L stainless-steel material data sheet, is 9.7 $g/_{cm^3}$ [42]. Equation 4.1 was used to calculate

the theoretical weight of the crank arm in kilograms.

$$W \ (kg) = \rho \ \left(\frac{g}{cm^3}\right) * volume \ (mm^3) * \left(\frac{1 \ cm^3}{1000 \ mm^3}\right)\left(\frac{1 \ kg}{1000 \ g}\right) \tag{4.1}$$

Equation 4.1 was used to calculate the weight of the original printed crank arm, initial optimized design, and the DFMAM optimized design. The weight of each crank arm was then compared to the original printed crank arm to determine the theoretical amount of weight savings. These results can be seen in Table 4.4.

After the crank arms were fabricated and the support material was removed, the original aluminum crank arm, the original stainless-steel crank arm, and the DFMAM optimized crank arm were weighed to determine their actual weight in kilograms. The actual weight was then compared to the theoretical weight to determine accuracy of the previous weight savings calculation. Finally, the actual volume was calculated by solving the previous equation for the volume.

Table 4.4 displays results of the weight analysis. The DFMAM optimized crank arm weighs 0.359 kg (359 g) less than the original stainless-steel crank arm, which is a 41.8% weight savings.

Table 4.4: Weight Analysis

	Theoretical Results			Experimental Results				
Weight Analysis	Volume (mm^3)	Calculated Weight (kg)	Weight Savings Compared to Original Printed Crank Arm (%)	Measured Weight (kg)	% Difference Between Theoretical Weight and Actual Weight	Weight Savings Compared to Original Printed Crank Arm (%)	Density (g/cm^3)	Calculated Volume (mm^3)
Original Aluminum Crank Arm				0.2909			2.7	107740.7407
Original Printed Crank Arm	109110	0.861969	0.0%	0.8591	-0.33%	0.0%	7.9	108746.8354
Initial Optimized Design	60429	0.4773891	-44.6%					
DFMAM Optimized Design	63836	0.5043044	-41.5%	0.5001	-0.83%	-41.8%	7.9	63303.79747

4.2.4   Test Results

Table 4.5 and Table 4.6 shown below display the results of the physical testing of the crank arms. The resulting two tables are divided into four categories. The first category displays the input data for each test, which consists of the initial angle, the final angle, and the resultant force. The second category presents the measured normal microstrain at strain gauge #1 and strain gauge #2. The third category shows the measured deflection in both the Y and Z axes relative to the tensile tester. The deflection was originally measured in inches but was converted into mm with the conversion formula shown in equation 4.2.

$$Deflection\ (mm) = \frac{25.4\ mm}{1\ in} * Deflection\ (in) \qquad (4.2)$$

Finally, the fourth category displays the calculated normal strain that occurred at strain gauge #1 and strain gauge #2. Stress can be derived from strain by multiplying the modulus of elasticity times the

measured strain value, which is shown in equation 4.3 [43]. According to the material data sheet within

ANSYS Mechanical, the modulus of elasticity for stainless-steel is 193000 MPa. Because the strain was

measured in microstrain, the conversion equation was multiplied by 10^{-6} to convert the microstrain into

strain.

$$\sigma = E\varepsilon \quad \rightarrow \quad \sigma = \frac{193000\ N}{mm^2} * (\varepsilon * 10^{-6}) \tag{4.3}$$

Table 4.5 displays the test results of original stainless-steel crank arm, and Table 4.6

presents the test results of the DFMAM optimized crank arm.

Table 4.5: Original Stainless-Steel Test Results

Original Stainless-Steel Crank Arm Test Results									
	Input Data			Measured Strain		Measured Deflection		Stress Calculations	
Number	Initial Angle (ϕ)	Final Angle (θ)	Total Force (Resultant) (N)	Gauge #1 ($\mu\varepsilon$)	Gauge #2 ($\mu\varepsilon$)	Z Deflection (mm)	Y Deflection (mm)	Stress at gauge #1 (MPa)	Stress at gauge #2 (MPa)
1	90	63.2	157	-32	29	0.038	N/A	-6.18	5.60
2	75	48.9	195	-53	52	0.051	0.076	-10.23	10.04
3	60	38.0	227	-71	71	0.038	0.025	-13.70	13.70
4	45	27.3	275	-100	101	0.064	0.025	-19.30	19.49
5	30	15.1	333	-128	132	0.089	0.000	-24.70	25.48
6	15	1.2	410	-157	165	0.127	0.102	-30.30	31.85
7	0	-14.6	515	-190	203	0.140	0.216	-36.67	39.18
8	-15	-32.2	689	-221	242	0.178	0.483	-42.65	46.71
9	-30	-47.3	888	-229	256	0.089	0.559	-44.20	49.41
10	-45	-60.4	1017	-167	297	0.076	0.711	-32.23	57.32
11	-60	-74.1	967	-80	107	0.025	0.686	-15.44	20.65
12	-75	-89.2	766	14	4	0.000	0.584	2.70	0.77

Table 4.6: DFMAM Optimized Test Results

DFMAM Optimized Crank Arm Test Results								
	Input Data			Measured Strain		Measured Deflection		Stress Calculations	
Test Number	Initial Angle (ϕ)	Final Angle (Θ)	Total Force (Resultant) (N)	Gauge #1 ($\mu\epsilon$)	Gauge #2 ($\mu\epsilon$)	Z Deflection (mm)	Y Deflection (mm)	Stress at gauge #1 (MPa)	Stress at gauge #2 (MPa)
1	90	63.2	157	-37	27	0.064	N/A	-7.14	5.21
2	75	48.9	195	-56	49	0.070	0.076	-10.81	9.46
3	60	38.0	227	-77	74	0.095	0.051	-14.86	14.28
4	45	27.3	275	-101	104	0.102	0.025	-19.49	20.07
5	30	15.1	333	-123	138	0.191	0.013	-23.74	26.63
6	15	1.2	410	-155	181	0.305	0.229	-29.92	34.93
7	0	-14.6	515	-171	220	0.216	0.229	-33.00	42.46
8	-15	-32.2	689	-180	259	0.241	0.483	-34.74	49.99
9	-30	-47.3	888	-176	289	0.191	7.366	-33.97	55.78
10	-45	-60.4	1017	-125	260	0.064	0.889	-24.13	50.18
11	-60	-74.1	967	-18	144	0.089	1.029	-3.47	27.79
12	-75	-89.2	766	60	30	0.102	0.826	11.58	5.79

The physical test results were then compared to the FEA results to determine if the FEA model accurately depicted the physical behavior of the crank arms. Within the ANSYS Mechanical software, two probes were placed in the same locations as the strain gauges to create numerical data that is comparable to the test results. The probes displayed both the normal strain and the normal stress for each test angle under consideration. The following four tables compare the test results against the FEA results and display the difference as a percentage.

First, the measured strain data was compared to the FEA strain data. As previously mentioned, two probes were placed on the crank arm to display the numerical strain values where the strain gauges were attached to the crank arm. Figure 4.40 shows the two probes that displayed the normal strain that occurred within the original crank arm at 27.3°, and Figure 4.41 displays the FEA results of the normal strain that occurred within the original crank arm at -60.4°. This process was repeated for all 12 crank angles under consideration.

Figure 4.40: FEA Strain on Original Crank at 27.3°

Figure 4.41: FEA Strain on Original Crank at -60.4° (Optimization Angle)

Table 4.7 presents a numerical comparison of the measured strain and the FEA strain. The percent difference columns compare the measured strain against the FEA strain. These differences are also displayed graphically in Figure 4.42.

Table 4.7: Strain Comparison of the Original Crank Arm

Original Crank Arm FEA Strain Verification								
Input Data			Measured Strain		FEA Strain		Percent Difference	
Initial Angle (ϕ)	Final Angle (Θ)	Applied Force (N)	Strain at Gauge #1 ($\mu\epsilon$)	Strain at Gauge #2 ($\mu\epsilon$)	Strain at Gauge #1 ($\mu\epsilon$)	Strain at Gauge #2 ($\mu\epsilon$)	% Difference at Gauge #1	% Difference at Gauge #2
90	63.2	157	-32	29	-33.03	29.02	-3.12%	-0.07%
75	48.9	195	-53	52	-54.55	52.70	-2.84%	-1.33%
60	38.0	227	-71	71	-72.03	70.09	-1.43%	1.30%
45	27.3	275	-100	101	-98.30	98.90	1.73%	2.12%
30	15.1	333	-128	132	-124.02	132.76	3.21%	-0.57%
15	1.2	410	-157	165	-156.25	161.08	0.48%	2.43%
0	-14.6	515	-190	203	-191.58	193.47	-0.82%	4.93%
-15	-32.2	689	-221	242	-220.86	243.31	0.06%	-0.54%
-30	-47.3	888	-229	256	-222.98	258.30	2.70%	-0.89%
-45	-60.4	1017	-167	297	-169.60	273.50	-1.53%	8.59%
-60	-74.1	967	-80	107	-80.26	106.53	-0.33%	0.44%
-75	-89.2	766	14	4	13.43	3.93	4.24%	1.72%
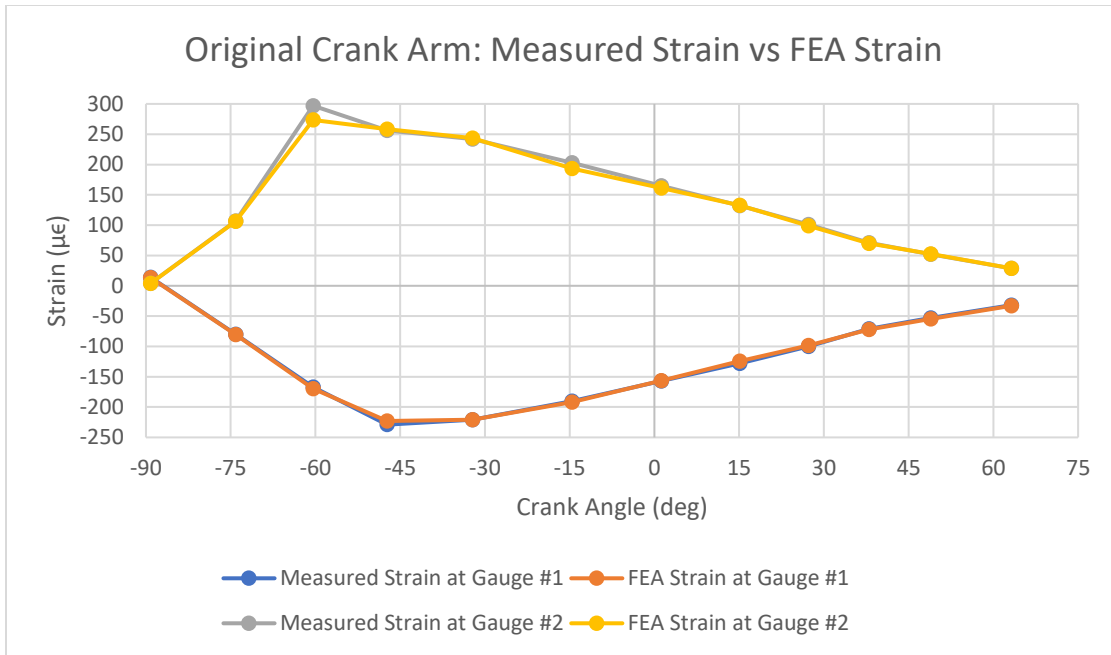
Figure 4.42: Comparison of Measured Strain vs FEA Strain on the Original Crank Arm

Next, the normal stresses of the original crank arm were then analyzed. The two probes shown in Figure 4.43 and Figure 4.44 display the normal stresses that occur within the original crank arm where the two strain gauges were attached to the physical crank arm.

Figure 4.43: FEA Stress on Original Crank at 27.3°

Figure 4.44: FEA Stress on Original Crank at -60.4° (Optimization Angle)

Table 4.8 presents the numerical comparison between the measured stress and the corresponding FEA stress. The percent difference columns compare the measured stress against the FEA stress. Figure 4.45 graphically displays how closely the measured stress data matches FEA stress data.

Table 4.8: Stress Comparison of the Original Crank Arm

Original Crank Arm FEA Stress Verification								
Input Data			Measured Stress		FEA Stress		Percent Difference	
Initial Angle (ϕ)	Final Angle (Θ)	Applied Force (N)	Stress at Gauge #1 (MPa)	Stress at Gauge #2 (MPa)	Stress at Gauge #1 (MPa)	Stress at Gauge #2 (MPa)	% Difference at Gauge #1	% Difference at Gauge #2
90	63.2	157	-6.18	5.60	-6.66	5.86	-7.26%	-4.42%
75	48.9	195	-10.23	10.04	-10.22	10.14	0.05%	-1.01%
60	38.0	227	-13.70	13.70	-14.86	13.37	-7.78%	2.50%
45	27.3	275	-19.30	19.49	-17.94	19.05	7.61%	2.35%
30	15.1	333	-24.70	25.48	-23.66	25.24	4.42%	0.96%
15	1.2	410	-30.30	31.85	-29.48	29.28	2.78%	8.78%
0	-14.6	515	-36.67	39.18	-36.72	35.90	-0.14%	9.15%
-15	-32.2	689	-42.65	46.71	-42.38	46.14	0.65%	1.23%
-30	-47.3	888	-44.20	49.41	-44.26	49.50	-0.14%	-0.19%
-45	-60.4	1017	-32.23	57.32	-32.64	51.79	-1.25%	10.67%
-60	-74.1	967	-15.44	20.65	-15.28	20.40	1.07%	1.21%
-75	-89.2	766	2.70	0.77	2.66	0.82	1.62%	-5.78%
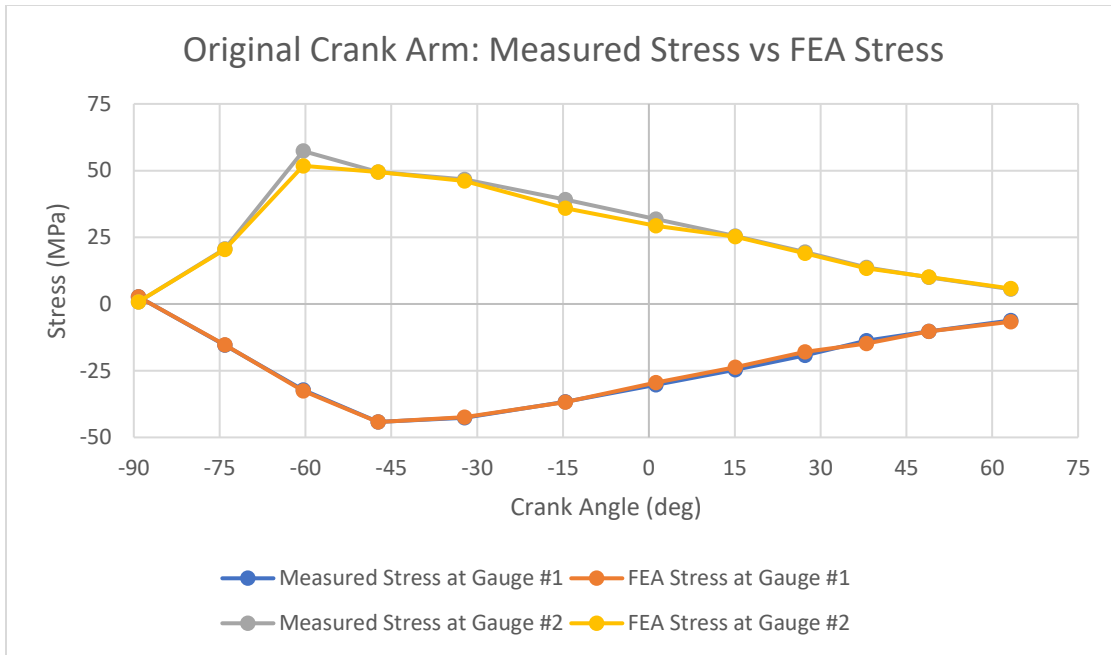
Figure 4.45: Comparison of Measured Stress vs FEA Stress on the Original Crank Arm

Next, the DFMAM optimized crank arm results were analyzed. Figure 4.46 and Figure 4.47 display the FEA results of the normal strain that occurred within the DFMAM optimized crank arm. As previously mentioned, two probes were added to the figures in the locations where the strain gauges were attached to the crank arm. This process was repeated for each of the 12 crank angles under consideration to gather the necessary FEA data to compare against the measured data.
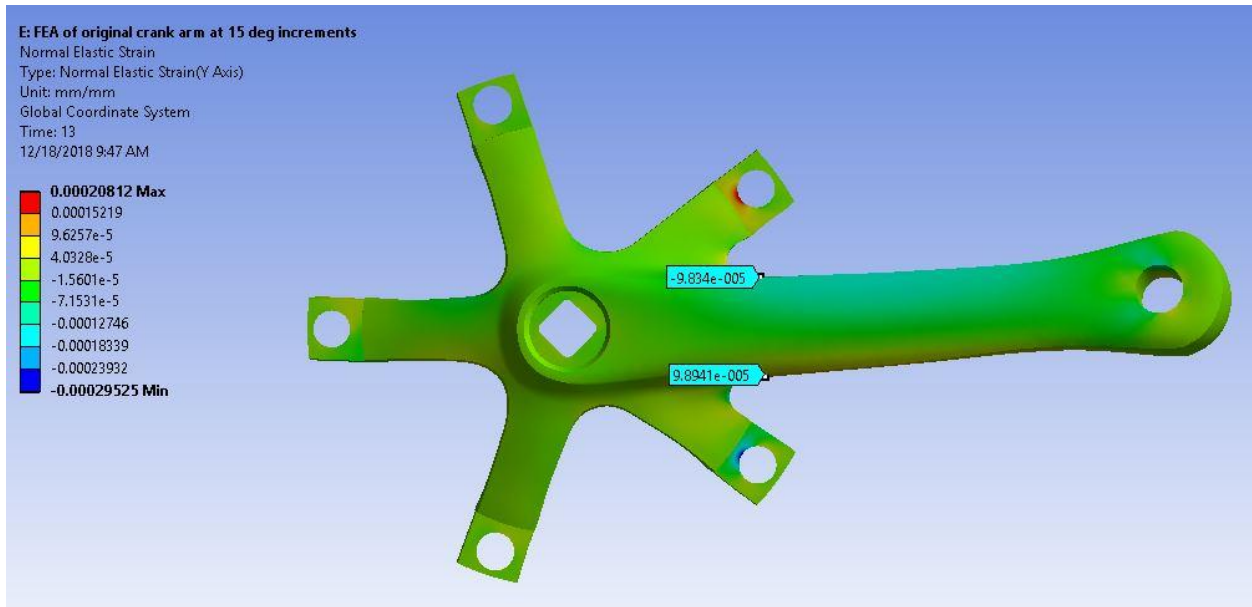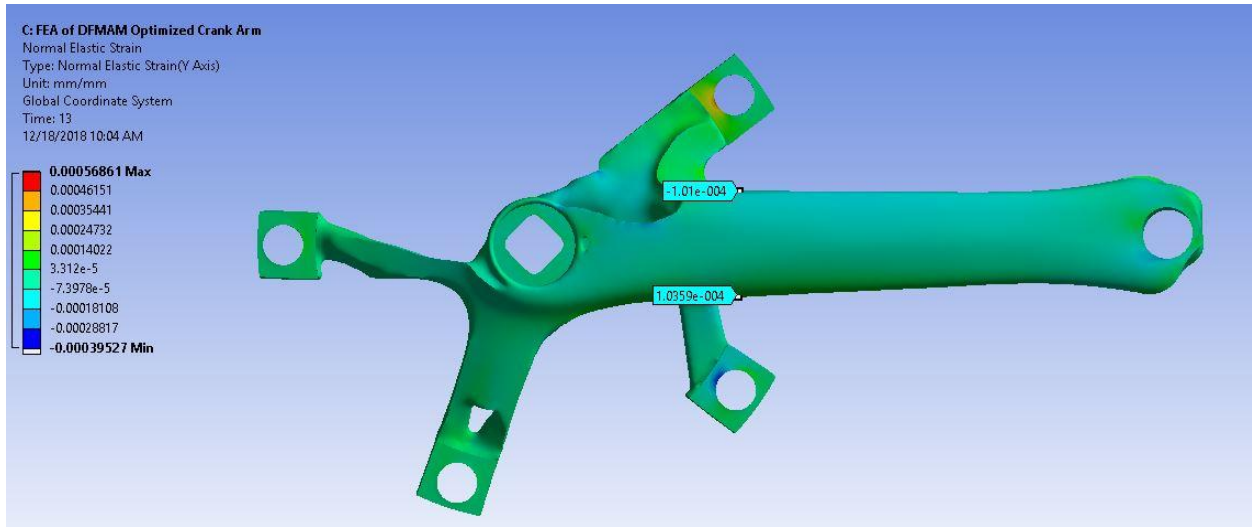
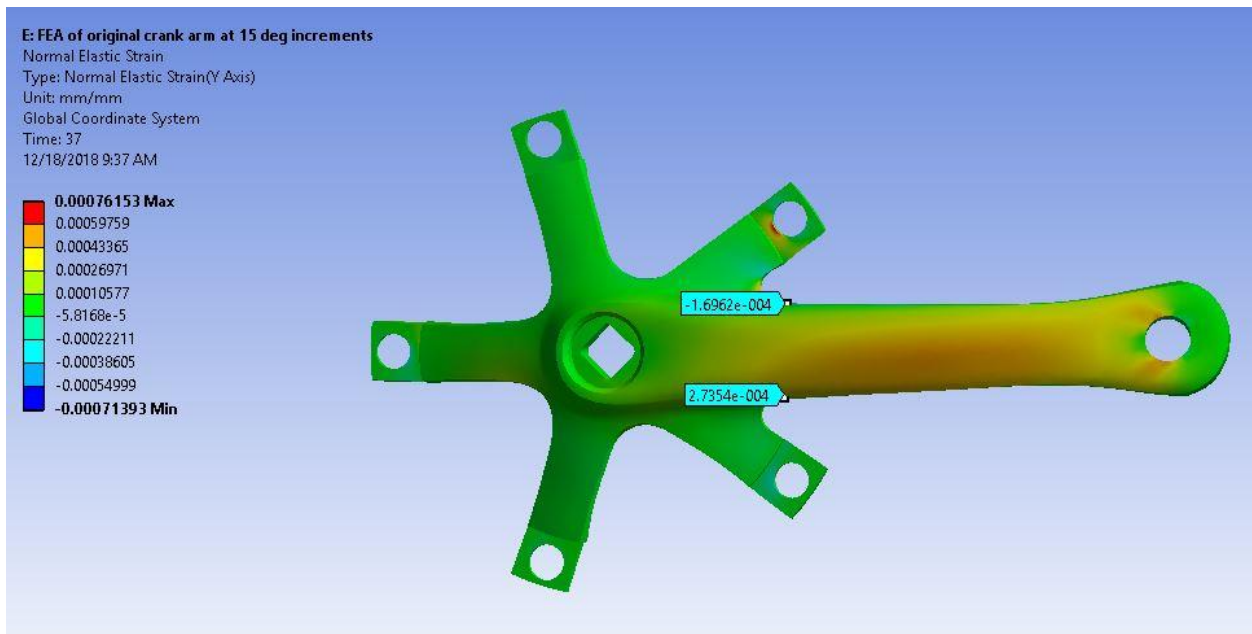Figure 4.46: FEA Strain on Optimized Crank at 27.3°
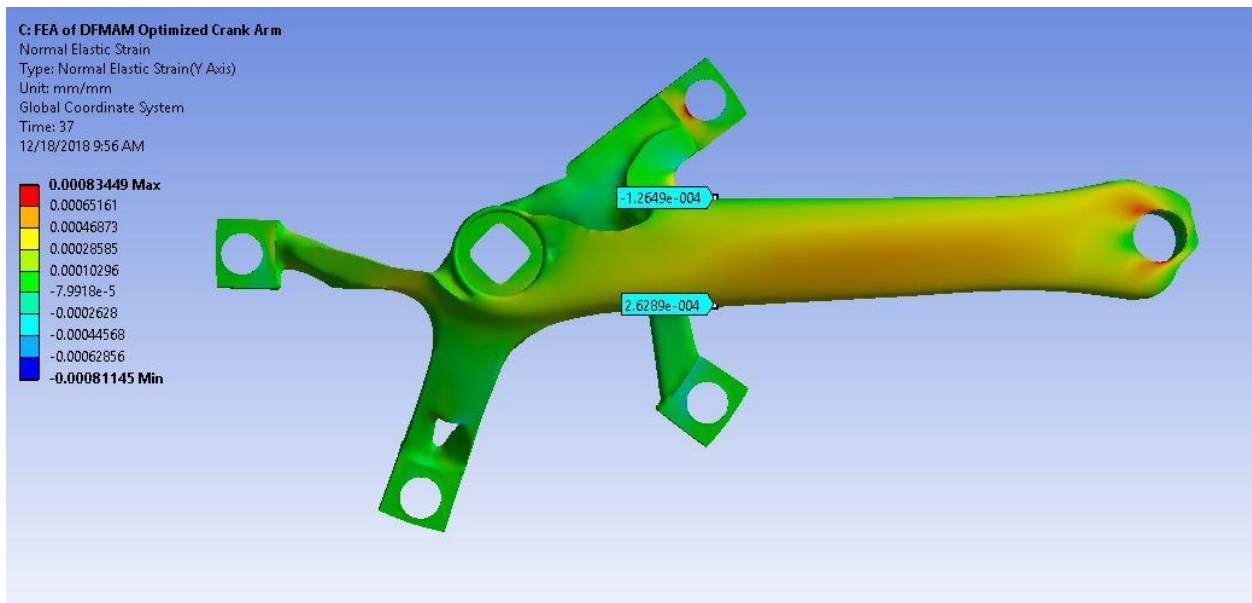
Figure 4.47: FEA Strain on Optimized Crank at -60.4° (Optimization Angle)

Table 4.9 presents a numerical comparison of the measured strain and the FEA strain for the DFMAM optimized crank arm. The percent difference columns compare the measured strain against the FEA strain. These differences are also displayed graphically in Figure 4.48.

Table 4.9: Strain Comparison of the Optimized Crank Arm

Optimized Crank Arm FEA Strain Verification								
Input Data			Measured Strain		FEA Strain		Percent Difference	
Initial Angle (ϕ)	Final Angle (Θ)	Applied Force (N)	Strain at Gauge #1 ($\mu\epsilon$)	Strain at Gauge #2 ($\mu\epsilon$)	Strain at Gauge #1 ($\mu\epsilon$)	Strain at Gauge #2 ($\mu\epsilon$)	% Difference at Gauge #1	% Difference at Gauge #2
90	63.2	157	-37	27	-37.39	27.20	-1.04%	-0.74%
75	48.9	195	-56	49	-56.43	49.69	-0.76%	-1.39%
60	38.0	227	-77	74	-77.24	74.14	-0.31%	-0.18%
45	27.3	275	-101	104	-101.00	103.59	0.00%	0.40%
30	15.1	333	-123	138	-122.35	136.92	0.53%	0.79%
15	1.2	410	-155	181	-155.73	171.64	-0.47%	5.45%
0	-14.6	515	-171	220	-171.99	210.33	-0.58%	4.60%
-15	-32.2	689	-180	259	-179.76	258.23	0.13%	0.30%
-30	-47.3	888	-176	289	-175.72	289.32	0.16%	-0.11%
-45	-60.4	1017	-125	260	-126.49	262.89	-1.18%	-1.10%
-60	-74.1	967	-18	144	-19.12	142.98	-5.86%	0.71%
-75	-89.2	766	60	30	59.50	30.96	0.84%	-3.11%
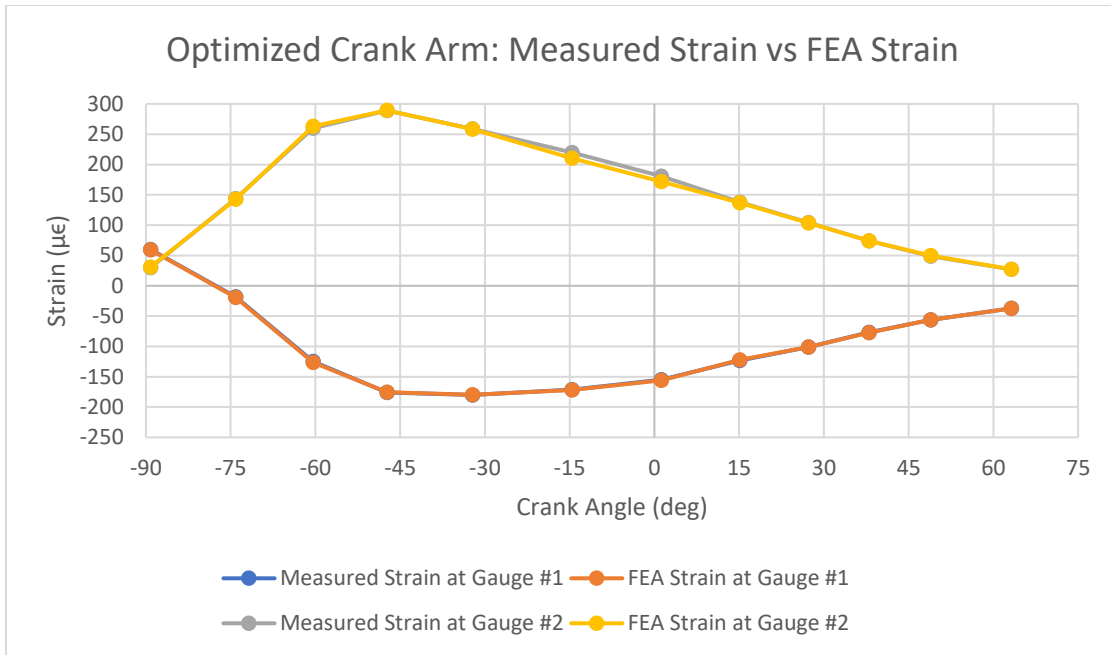
Figure 4.48: Comparison of Measured Strain vs FEA Strain on the Optimized Crank Arm

Figure 4.49 and Figure 4.50 display the normal stresses that occur within the optimized crank arm. The two probes were applied at the same location where the strain gauges were applied to the physical crank arm. The data points received from these probes were then compared with the data measured during the physical testing.
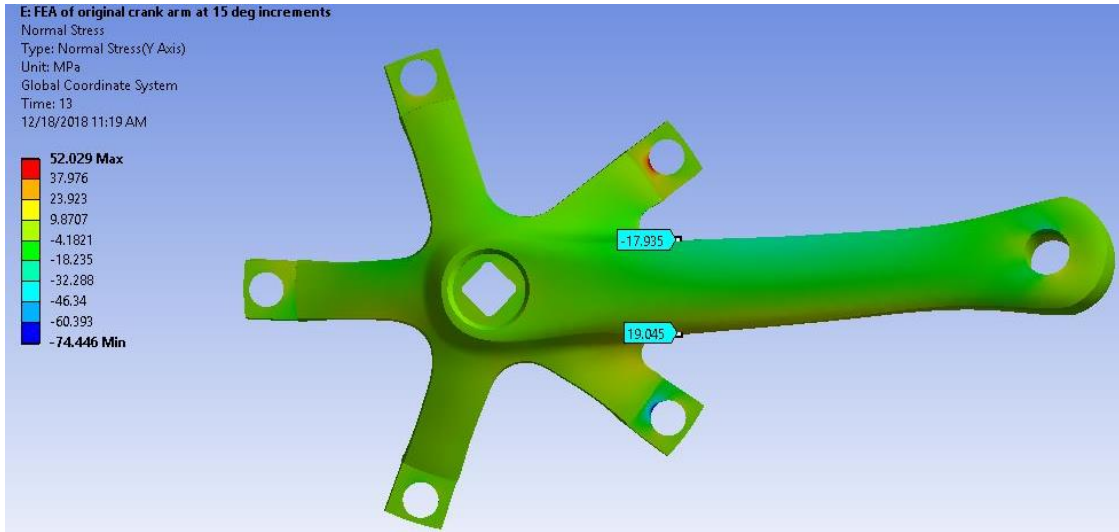
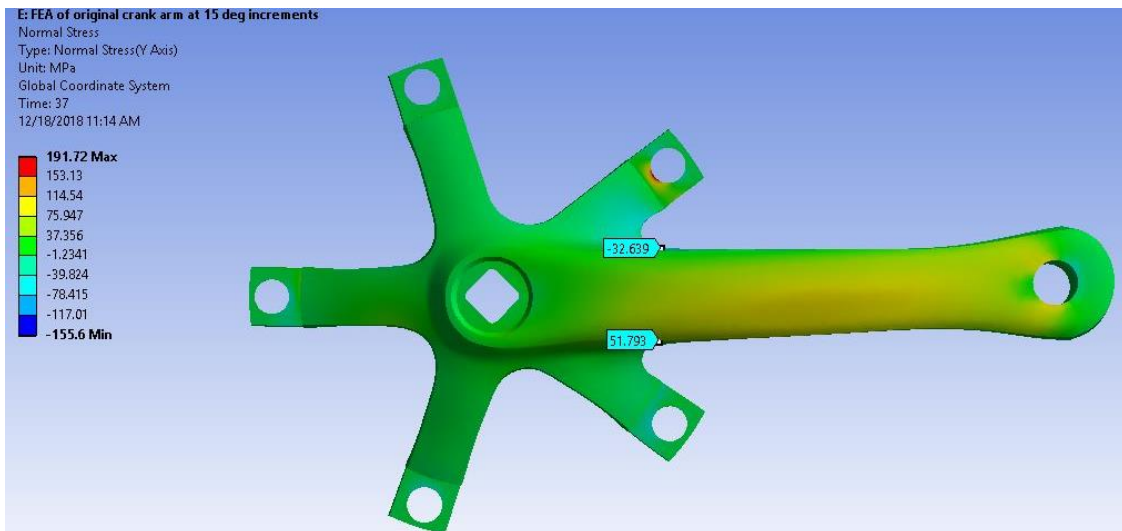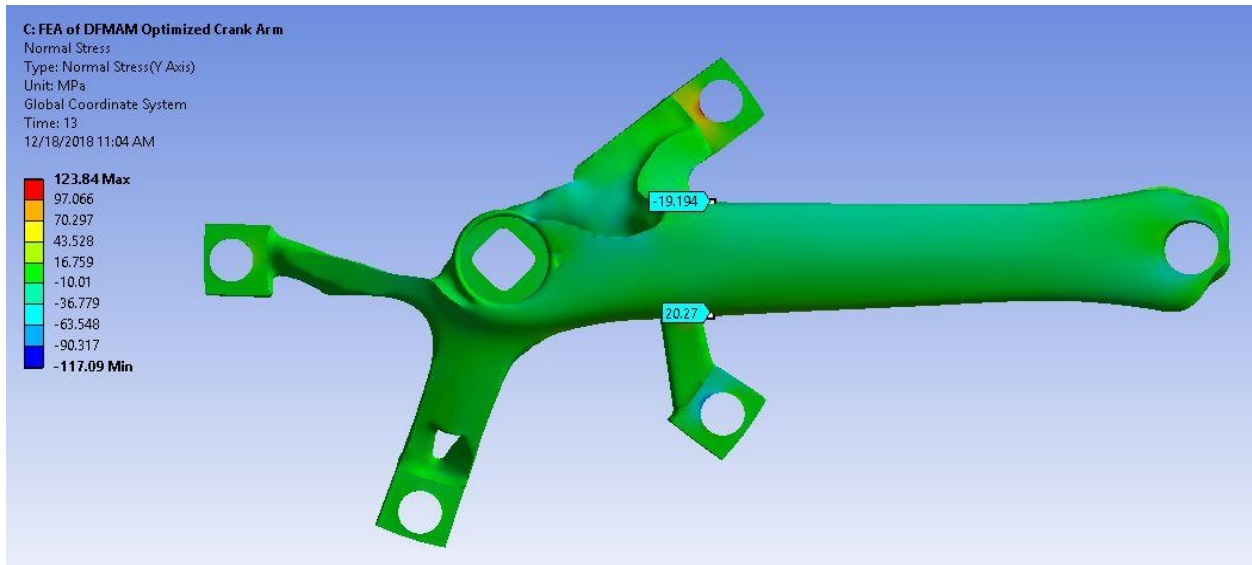Figure 4.49: FEA Stress on Optimized Crank at 27.3°
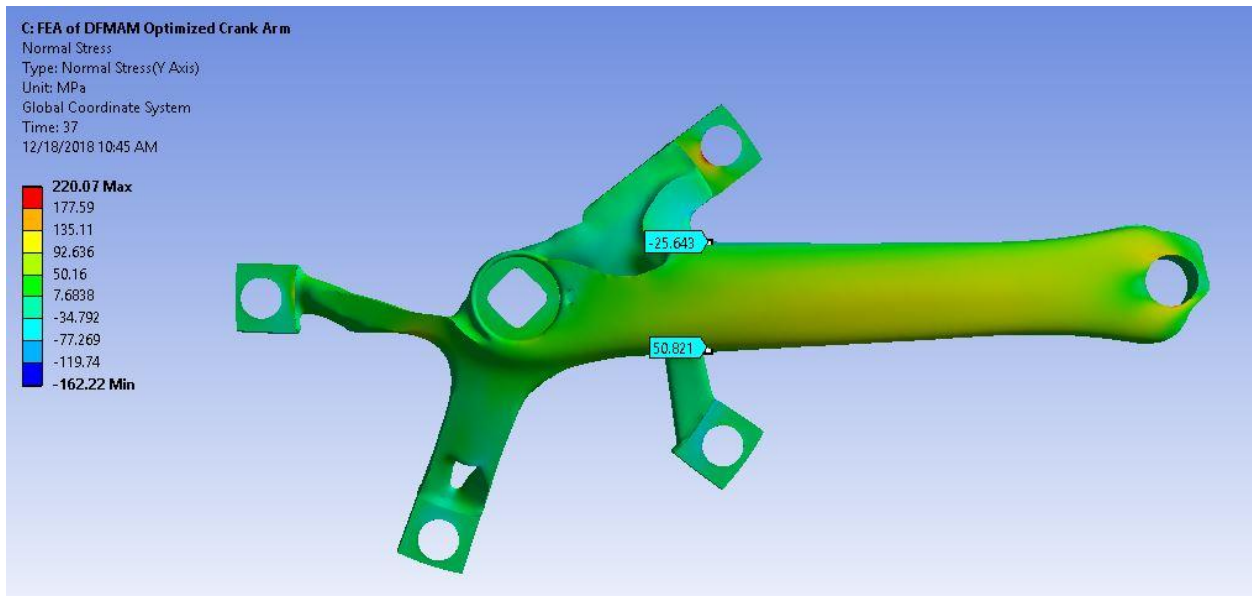
Figure 4.50: FEA Stress on Optimized Crank at -60.4° (Optimization Angle)

Table 4.10 presents the numerical comparison between the measured stress and the corresponding FEA stress. The percent difference columns compare the measured stress against the FEA stress. Figure 4.51 graphically displays how closely the measured stress data resembles FEA stress data.

Table 4.10: Stress Comparison of the Optimized Crank Arm

Optimized Crank Arm FEA Stress Verification								
Input Data			Measured Stress		FEA Stress		Percent Difference	
Initial Angle (φ)	Final Angle (θ)	Applied Force (N)	Stress at Gauge #1 (MPa)	Stress at Gauge #2 (MPa)	Stress at Gauge #1 (MPa)	Stress at Gauge #2 (MPa)	% Difference at Gauge #1	% Difference at Gauge #2
90	63.2	157	-7.14	5.21	-7.18	5.11	-0.54%	2.08%
75	48.9	195	-10.81	9.46	-10.82	9.39	-0.06%	0.68%
60	38.0	227	-14.86	14.28	-14.96	14.02	-0.64%	1.88%
45	27.3	275	-19.49	20.07	-19.19	20.27	1.56%	-0.98%
30	15.1	333	-23.74	26.63	-24.12	25.93	-1.56%	2.70%
15	1.2	410	-29.92	34.93	-29.91	34.80	0.02%	0.38%
0	-14.6	515	-33.00	42.46	-33.33	41.72	-0.97%	1.77%
-15	-32.2	689	-34.74	49.99	-34.53	49.94	0.60%	0.09%
-30	-47.3	888	-33.97	55.78	-33.77	55.22	0.60%	1.01%
-45	-60.4	1017	-24.13	50.18	-25.64	50.82	-5.92%	-1.26%
-60	-74.1	967	-3.47	27.79	-3.73	27.79	-6.76%	0.02%
-75	-89.2	766	11.58	5.79	11.17	5.54	3.67%	4.52%
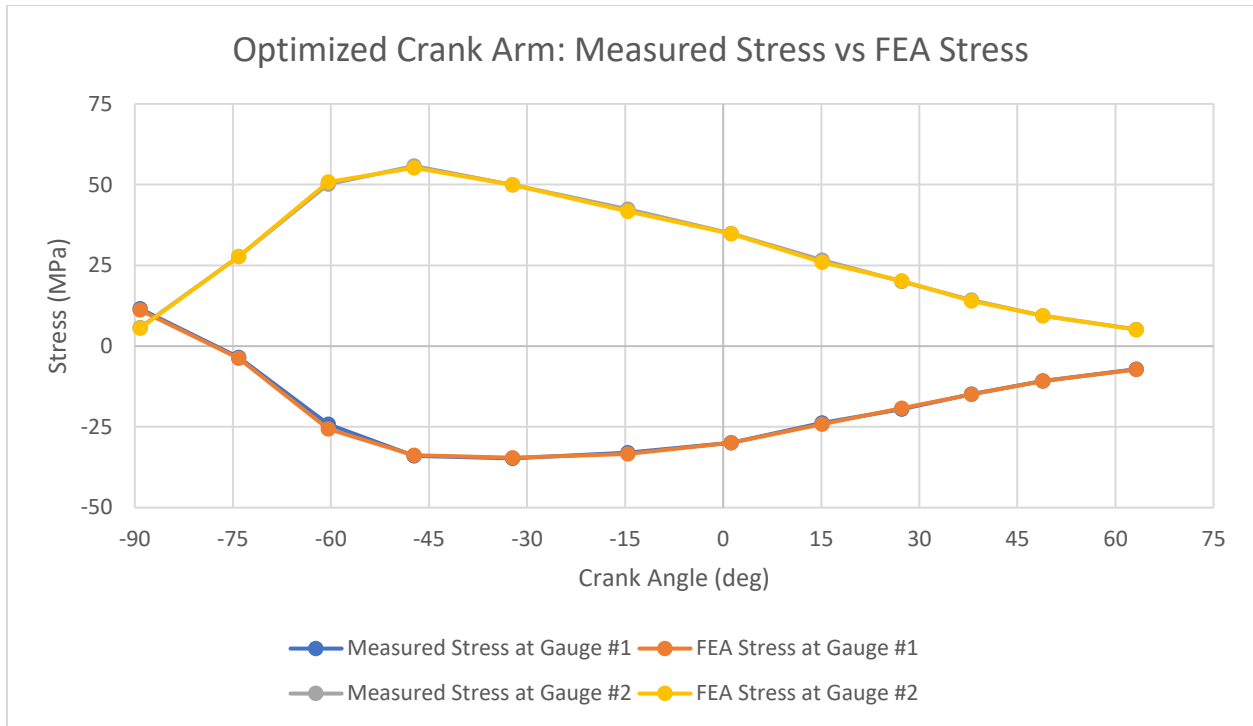
Figure 4.51: Comparison of Measured Stress vs FEA Stress on the Optimized Crank Arm

After gathering the strain and stress data for both crank arms, the two designs could then be compared against each other. First, the measured normal strain data of the original crank arm was compared to the measured normal strain data of the optimized crank arm, which is shown in Figure 4.52. Next, the measured normal stress data of the original crank arm was compared to the measured normal stress data of the optimized crank arm (see Figure 4.53).
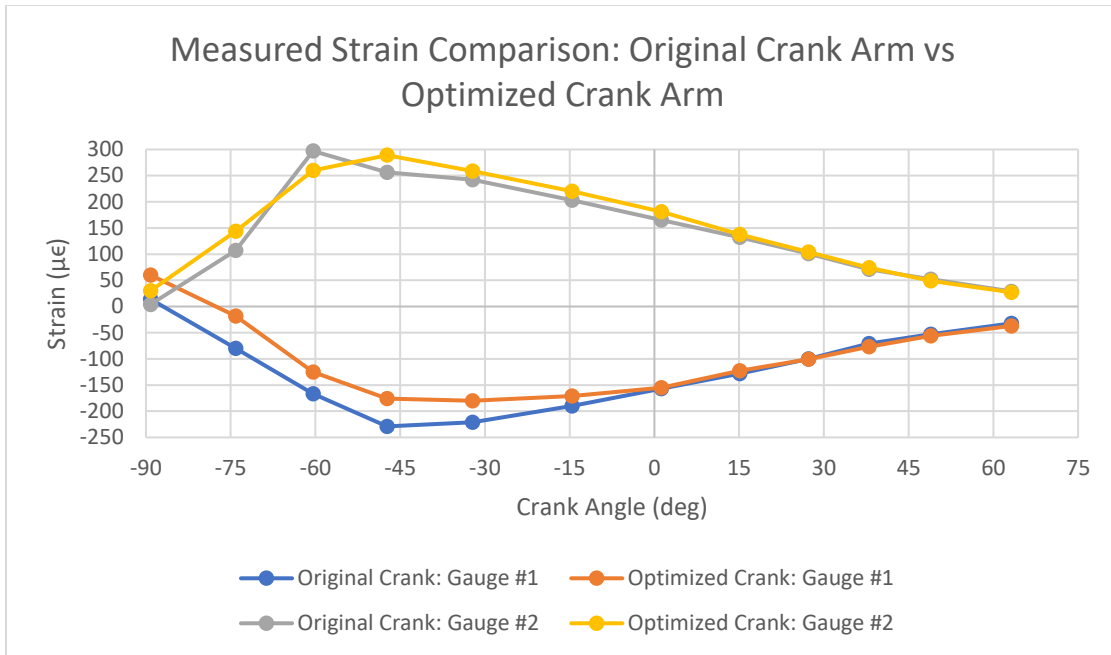
Figure 4.52: Measured Strain vs Final Crank Angle
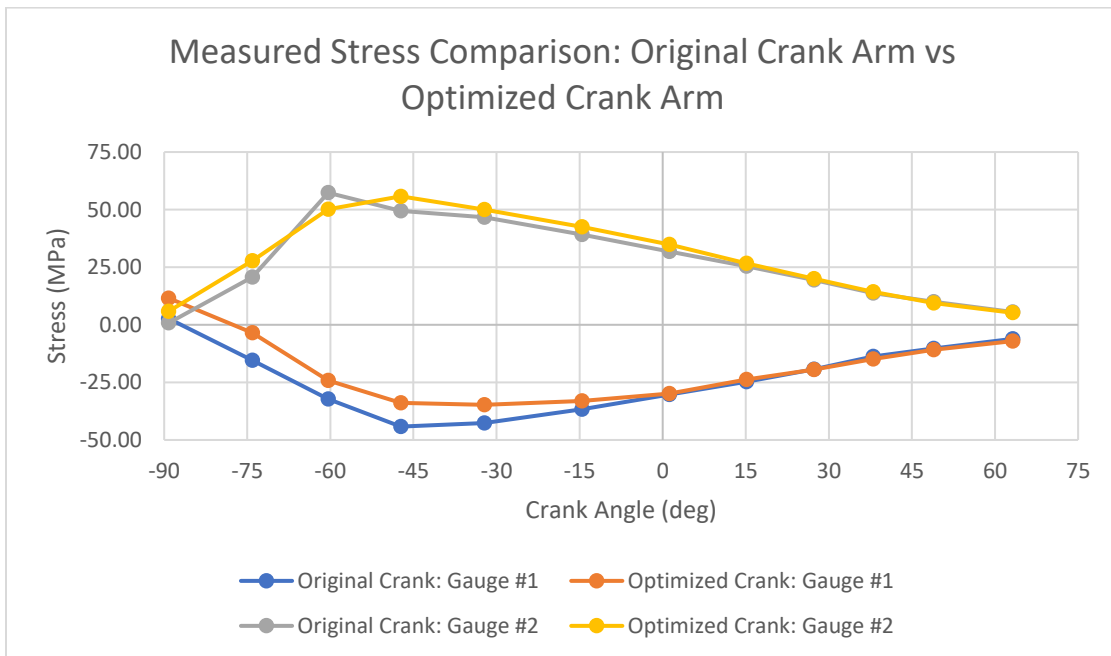
Figure 4.53: Measured Stress vs Final Crank Angle

The physical deflection measurements were then compared to FEA deflection data to determine the accuracy of the FEA model. As previously mentioned, two dial indicators were placed on the crank arm to collect deflection data in both the Z and Y axes relative to the tensile tester, which is known as the global coordinate system (GCS). Therefore, as the crank arm was rotated between tests, the dial indicators only collected data in the Z and Y directions relative to the global coordinate system. However, the coordinate system of the crank arm in the FEA analysis is considered to be the local coordinate system (LCS). Therefore, the FEA the deflection measurements (LCS) need to be translated to the global coordinate system of the tensile tester to achieve an accurate comparison. The deflection data from the Z and the X axes (LCS) was collected from the FEA model and was transformed into a singular deflection data point that relates to the measured deflection along the global Z axis (GCS). The data measured in the Y direction did not need to be transformed from the LCS to the GCS because it did not change with respect to the rotation of the crank arm.

Two equations were needed to perform the translation. Equation 4.4 was used to relate the Z axis of the LCS to the Z axis of the GCS, and equation 4.5 was used to translate the X axis of the LCS to the Z axis of the GCS.

$$Z_{1\,GCS} = Z_{LCS} * Cos(\theta) \quad\quad\quad (4.4)$$

$$Z_{2\,GCS} = X_{LCS} * Sin(\theta) \quad\quad\quad (4.5)$$

Next, the two vectors were added together to create a singular deflection value in the Z axis relative to the GCS. Finally, the translated FEA data was compared to the measured test data to determine the difference between the theoretical data and the actual data. Table 4.11 displays the deflection varication results of the original crank arm, and Table 4.12 presents the deflection verification results of the optimized crank arm.

Table 4.11: Deflection Comparison of the Original Crank Arm

Original Crank Arm FEA Deflection Verification							
Initial Angle (φ)	Final Angle (θ)	Axis	ANSYS Deflection Measurements (mm)	Adjusted Measurements (mm)	Total Z Deflection (mm)	Measured Deflection (mm)	Difference Between Measured and FEA (%)
45	27.3	Z	0.061980	0.055076	0.067026	0.064	-4.51%
		X	0.026054	0.011950	N/A	N/A	N/A
		Y	0.044115	N/A	N/A	0.025	-43.33%
-45	-60.4	Z	0.086087	0.042522	0.073009	0.076	4.10%
		X	0.035063	-0.030487	N/A	N/A	N/A
		Y	0.692160	N/A	N/A	0.711	2.72%

Table 4.12: Deflection Comparison of the Optimized Crank Arm

Optimized Crank Arm FEA Deflection Verification							
Initial Angle (φ)	Final Angle (θ)	Axis	ANSYS Deflection Measurements (mm)	Adjusted Measurements (mm)	Total Z Deflection (mm)	Measured Deflection (mm)	Difference Between Measured and FEA (%)
45	27.3	Z	0.085131	0.075649	0.086339	0.102	18.14%
		X	-0.023308	-0.010690	N/A	N/A	N/A
		Y	0.068980	N/A	N/A	0.025	-63.76%
-45	-60.4	Z	0.136970	0.067655	0.067911	0.064	-5.76%
		X	0.000294	-0.000256	N/A	N/A	N/A
		Y	0.740150	N/A	N/A	0.889	20.11%

136

CHAPTER 5:   DISCUSSION

The objective of this chapter is to compare the theoretical results to the experimental results to prove that an existing part can be improved by applying topology optimization and design for metal additive manufacturing principles to the design process. If the experimental data matches the theoretical simulation data, then the theoretical data can be further examined. If these data match, the two designs can be analyzed and compared to better understand the effects of the optimization study. The goal of this chapter is to discuss the similarities and differences between the original part and the optimized part and to determine if the physical characteristics of the lightweight optimized part are similar to the structural characteristics of the original part.

The objective of the physical testing was to prove that the FEA model accurately approximated the actual behavior of each crank arm. Therefore, the measured test results were compared to the FEA results to determine accuracy of the FEA model. On average, the measured normal stress and normal strain varied from the corresponding FEA data by 0.45%, which proves that the FEA was conducted properly and generated accurate results. Because the normal stress and the normal strain were proven to be accurate, it can be assumed that the entire FEA model is accurate. Thus, areas of high stress that cannot be accurately measured using experimental methods can be evaluated with the FEA. In addition, the topology optimization that was based upon local stress levels is also likely to be accurately performed.

Because the FEA model was proven to be accurate, the resulting stress data can be analyzed. As previously mentioned, a stress factor of safety of two was incorporated into the design. Therefore, the desired stress threshold was 250 MPa (F.S. = 2), which is half of the 500 MPa yield strength of the stainless-steel material. The original crank arm experienced a maximum stress of 206 MPa when the crank arm was at -60.4°. This stress value is 41.2% of the 500 MPa yield strength, or 82.4% of the desired 250 MPa stress threshold. The DFMAM optimized crank arm experienced a maximum stress of 307 MPa when the crank arm was at -14.6°. This stress value was 61.5% of the yield strength, or 122.8% of the 250 MPa desired stress threshold. However, the maximum stress values on the DFMAM optimized crank arm

137

are skewed because of a stress concentration point located on the base of the geometry associated with spider leg #5.

As seen in Figure 4.16 on page 101, a large stress concentration point at the base of spider leg #5's enhanced geometry is exposed when the crank angle equals -14.6°. The stress concentration point came into being because the optimization study was performed at a singular angle but was evaluated over the entire range of angles (at discrete intervals). The optimization study was performed at -60.4° and the stress concentration is most prevalent at -14.6°, which is a difference of 45.8°. As seen in Figure 4.17 on page 102, the stress concentration point at the optimization angle is miniscule. At the location of the stress concentration point when the crank arm is at -14.6°, the maximum stress equals 307 MPa, which is significantly greater than the stress in the surrounding geometrical area. However, this stress concentration is still less than the material's yield strength of 500 MPa, which means that the part will not break under the given loading conditions. However, this stress concentration point could potentially cause the part to fail because of fatigue. The concentration point could also cause the crank arm to fail if a larger force is applied to the crank arm. This stress concentration factor could be remedied by adding a fillet between the geometry of spider leg #5 and the shaft of the crank arm.

As previously mentioned in section 3.3.2 on page 38, the topology optimization study only focused on the forces that were applied at the initial crank angle of -45° ($\theta = -60.4°$). In order to best understand the direct effects of the optimization study, the stresses that occurred at the *optimization angle* must analyzed. First, the original stainless-steel crank arm experienced a maximum stress of 215 MPa (see Figure 4.1 on page 93), which is 86% of the desired 250 MPa stress threshold. The DFMAM optimized crank arm experienced a maximum stress of 237 MPa (see Figure 4.17 on page 102), which is 95% of the desired stress threshold. The maximum stress at the optimization angle increased by 22 MPa (10%). Therefore, at the angle under consideration, the optimization study was able to reduce the weight of the crank arm by 41.8% while only increasing the maximum stress within the part by 10%. However, the crank arm did experience loading at other angles, but this research did not optimize the crank arm in terms of these additional angles due to the scope of the project.

According to Figure 4.25 on page 107, the maximum stress values of the DFMAM optimized crank arm are, on average, 140% greater than the maximum stress values of the original crank arm. In order to decrease the average variance between the stresses in the original crank arm and the optimized crank arm, the scope of the optimization study should be increased. Instead of optimizing the crank arm at only one angle, the crank arm could be optimized for the loading conditions that occurred at other angles. This would reduce the average variance in stress, but it would also likely increase the mass of the crank arm. This study has determined that a topology optimization study can significantly reduce the mass of an object without extensively increasing the stress within the part. This topology optimization process is not limited to a bicycle crank arm, but it can also be applied to a wide variety of parts.

The FEA model can also be used to analyze the difference in total deformation between the two crank arms. The total deflection of the DFMAM optimized crank arm must be similar to the total deflection of original crank arm for the new design to be viable. If the newly designed crank arm is not similar in rigidity, the cyclist's pedaling efficiency will suffer. As previously shown by the results in Figure 4.23 on page 105, the theoretical maximum deflection vs crank angle curve of the DFMAM optimized crank arm closely follows the theoretical maximum deflection vs crank angle curve of the original crank arm. According to the results shown in Figure 4.26 on page 107, the DFMAM optimized crank arm, on average, experiences a 16% increase in maximum deflection. In order to best understand the direct effects of the optimization study, the deformation that occurred at the *optimization angle* must be analyzed. First, at the optimization angle, the original stainless-steel crank arm experienced a maximum deflection of .718 mm (see Figure 4.3), and the DFMAM optimized crank arm experienced a maximum deflection of .735 mm (see Figure 4.20). Therefore, at the optimization angle, the newly designed crank arm experienced an increase of 0.017 mm of deflection, which is an increase of 2.4%. At the angle under consideration, the optimization study reduced the weight by 41.8% while only increasing the maximum deflection by 2.4%. Therefore, it can be determined that the optimization process did not have a negative effect on the deflection properties.

The success of the topology optimization study also depends on the amount of weight that was saved between the optimized design and the original design. The theoretical weight, which was calculated by multiplying the volume times the density of the stainless-steel material, was very similar to the actual weight of the fabricated crank arms. Therefore, the calculated theoretical weight savings from the original stainless-steel crank arm to the DFMAM optimized crank arm accurately predicted the actual weight savings between the two crank arms. The DFMAM optimized crank arm weighs 359 grams (41.8%) less than the original stainless-steel crank arm, which is less than the original weight savings goal of 50%. However, the actual weight savings of 359 grams is still a significant improvement.

Ideally, the optimization study would have been performed using aluminum, the original material used to produce the Sugino RD2 crank arm. However, the EOS M 290 metal additive manufacturing machine located in the Rapid Center was not configured to fabricate aluminum parts. As a result, 316L stainless-steel was used for both the optimization study and the fabrication. 316L stainless-steel has a modulus of elasticity that is 161% greater than aluminum, and it is also 193% more dense than aluminum. Because of these differences in material properties, the optimization process was then able to remove a significant amount of material. However, if the optimization process had been performed using aluminum, the amount of material that could be removed may have been significantly different.

The stress, strain, and deflection data collected from the FEA model is subject to error. For each data point collected, a virtual probe was manually placed on the crank arm to display the value at that particular location on the crank arm. There were likely some inconsistencies between where the virtual probes that were placed and where the data measurement device was actually placed on the crank arm. The accuracy of the comparison is dependent on the placement of the probes on the crank arm within the FEA model. There is also a possibility that the measured data could be skewed due to instrumentation error. For example, the deflection results could have been affected by the angle at which the dial indicator was contacting the crank arm, the surface finish of the crank arm, and human error when reading the measurements. The DFMAM optimized crank arm had more surface irregularities near the pedal hole (which is where the dial indicators were located) than the original crank arm. The deflection results

displayed these irregularities. The difference between the measured deflection data and the FEA

deflection data were greater for the DFMAM optimized crank arm than they were for the original crank

arm.

CHAPTER 6:   CONCLUSION

Metal additive manufacturing enables the creation of complex and novel geometries. However, when using this advanced manufacturing method, design engineers must change the methodology used to design products. Topology Optimization is a new design method that can be used in conjunction with metal additive manufacturing to reduce the mass of a part without compromising the part's structural properties. Topology optimization can be used to analyze and improve existing products, or it can be used to create new designs based on a general bounding box and boundary conditions. The process demonstrated in this research focused on the procedure associated with redesigning an existing product for additive manufacturing. This research used a Sugino RD2 bicycle crank arm to demonstrate how the optimization process can reduce the weight of an existing product while maintaining the part's structural properties. The methods presented in this thesis are not limited to this bicycle component, but it can be applied to a large variety of structures.

This research demonstrated that a previously designed part could be further improved by using metal additive manufacturing in conjunction with topology optimization. However, the initial optimized geometry could not be easily manufactured because the geometry was crude. It was shown that the optimized geometry could be edited employing Design for Metal Additive Manufacturing (DFMAM) guidelines to increase the printability of the optimized part. Depending on the print orientation selected by the design engineer, the geometry may need to be edited to reduce/eliminate downward faces and to reduce the amount of part-on-part support structures, which are important considerations in metal additive manufacturing.

Reduction in weight while maintaining similar physical characteristics is expected when combining topology optimization with metal additive manufacturing. The optimized crank arm was 41.8% lighter than the original Sugino RD2 stainless-steel crank arm, which is quite significant, although less than the weight reduction goal of 50%. At the optimization angle, the maximum stress of the optimized crank arm increased by 10%, which satisfies the goal of the stress to be within 10% of the

original crank arm. Also, at the optimization angle, the total deflection of optimized crank arm increased by 2.4%, which satisfies the goal of the deflection to be within 5% of the original part. Therefore, at the optimization angle, the weight of the optimized crank arm was reduced by 41.8% at the expense of a 10% increase in maximum stress and a 2.4% increase in total deflection.

These results are not exclusive to this particular product. Similar conclusions would have been reached if this experiment were performed on a different part, except the exact percentages would differ from part to part. This research has proven that the topology optimization design methodology can be combined with metal additive manufacturing technology to create a fully-functional production product that is both light-weight and strong.

Design possibilities are endless with topology optimization and additive manufacturing. Topology optimization can be applied to a wide array of industries such as aerospace, automotive, civil engineering, and sporting equipment. For example, the process outlined in this research can be applied to an automotive component to reduce the weight of the vehicle and improve fuel efficiency, or this process can be applied to create a more efficient truss design. Topology optimization can be applied in any scenario in which strong and light-weight structures are imperative to the improvement of a part's performance.

6.1 Future Work

The topology optimization study performed in this research only focused on the maximum forces that were applied to the crank arm, which occurred when the crank arm was at -45°. Considering additional angles within the optimization study would result in a more accurate solution. Several different optimization studies could be performed to determine the optimum number of angles to include in the optimization study. For example, a second study can be conducted considering the forces that are applied at 45° and - 45°. The variance in stress and the amount of weight savings can then be compared to the original topology optimization study. This process could then be repeated using several additional angles to see how the number of angles added to the study will affect the variance in stress and the significance of the weight savings. It may be necessary to include every angle (in 15° increments) in the optimization

study to achieve satisfactory results. However, after adding several angles to the study, the results may converge on a solution. More experimentation is needed to understand the optimum number of angles to include in the optimization study.

The topology optimization study could also be repeated using aluminum instead of stainless-steel. The original Sugino RD2 crank arm was cast out of aluminum, which is not as dense as the stainless-steel used in this research. The changes in material properties would affect the amount of material that the topology optimization software could remove, which would affect the stress variance and the amount of weight reduction. It would also enable the optimized design to be field tested by a cyclist to verify its performance or uncover deficiencies in the design.

One additional area of future work would be to adapt the optimized crank arm to a functioning bicycle and allow experienced cyclists to perform a field test on the crank arm. Of course, an opposing crank arm would need to be first designed, analyzed, manufactured, and tested. Therefore, the test subjects could compare an optimized crank set to a commercially manufactured crank set.

The effects of topology optimization on the fatigue life of a part was not considered in this study. As stress increases, the fatigue life may be reduced. Further research must be performed to gain a better understanding of how the reduction in mass will affect the fatigue life of products that have been redesigned utilizing metal additive manufacturing and topology optimization. In the case of the bicycle crank arm used in this research, the optimized crank arm must be able to withstand a large number of cycles for the design to be suitable.

Due to the scope of this thesis, the optimization study was only conducted on one part. However, as previously mentioned, these results of this research should not be limited to a bicycle crank arm. The process outlined in this thesis can be applied to a variety of parts. The results from other optimized parts should be comparable to the results of this study. The ratios of the weight savings, increase in stress, and increase in deflection should be similar to the results found in this research. However, more research is needed to determine if these ratios are consistent.

WORKS CITED

[1] AutoDesk, "CAD Software," [Online]. Available: https://www.autodesk.com/solutions/cad-software.

[2] L. Sechrest, *Comparison Between the Dynamic Response of Selective Laser Melting (SLM) Parts and Conventionally Manufactured Parts,* 2016.

[3] E. Holmberg, B. Torstenfelt and A. Klarbring, "Stress Constrained Topology Optimization," *Struct Multidisc Optim,* vol. 48, pp. 33-47, 19 November 2012.

[4] E. Yares, "50 Years of CAD," 13 February 2013. [Online].
     Available: https://www.designworldonline.com/50-years-of-cad/.

[5] D. Cohn, "Evolution of Computer-Aided Design," 1 December 2010. [Online].
     Available: http://www.digitaleng.news/de/evolution-of-computer-aided-design/.

[6] J. Gardan, "Additive Manufacturing Technologies: Start of the Art and Trends," *International Journal of Production Research,* vol. 54, pp. 3118-3132, 9 February 2015.

[7] J. Chang, J. He, M. Mao, W. Zhou, Q. Lei, X. Li, D. Li, C.-K. Chua and X. Zhao, "Advanced Material Strategies for Next-Generation Additive Manufacturing," *Materials,* 29 December 2017.

[8] K. V. Wong and A. Hernandez, "A Review of Additive Manufacturing," *International Scholar Research Network,* vol. 2012, pp. 1-10, 29 May 2012.

[9] A. Hussein, L. Hao, C. Yan, R. Everson and P. Young, "Advanced Lattice Support Structures for Metal Additive Manufacturing," *Journal of Materials Processing Technology,* vol. 213, no. 7, pp. 1019-1026, July 2013.

[10] R. Castells, "DMLS vs SLM 3D Printint for Metal Manufacturing," 29 June 2016. [Online].
     Available: https://www.element.com/nucleus/2016/06/29/dmls-vs-slm-3d-printing-for-metal-manufacturing.

[11] B. Vrancken, V. Cain, R. Knutssen and J. Van Humbeeck, "Residual sress via the contour method in compact tension specimens produced via selective laser melting," *Acta Materialia,* 15 April 2014.

[12] EOS, "Real Highest Quality Metal Parts using the Benchmark in Additive Manufacturing - Now with the most comprehensive Monitoring Suite," September 2017. [Online]. Available: https://cdn0.scrvt.com/eos/413c861f2843b377/51d966b8b31d/EOS_System_Data_Sheet_ EOS_M_290_EN_V6_Web.pdf.

[13] EOS, "EOS M 290 Safety Training," EOS.

[14] R. Rajadhyaksha, "Turning Designs into Reality: The Manufacturability Paradigm," Geometric Limited, 2012.

[15] A. Pacurar, R. Pacurar, B. Eross, F. Popister and C. Otel, "Decreasing of the Manufacturing time for a Thermoforming Mold by Appling the DFM principles," in *MATEC Web of Converences*, 2017.

[16] E. Komi, "Component Design for Metal AM," VTT Techniical Research Centre on Finland Ltc, 3 October 2017. [Online]. Available: http://www.vtt.fi/inf/julkaisut/muut/2017/OA-Component-Design.pdf.

[17] X. Wang, S. Xu, S. Zhou, W. Xu, M. Leary, P. Choong, M. Qjan, B. Milan and Y. M. Xie, "Topological design and additive manufacturing of porous metals for bone scaffolds and orthopaedic implants: A review," *Biomaterials 82,* pp. 127-141, 2016.

[18] A. E. Patterson, S. L. Messimer and P. A. Farrington, "Overhanging Features and SLM/DMLS Residual Stresses Problem: Review and Future Research Needed," *Technologies,* pp. 1-21, 2017.

[19] T. Kannan, "Design for Additive Manufacturing," HCL Technologies Limited, 2017.

[20] W. King, A. Anderson, J.-L. Fattebert, R. Ferencz, N. Hodge, S. Khairallah, M. Matthews, A. Rubenchik, O. Walton and M. Want, "Achieving "Just Press Print" for Metal Additive Manufacturing," *Blue Sky Competition,* pp. 1-19, 2017.

[21] S. Hallgren, L. Pejryd and J. Ekengren, "(Re)Design for Additive Manufacturing," in *Procedia CIRP 50*, 2016.

[22] K. V. Praet, "Tips and Tricks for Metal 3D Printing: Recoaters," 21 July 2017. [Online]. Available: https://www.materialise.com/en/blog/metal-3D-printing-recoaters. [Accessed 19 November 2018].

[23] J. Reddy, "Nonlinear Finite Element Analysis with Applications to Solid and Structural Mechanics," College Station, 2010.

[24] AUTODESK, "What is Finite Element Analysis Software," [Online]. Available: https://www.autodesk.com/solutions/finite-element-analysis.

[25] V. Adams and A. Askenazi, Building Better Products with Finite Element Analysis, Santa Fe: OnWord Press, 1999.

[26] W. F. Bronsvoort and M. S. Smit, "Variational Tetrahedral Meshing of Mechanical Models for Finite Element Analysis," in *Computer-Aided Design & Applications*, CAD Solutions, LLC, 2008, pp. 228-240.

[27] ANSYS, "ANSYS Meshing Advanced Techniques," ANSYS, 17 April 2017. [Online]. Available: File:///C:/Users/jjsmith8/Desktop/Data%20Sheets/Ansys%20Meshing%20Techniques.pdf. [Accessed 15 November 2018].

[28] S. Hale, "What is Topology Optimization and Why Use It?," 22 May 2017. [Online]. Available: https://caeai.com/blog/what-topology-optimization-and-why-use-it.

[29] R. Larsson, "Methodology for Topology and Shape Optimization: Application to a Rear Lower Control Arm," Chalmers University of Technology, Goteborg, Sweeden, 2016.

[30] O. Sigmund and K. Maute, "Topology Optimization Approaches," *Struct Multidisc Optim,* vol. 45, pp. 1031-1055, 18 July 2013.

[31] D. Brackett, I. Ashcroft and R. Hague, "Topology Optimization for Additive Manufacturing," Wolfson School of Mechanical and Manufacturing Engineering, Loughborough, 2011.

[32] G. G. Holderbaum and R. D. de Souza Petersen, "Methodological Proposal for Teaching the Pedaling Technique of Cycling Using a System of Visual Augmented Feedpack: A Previous Study," EFDepordes, 2012. [Online]. Available: http://www.efdeportes.com/efd173/proposal-for-teaching-the-pedaling-technique.htm. [Accessed 26 October 2018].

[33] S. Auctherlonie, "The Pedal Stroke Part 1," [Online]. Available: https://ozarkcyclingadventures.com/articles/.

[34] Capture 3D, "GOM ATOS Triple Scan," Capture 3D, [Online]. Available: http://www.capture3d.com/3d-metrology-solutions/3d-scanners/atos-triple-scan. [Accessed February 2019].

[35] M. L. Hull and C. Stone, "Rider/Bicycle Interaction Loads During Standing Treadmill Cycling," *Journal of Applied Biomechanics,* vol. 9, pp. 202-218, 1993.

[36] ImageJ, "ImageJ - An open platform for scientific image analysis," ImageJ, 3 August 2018. [Online]. Available: https://imagej.net/Welcome. [Accessed 28 August 2018].

[37] ANSYS, "Mechanical User's Guide - Virtual Topology," ANSYS, Inc., 2018. [Online]. Available: https://ansyshelp.ansys.com/account/secured?returnurl=/Views/Secured/corp/v191/wb_sim/ds_Virtual_Topology_o_r.html. [Accessed 30 0ctober 2018].

[38] Materialise Magis, "The Most Powerful Data and Build Preparation Software," Materialise, [Online]. Available: https://www.materialise.com/en/software/magics. [Accessed 19 November 2018].

[39] Instron, *5960 Series Dual Column Table Frames,* Norwood, MA: Instron.

[40] R. C. Hibbeler, Mechanics of Materials, 9th ed., Boston, MA: Prentice Hall, 2014.

[41] Digi-Key Eletronics, "P3 Strain Indicator and Recorder," MicroMeasurements, [Online]. Available: https://www.digikey.com/catalog/en/partgroup/p3-strain-indicator-and-recorder/12751. [Accessed December 2018].

[42] EOS, "EOS StainlessSteel 316L Material Data Sheet," 2014. [Online]. Available: https://cdn0.scrvt.com/eos/77d285f20ed6ae89/dd6850c010d3/EOSStainlessSteel316L.pdf. [Accessed 2018].

[43] R. G. Budynas and J. K. Nisbett, Shingley's Mechanical Engineering Design, 9th ed., New York, New York: McGraw Hill, 2011.